UNIVERSITY OF NOVI SAD
FACULTY OF TECHNICAL SCIENCES
NOVI SAD

NOVEL METAMATERIAL STRUCTURES FOR NON-CONVENTIONAL PROPAGATION OF ACOUSTIC WAVES

PhD thesis

Candidate:
Norbert Cselyuszka, MSc

Advisor:
Prof. Vesna Crnojević-Bengin, PhD

Novi Sad, 2015

УНИВЕРЗИТЕТ У НОВОМ САДУ ● **ФАКУЛТЕТ ТЕХНИЧКИХ НАУКА**
21000 НОВИ САД, Трг Доситеја Обрадовића 6

КЉУЧНА ДОКУМЕНТАЦИЈСКА ИНФОРМАЦИЈА

Редни број, **РБР**:	
Идентификациони број, **ИБР**:	
Тип документације, **ТД**:	Монографска документација
Тип записа, **ТЗ**:	Текстуални штампани материјал
Врста рада, **ВР**:	Докторска дисертација
Аутор, **АУ**:	Норберт Чељуска
Ментор, **МН**:	Проф. др Весна Црнојевић-Бенгин
Наслов рада, **НР**:	Нове структуре метаматеријала за неконвенционално простирање акустичких таласа
Језик публикације, **ЈП**:	Енглески
Језик извода, **ЈИ**:	српски/енглески
Земља публиковања, **ЗП**:	Србија
Уже географско подручје, **УГП**:	
Година, **ГО**:	2015
Издавач, **ИЗ**:	Ауторски репринт
Место и адреса, **МА**:	
Физички опис рада, **ФО**: (поглавља/страна/ цитата/табела/слика/графика/прилога)	9 поглавља/124 страна/146 референци/4 табеле/105 слике /6 додатака
Научна област, **НО**:	Електротехничко и рачунарско инжењерство
Научна дисциплина, **НД**:	Електроника
Предметна одредница/Кључне речи, **ПО**:	Електро-акустичка аналогија, Метаматеријали, Акустички површински таласи
УДК	Монографска документација
Чува се, **ЧУ**:	Библиотека Факултета техничких наука, Универзитет у Новом Саду
Важна напомена, **ВН**:	

УНИВЕРЗИТЕТ У НОВОМ САДУ ● **ФАКУЛТЕТ ТЕХНИЧКИХ НАУКА**
21000 НОВИ САД, Трг Доситеја Обрадовића 6

КЉУЧНА ДОКУМЕНТАЦИЈСКА ИНФОРМАЦИЈА

Извод, **ИЗ**:		Метаматеријали су вештачки медијуми састављени од јединичних ћелија мањих од таласне дужине, пројектовани на посебан начин да при пропагацији таласа испољавају необичне особине које се иначе не срећу у природи. Већина истраживања у овој области фокусира се на електромагнетске метаматеријале. У овој дисертацији презентовани су резултати у новом мултидисциплинарном пољу метаматеријала у акустици и реализација нове неконвенционалне пропагације таласа применом јединичних ћелија метаматеријала. Научни допринос ове дисертације су три нова типа модова пропагације таласа и њихова контрола новим пројектованим јединичним ћелијама метаматеријала. У дисертацији је теоријски анализирана и експериментално показана нова класа CNZ (енг. *compressibility-near-zero*) акустичке пропагације постигнуте Хелмхолцовим резонатором. Дата је затворена аналитичка формула за ефективну стишљивост јединичне ћелије, а затим је показано да постоје две фреквенције које подржавају CNZ пропагацију. Такође, предложена је нова јединична ћелија са ефективном густином Лоренцовог типа, изведена је затворена аналитичка формула за њену ефективну густину и показане су „леворука“, еванесцентна и DNZ (енг. *density-near-zero*) пропагација акустичких таласа. На крају, по први пут је показано да се површински акустични талас који се простире на граници између флуида и чврсте избраздане површи може ефикасно контролисати само променом температуре, док геометрија избраздане површи остаје непромењена. Ово отвара могућности за бројне нове примене где је потребна лакоћа екстерног подешавања. Пратећи изложену теорију, демонстрирано је заробљавање звука контролисано температуром, као и његова примена у акустичкој спектралној анализи и мерењу температуре. Такође, презентован је акустички медијум са температуром контролисаним градијентом индекса преламања, као и његова примену у температурно контролисаном акустичком фокусирању.
Датум прихватања теме, **ДП**:		14. април 2014.
Датум одбране, **ДО**:		
Чланови комисије, **КО**:	Председник:	Проф. др Милан Сечујски
	Члан:	Проф. др Вера Марковић
	Члан:	Проф. др Србољуб Симић
	Члан:	Проф. др Анамарија Јухас
	Члан:	Проф. др Надер Енгета
	Члан, ментор:	Проф. др Весна Црнојевић-Бенгин

Потпис ментора

УНИВЕРЗИТЕТ У НОВОМ САДУ ● **ФАКУЛТЕТ ТЕХНИЧКИХ НАУКА**
21000 НОВИ САД, Трг Доситеја Обрадовића 6

КЉУЧНА ДОКУМЕНТАЦИЈСКА ИНФОРМАЦИЈА

Accession number, **ANO**:	
Identification number, **INO**:	
Document type, **DT**:	Monograph documentation
Type of record, **TR**:	Textual printed material
Contents code, **CC**:	PhD thesis
Author, **AU**:	Norbert Cselyuszka
Mentor, **MN**:	Vesna Crnojević-Bengin, PhD
Title, **TI**:	Novel metamaterial stuctures for non-conventional propagation of acoustic waves
Language of text, **LT**:	English
Language of abstract, **LA**:	Serbian/English
Country of publication, **CP**:	Serbia
Locality of publication, **LP**:	
Publication year, **PY**:	2015
Publisher, **PB**:	Author reprint
Publication place, **PP**:	
Physical description, **PD**:	9 chapters/124 pages/146 references/4 tables/105 figures /6 appendices
Scientific field, **SF**:	Electrical and Computer Engineering
Scientific discipline, **SD**:	Electronics
Subject/Key words, **S/KW**:	Electro-acoustic analogy, Metamaterials, Acoustic surface waves
UC	
Holding data, **HD**:	Library of the Faculty of Technical Sciences, University of Novi Sad
Note, **N**:	

УНИВЕРЗИТЕТ У НОВОМ САДУ ● **ФАКУЛТЕТ ТЕХНИЧКИХ НАУКА**
21000 НОВИ САД, Трг Доситеја Обрадовића 6

КЉУЧНА ДОКУМЕНТАЦИЈСКА ИНФОРМАЦИЈА

Abstract, **A**:		Metamaterials are artificial media composed of subwavelength unit cells, specifically engineered to exhibit unusual properties in relation to wave propagation, generally not found in nature. Most research in this area has been dedicated to electromagnetic metamaterials, In this thesis we present results in a new multidisciplinary field of metamaterials in acoustics and realization of non-conventional wave propagation applying novel metamaterial unit cells. The scientific contribution of this dissertation comprises three new types of wave propagation modes and their control with newly designed metamaterial unit cells. In the thesis, a novel class of compressibility-near-zero (CNZ) acoustic propagation, achieved by using Helmholtz resonators, is theoretically analyzed and experimentally demonstrated. A closed analytical formula for the effective compressibility of the proposed unit cell is presented, and the existence of two frequencies which may support CNZ propagation is shown. Furthermore, a new unit cell with effective mass density with Lorentzian type behavior is proposed, a closed analytical formula for its effective mass density is found, and the evanescent, left-handed propagation and density-near-zero acoustic wave propagation are demonstrated. In the end it is demonstrated for the first time that a surface acoustic wave propagating at the boundary between a fluid and a hard grooved surface can be efficiently controlled by varying only the temperature of the fluid, while the geometry of the grooved surface remains unchanged. This opens up a way for a number of new applications, all easily tunable by external means. Following theoretical considerations, we demonstrate temperature-controlled sound trapping and its applications in acoustic spectral analysis and temperature sensing. We also present a temperature-controlled gradient refractive index (GRIN) acoustic medium and apply it to achieve temperature-controlled acoustic focusing.	
Accepted by the Scientific Board on, **ASB**:		April 14th, 2014	
Defended on, **DE**:			
Defended Board, **DB**:	President:	Milan Sečujski, PhD	
	Member:	Vera Marković, PhD	
	Member:	Srboljub Simić, PhD	Menthor's sign
	Member:	Anamarija Juhas, PhD	
	Member:	Nader Engheta, PhD	
	Member, Mentor:	Vesna Crnojević-Bengin, PhD	

PROŠIRENI IZVOD NA SRPSKOM JEZIKU

NOVE STRUKTURE METAMATERIJALA ZA NEKONVENCIONALNO PROSTIRANJE AKUSTIČKIH TALASA

Uvod

U ovoj disertaciji prezentovani su rezultati u novom multidisciplinarnom polju metamaterijala u akustici i realizacija novog nekonvencionalnog prostiranja talasa primenom jediničnih ćelija metamaterijala. U poslednjih nekoliko godina svedoci smo izuzetno brzog razvoja u oblasti metamaterijala, veštačkih struktura koje pokazuju osobine kakve se ne mogu naći u prirodi. Metamaterijali se projektuju korišćenjem jediničnih ćelija čije su dimenzije mnogo manje od talasne dužine talasa koji se prostire kroz posmatrani medijum. U zavisnosti od geometrije jedinične ćelije mogu se postići proizvoljno niske, visoke ili čak negativne vrednosti dielektrične permitivnosti i magnetne permeabilnosti. Sličan razvoj se može primetiti i kod akustičkih stuktura, postoje tzv. akustički metamaterijali.

Akustički metamaterijali

Akustički metamaterijali su zasnovani na periodičnom ponavljanju jedinične ćelije koja je mnogo manja od primenjene talasne dužine, prema sličnom principu kao u elektromagnetici. Na taj način možemo modifikovati efektivne parametre u posmatranoj homogenoj strukturi. Pri prostiranju akustičkih talasa kroz akustičke metamaterijale opažaju se slični efekti kao kod elektromagnetnih talasa i metamaterijala. U zavisnosti od jedinične ćelije akustičkog metamaterijala, stišljivost i gustina metamaterijala mogu se napraviti proizvoljno mali, veliki ili čak negativni. Dve konstante koje opisuju ponašanje akustičkih talasa u sredini su gustina materiajala (ρ) i stišljivost materijala (β). Postoji mogućnost pravljenja struktura tako da efektivna vrednost navedenih parametara bude negativna u nekom određenom opsegu učestanosti. Ako je samo jedan od dva parametra, ρ ili β, manji od nule, metamaterijal se u datom opsegu učestanosti naziva jednostruko negativan metamaterijal. U ovom slučaju nije moguće prostiranje akustičkog talasa u posmatranom opsegu učestanosti. U slučaju kada su oba parametara (ρ i β) manja od nule u nekom opsegu učestanosti, imamo dvostruko negativan metamaterijal. U opsegu učestanosti gde je metamaterijal dvostruko negativan (LH) postoji mogućnost prostiranja akustičkog talasa, konstanta prostiranja u ovom slučaju je realna, ali ima negativnu vrednost. Negativne vrednosti ρ mogu se dobiti pomoću niza tankih membrana, a negativne vrednosti za stišljivost (β) dobijaju se pomoću niza Helmholcovih rezonatora ili pomoću niza malih otvora na cevi kroz koju se prostire akustički talas. *Near-zero* metamaterijali čine posebnu klasu. Kod ove vrste metamateriajala jedan od efektivnih parametara materijala je blizu ili jednak nuli. Interesantna stvar kod ovih fenomena jeste da fazna brzina talasa u *near-zero* sredini teži beskonačnosti i zbog toga dobijamo dodatni efekat tuneliranja talasa bez promene faze. Na *near-zero* učestanosti fazna brzina akustičkog talasa je beskonačna i zato je faza na početku i kraju kanala ista i ne zavisi ni od dužine ni od oblika kanala.

Analiza akustičkih kola

Disertacija obuhvata analizu, CAD (engl. *computer-aided design*) projektovanje, simulaciju i optimizaciju novih metamaterijalnih struktura, kao i fabrikaciju i merenje karakteristika fabrikovanih

kola i analizu rezultata merenja. Računarsko projektovanje akustičkih metamaterijala je izvršeno pomoću softverskih paketa za multifizičke simulacije *Comsol Multiphysics 4.0*. *COMSOL* je program zasnovan na metodi konačnih elemenata (FEM). Za dodatnu numeričku analizu akustičkog kola napravljen je model baziran na teoriji kola i teoriji vodova. Razvijena je nova metoda za određivanje S-matrica dvopristupnog akustičkog kola. Metoda je zasnovana na merenju sa četiri mikrofona. Pomoću dva mikrofona na jednom, i dodatna dva mikrofona na drugom pristupu, može se razdvojiti upadna i reflektovana komponenta ravanskog zvučnog talasa. Razvijen merni sistem se sastoji još od jednog četvorokanalnog digitalnog osciloskopa i izvora, a sve je povezanao sa računarom koji služi za kontrolu procesa i obradu signala. Mikrofoni nisu proizvoljno smešteni u kolo, već svi imaju određeno mesto. Na slici 1. se vidi raspored M_A, M_B, M_C i M_D mikrofona:

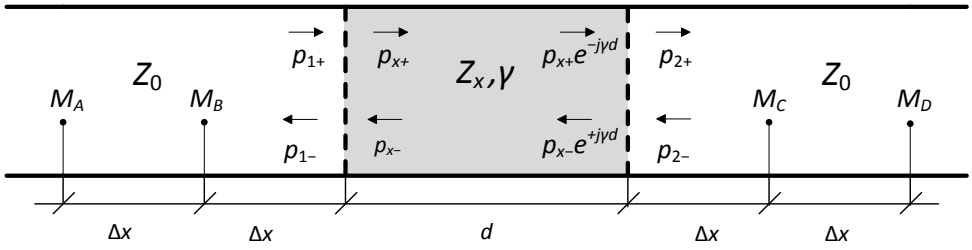

Slika 1. Model za ekstrakciju akustičke S-matrice

Međusobno rastojanje između dva mikrofona na istoj strani kola je konstantno i iznosi Δx=50 mm, a rastojanje između kola i bližeg mikrofona je takođe konstantno: Δx=50 mm. Sa četiri mikrofona koji su vezani sa digitalnim osciloskopom snimamo sva četiri signala u istom trenutku. Iz osciloskopa sve signale snimamo na računar za dalju obradu. Ovaj postupak ponavljamo za ceo opseg učestanosti sa željenim koracima u kojima želimo ispitivati naše kolo. Softverska obrada signala sastoji se od filtriranje visokofrekvencijskog šuma i neželjenih komponenti signala, određivanja amplitude i faze svakog signala, razdvajanja upadne i reflektovane komponente talasa i na kraju određivanja akustičke S-matrice. Za karakterizaciju akustičkih metamaterijala neophodno je ekstrahovati efektivne parametre - stišljivost (β_{eff}) i gutinu (ρ_{eff}) metamaterijala. Akustička talasna impedansa z i akustički indeks prelamanja n se mogu izračunati direktno iz S-matrice, a pomoću njih i efektivni parametri metamaterijala. Matlab kôd za određivanje akustičke S-matrice i za ekstrakciju parametara su dati u pilogu (A1, A2).

Near-zero prostiranje talasa: stišljivost *near-zero* metamaterijali

Near-zero metamaterijali su specijalna podklasa metamaterijala sa beskonačnom faznom brzinom. Ova vrsta prostiranja u akustici pokazana je za slučaj kada je gustina blizu nule. U disertaciji je pokazana nova klasa prostiranje akustičkih talasa gde je stišljivost blizu nule tzv. CNZ (eng. *compressibility-near-zero*) akustičko prostiranje. Ova vrsta prostiranja je postignuta Helmholcovim rezonatorom. Helmholc resonantor je struktura koja se sastoji iz dva dela, uske cevi i komore, kao što

je prkazano na Slici 2. Dimenzije rezonatora su manje od talasne dužine i može se posmatrati kao jedinična ćelija sa efektivnom stišljivošću.

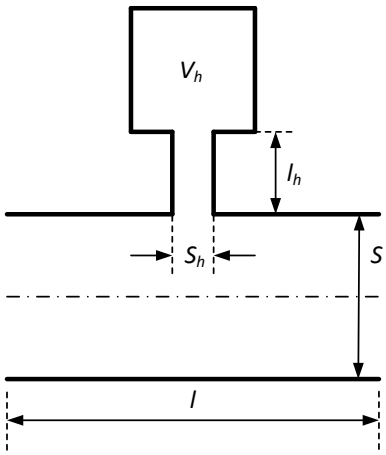

Slika 2. Poprečni presek Helmholc rezonatora vezan sa akustičkom cevi

Jedinična ćelija je detaljno analizirana i izveden je izraz za efektivnu stišljivost Halmholcovog rezonatora. U slučaju prostoperiodične pobude efektivna stišljivost Helmholc rezonatora zavisi od učesatanosti i može se zapisati u obliku:

$$\beta_{\text{eff}} = \beta_0 \left(1 + \frac{S_h}{V} \cdot \frac{1}{\frac{S_h}{V_h} - l_h \frac{\omega^2}{c^2}} \right). \tag{1}$$

Iz izraza se može zaključiti da je jedinična ćelija pogodna za *near-zero* propagaciju na određenoj učestanosti. U *Comsol*-u dizajniran je i simuliran Helmholc rezonator ispunjen vazduhom sa dimenzijama S= 206 mm^2, S_h= π mm^2, c= 343.12 m/s (T= 293.15 K), β_0= 7.04 Pa^{-1}, l= 32 mm, l_h= 28 mm, V_h= 567 mm^3. Rezultati simulacije, akustički S-parametri i ekstrahovane efektivne stišljivosti su prikazani na Slici 3. Na Slici 3 prikazan je i Helmholc rezonator sa ekvivlentnim akustičkim elementima.

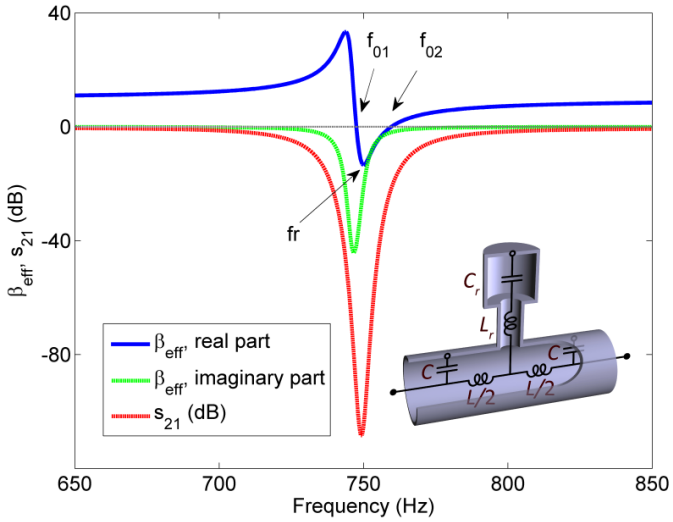

Slika 3 Prenosna karakteristika i ekstrahovana stišljivost Helmholc rezonatora (u prilogu je prikazan Helmholc rezonator sa akustičkim komponentama).

Odziv rezonatora je nepropusan u opsegu gde je stišljivost manja od nule. U ovom delu, struktura se ponaša kao jednostruko negativan medijum u kojem nije dozvoljena propagacija akustičkih talasa. Na Slici 4 je prikazana ekstrahovana efektivna stišljivost Helmhoc rezonatora upoređena sa efektivnom stišljivošću koja je dobijena analitičkim putem.

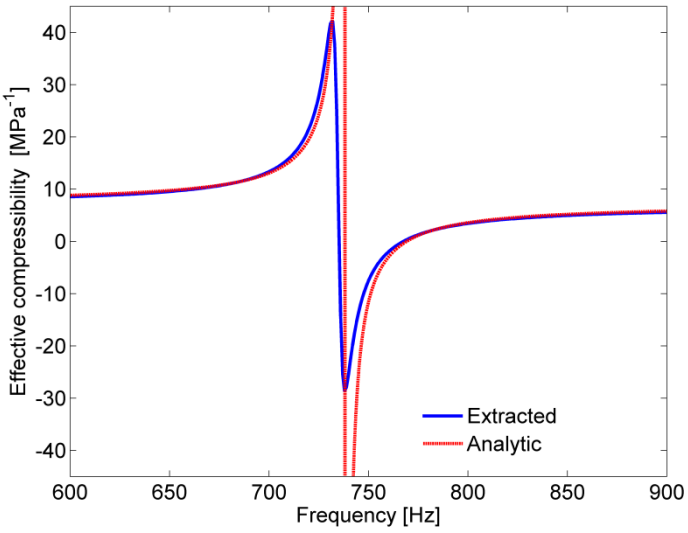

Slika 4 Ekstrahovaan efektivna stišljivost Helmholc rezonatora upoređena sa efektivnom stišljivosti dobijene iz analitičke formula

Ekstrahovana efektivna stišljivost i efektivna stišljivost iz analitičkog izraza pokazuju dobro poklapanje. Kao što je pokazano, jedinična ćelija je nepropousna u delu spektra gde je efektivna stišljivost negativna, dok je u ostalim delovima spektra propusna. Kako bismo pokazali *near-zero* propagaciju potrebno je koristiti *host* strukturu gde između dva pristupa imamo veliku neprilagođenost impedansi. U slučaju kada impedanse nisu prilagođene, struktura je nepropusna, a dok su u slučaju *near-zero* propagacije pristupi uvek prilagođeni nezavisno od strukture kola. Zato smo za prikazivanje *near-zero* propagacije kao *host* strukturu kostistili niskopropusni filtar. Na Slici 5 je prikazana *ho*st struktura opterećena Helmholc rezonatorima.

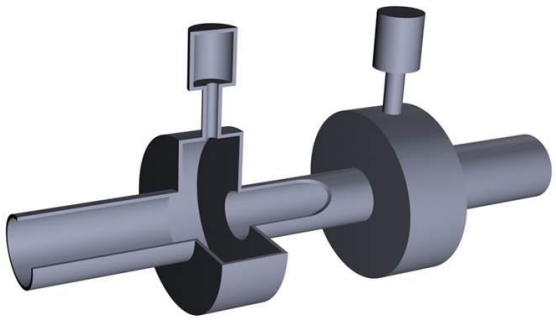

Slika 5. Stišljivost near-zero (CNZ) metamaterjial

Rezultati simulacije su prikazani na Slici 6 uporedo sa odzivom niskoporpusnog filtra bez helmholcovog rezonatora. Iz odziva se može zaključiti da se u nepropusnom opsegu niskoporpusnog

filtra pojavljuje jedan uski propusni opseg tačno na učestanosti na kojoj je efektivna stišljivost jediniče ćelije jednaka nuli.

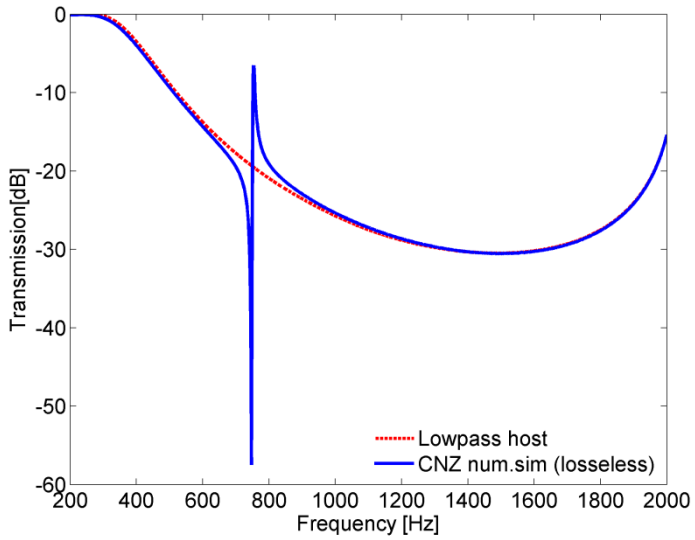

Slika 6 Odziv niskopropusnih filtara i CNZ struktura

Kako bismo dokazali da novi propusni opseg stvarno ima *near-zero* karakteristike ekstrahovana je faza po dužini strukture. Kod *near-zero* prostiranja očekivano je da je fazna razlika između dva kraja strukture blizu nule, zato što je fazna brzina beskonačno velika. Distribucija faze po dužinu CNZ metamaterijala je prikazan na Slici 7 uporedo sa faznom brzinom u običnoj akustičkoj cevi po istoj dužini.

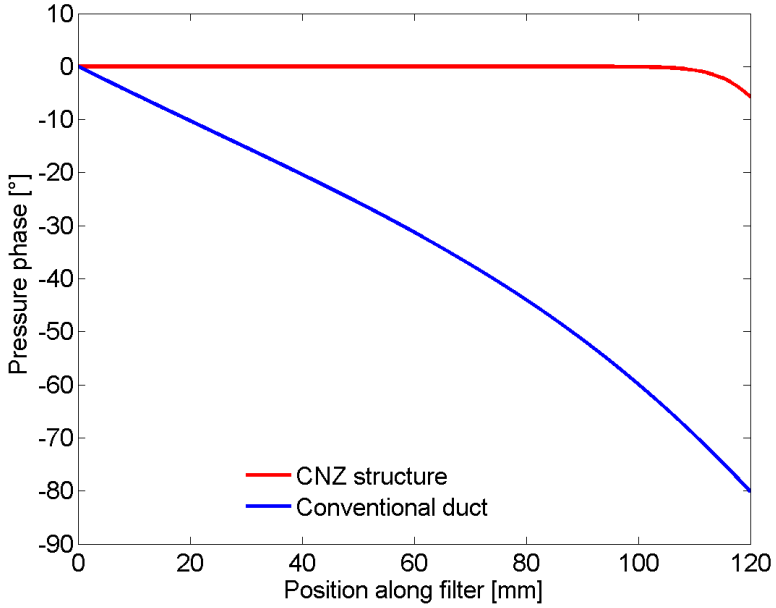

Slika 7. Fazna distribucija po dužini strukture na near-zero učestanosti

U slučaju akustičke cevi iste dimenzije kao CNZ sruktura ukupni fazni pomeraj je 80°, a u slučaju CNZ stuktura na *near-zero* učestanosti redukovan je na 5.7°. Za eksperimentalnu verifikaciju

teorijskih i numeričkih rezultata *near-zero* metamaterijala fabrikovana je struktura sa slike 5. Fabrikovana struktura je prikazana na Slici 8.

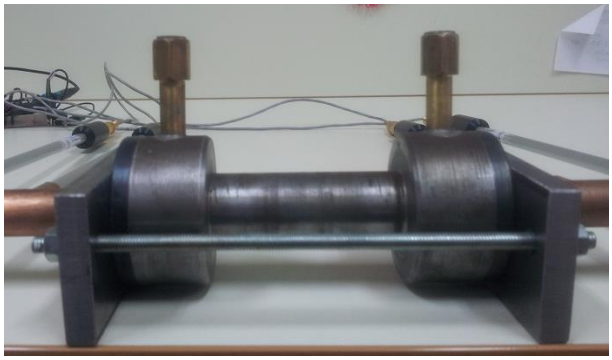

Slika 8 Fabricated CNZ structure

Merenje akustičkih S-parametara izvršeno je na osnovu metode razvijene u toku istraživanja. Laboratorijski merni set za određivanje akustičkih S-parametra prikazan je na Slici 9.

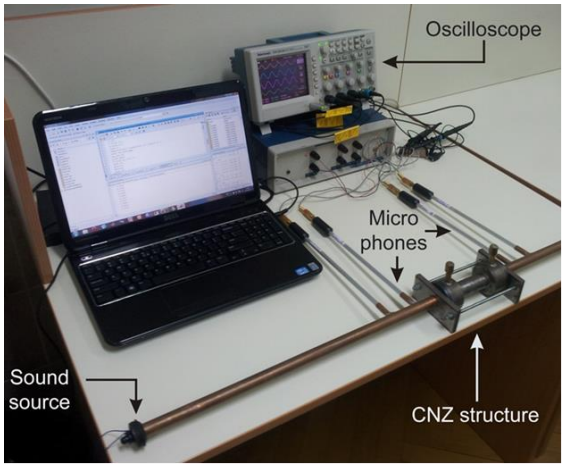

Slika 9 Laboratorijski merni sistem za održivanje akustičkih S-parametara

Na Slici 10 su prikazana izmerena prenosna funkcija od tri seta merenja u frekventnom opsegu od 600 Hz do 920 Hz.

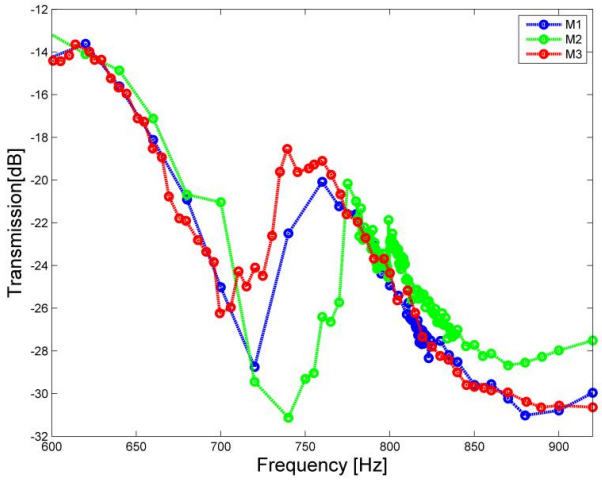

Slika 10 Izmerena prenosna karakteristika CNZ strukture

Između različitih setova merenja postoji dobra saglasnost sa blagim varijacijama rezonantnog vrha. Ova mala promena je rezultat varijacija spoljnih parametara, kao što je sobna temperatura. Gubici u izmerenim vrednostima na near-zero učestanosti su relativno veliki, što je posledica efekta uske cevi u uskom delu Helmholcog rezonatora. Na Slici 11 su prikazani rezultati merenja upoređeni sa rezultatima simulacije sa svim gubicima. Rezultati simulacija i merenja se poklapaju, što potvrđuje naša teorijska predviđanja.

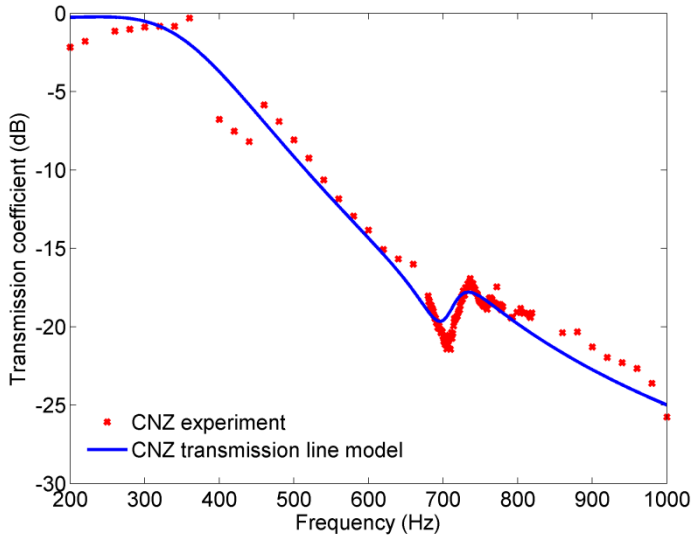

Slika 11 Rezultati merenja upoređeni sa rezultatima simulacije

Nova rezonantna jedinična ćelija sa negativnom gustinom

Kod elektromagnetnih metamaterijala postoje strukture koje daju negativnu permitivnost ili magnetsku permeabilnost po Lorencovom modelu. Ove dve komponente su *split-ring* rezonator (SRR) koji daje negativno μ i komplementarni *split-ring* rezonator (CSRR), koji daje negativno ε. U akustici dosada je postojao samo jedan element koji daje negativan efektivni parameter po Lorencovom modelu, a to je Helmholcov rezonator, koji daje negativnu stišljivost, a nije postojala jedinična ćelija koja proizvodi negativnu gustinu po istom principu. U disertaciji predložena je nova jedinična ćelija sa efektivnom masenom gustinom Lorencovog tipa, tzv. aSRR (akustički *split-ring* rezonator). Predložena jedinična ćelija sa akustičkim ekvivalentnim elementima i poprečni presek su prikazani na Slici 12.

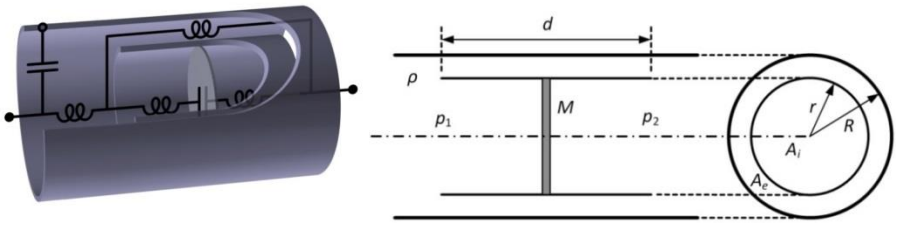

Slika 12 Nova jedinična ćelija (akustički split ring resonator- aSRR)

Nova jedinična ćelija sastoji se od membrane koja je postavljena u koaksijalnu cev. Izvedena je analitička formula za efektivnu gustinu aSRR u slučaju prostoperiodične pobude, koja glasi:

$$\rho_{\text{eff}} \overset{\text{def}}{=} \frac{-\frac{dp}{dz}}{\frac{d^2q}{dt^2}} = \frac{A_e + A_i}{\frac{1}{\rho_0}A_e + \frac{1}{\left(\rho' - \frac{8\pi\tau}{\omega^2 A_i d}\right)}A_i}. \tag{2}$$

Na slici 13 su prikazane ekstrahovana efektivna gustina akustičkog split ring rezonatora upoređena sa efektivnom gustinom dobijanom iz analitičkog izraza (2). U oba slučaja korišćene su sledeće dimenzije: $M = 88\ \mu\text{g}$, $d = 32\ \text{mm}$, $R = 8.1\ \text{mm}$, $r = 3\ \text{mm}$, $\tau = 5\ \text{N/m}$.

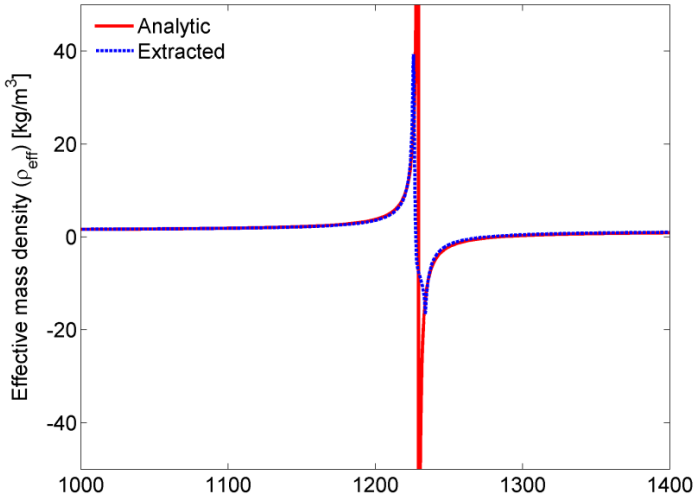

Slika 13 Ekstrahovana efektivna gustina aSRR-a upoređena sa efektivnom gustinom dobijenom iz analitičke formule

Sa Slike 13 se vidi da efektivna gustina ima Lorencov oblik i da jedinična ćelija ima negativnu gustinu u uskom opsegu učestanosti. Prenosna karakteristika strukture je prikazana na Slici 14.

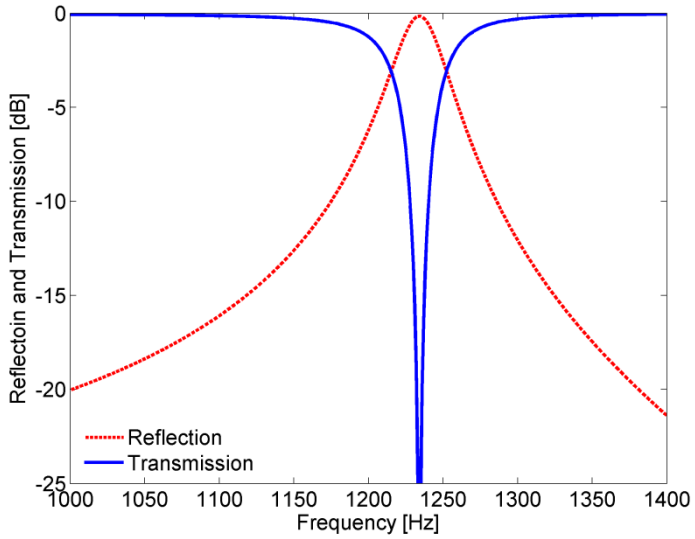

Slika 14 Prenosna karakteristika aSRR-a

Struktura ima nepropusni karakter, pri čemu je nepropusni opseg tačno na učestanosti na kojoj je efektivna gustina manja od nule. Nova jedinična ćelija (aSRR) može se koristiti za realizaciju dvostruko negativnih akustičkih metamaterijala. Kombinacijom aSRRa sa jediničnom ćelijom koja prozvodi negativnu stišljivost može se realizovati u sredini u kojoj se akustički talas prostire sa negativnim talasnim brojem. Na Slici 15 prikazan je novi dvostruko negativan metamaterijal sa aSRRom i otovorima na strani akustičkog voda koji daju negativnu efektivnu stišljivost.

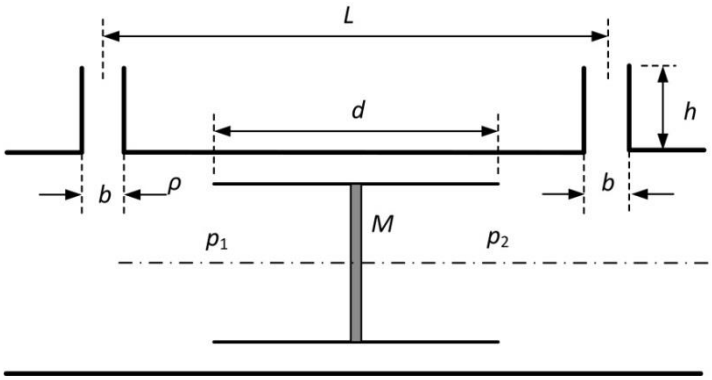

Slika 15 Dvostruko negativan metamaterijal realizovan sa aSRR-om

Dimenzije otvora na strani akustičkog voda su izabrane tako da struktura ima negativnu efektivnu stišljivost u istom opsegu učestanosti u kojem aSRR proizvoidi negativnu gustinu. Dimenzije otvora su $b = 5$ mm, $h =$ 48.95 mm, $L = 34$ mm. Ekstrahovani parametri dvostruko negativnog metamaterijala, efektivna stišljivost, gustina kao i talasni broj u medijumu su prikazani na Slici 16.

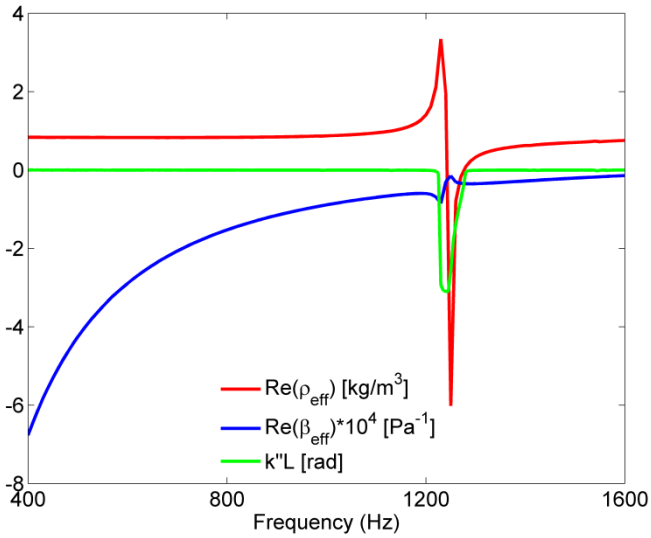

Slika 16 Ekstrahovani efektivni parametri i talasni broj dvostruko negativnog metamaterijala

U frekvencijskom opsegu gde su oba parametara metamaterijala manja od nule, talasni broj metamaterijala je takođe manji od nule, što je dokaz da je sredina dvostruko negativna. Na Slici 17 je prikazan odziv strukture koja ima propusni opseg u opsegu učestanosti u kojem imamo dvostruko negativan metamaterijal.

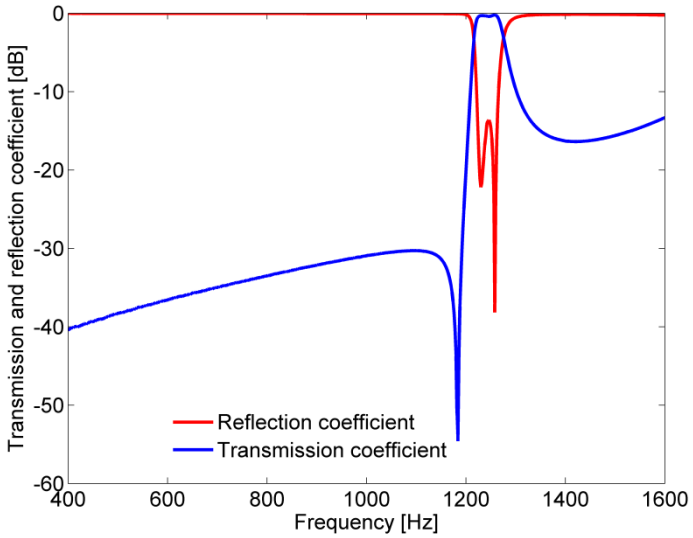

Slika 17 Odziv dvostruko negativnog metamaterijala

Temperaturna kontrola akustičkih površinskih talasa

Na kraju, po prvi put je pokazano da se površinski akustički talas koji se prostire na granici između fluida i čvrste izbrazdane površine može efikasno kontrolisati samo promenom temperature, dok geometrija izbrazdane površi ostaje nepromenjena. Ovo otvara mogućnosti za brojne nove primene, koje se lako podešavaju eksterno. Prateći izloženu teoriju, demostrirali smo zaustavljanje zvuka kontrolisano temperaturom i njegovu primenu u akustičkoj spektralnoj analizi. Takođe, prezentovali smo akustički medijum sa temperaturom kontrolisanim gradijentom indeksa prelamanja i njegovu primenu u temperaturno kontrolisanom akustičkom fokusiranju. Tipična izbrazdana površina sa dimenzijama *d*, *a* i *h*, koje predstavljaju period, širinu i dubinu brazde, redom, prikazana je na Slici 18.

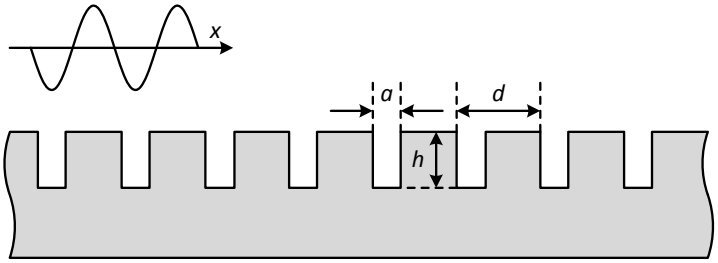

Slika 18 Čvrst material sa izbrazdenim površinom

U slučaju kada je perioda brazde mnogo manja od talasne dužine, medijum se može posmatrati kao efektivna sredina i karakterisati efektivnim parameterima materijala. Temperaturnu zavisnost talasnog broj na površinu u *x* pravcu možemo zapisati kao:

$$k_x(T) = \omega\sqrt{\frac{1}{\kappa RT}}\sqrt{1+\left(\frac{a}{d}\right)^2\tan^2\left(h\omega\sqrt{\frac{1}{\kappa RT}}\right)} \tag{3}$$

gde je R specifična gasna konstanta, T je apsolutna temperatura, κ je adiabadska konstanta i a, d, h su geometrijski parametri izbrazdane površine. Disperziona karakteristika na različitim temperaturama za slučaj kada su geometrijski parametri proizvoljno izabrani i jednaki a = 0.2 mm, d = 1 mm, and h = 24 mm je prikazana na Slici 19.

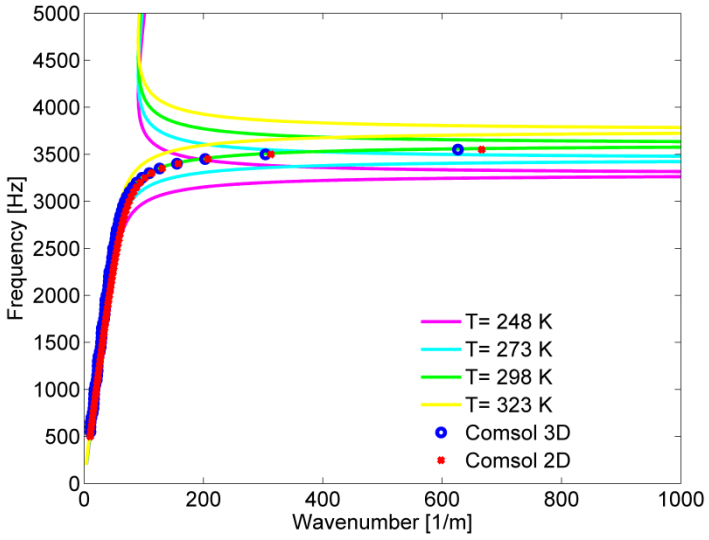

Slika 19 Disperzioni dijagram površinskog talasa na različitim temperaturama

Sa grafika se vidi da se temperaturom okoline može kontrolisati disperziona kriva, pa tako i prostiranje. Na manjim učestanostima sredina nije disperzivna i talasni broj na površini se poklapa sa talasnim brojom u sredini, dok na višim učestanostima u zavisnoti od temperature i od geomaterijskih parameter izbrazdane površine talasni broj brzo počinje da raste i teži do beskonačnosti. Kako talasni broj teži beskonačnosti, talasna dužina i brzina prostiranja teže nuli, i više nije dozvoljeno prostiranje talasa na površini. Na Slici 20 je prikazana promena talasnog broja u zavisnosti od temperature kada je učestanost prostiranja konstantna.

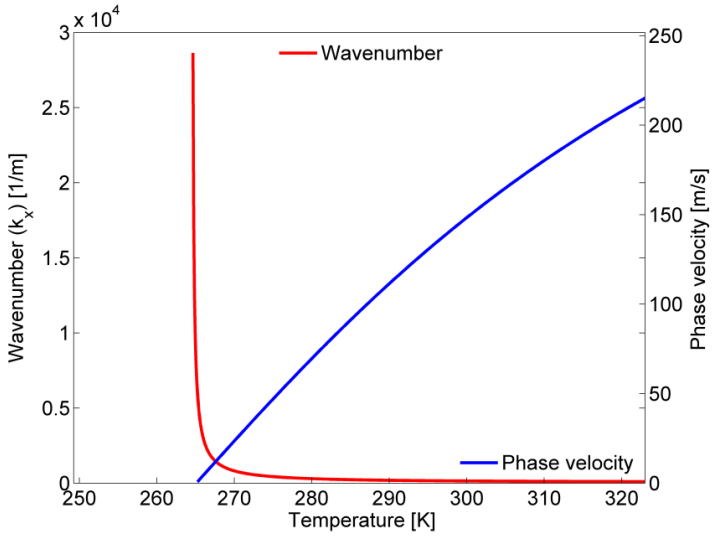

Slika 20 Talasni broj u funkciji temperature

Pri konstantnoj učestanosti u zavisnosti od temperature talasni broj teži beskonačnosti. Vrednost temperatura za koju talasni broj asimtotski dostigne beskonačnost naziva se kritična temperatura i može izračunati pomoću sledeće formule:

$$T_c = \frac{16h^2 f^2}{\kappa R}, \tag{4}$$

gde je f operativna učestanost, h je dubina kanala, R je specifična gasna konstanta gasa u okolini, a κ je adiabadska konstanta. Ova vrednost je teorijska i može se postići ako je perioda beskonačno mala, zato što smanjenjem talasne dužine efektivna sredina i perioda neće biti manje od talasne dužine. Na Slici 21 prikazan je intenzitet zvuka u zavisnosti od temperature, u slučaju kada je perioda strukture promenljiva, a disperzija ista (*a/d=konst.*).

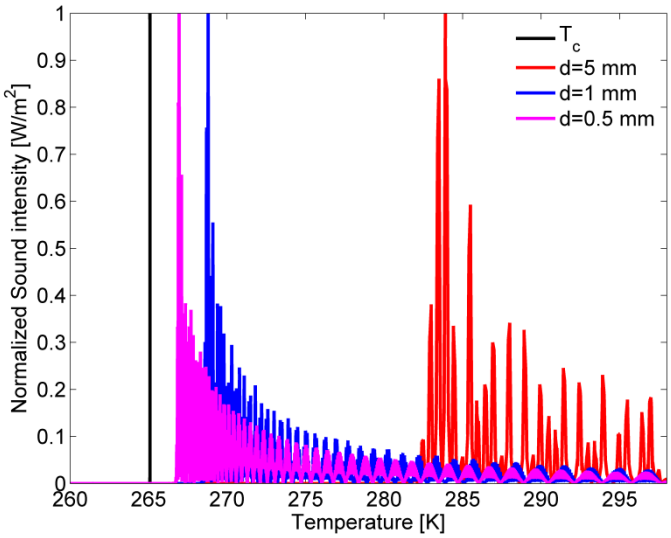

Slika 21 Normalizovan intenzitet zvuka u zavisnosti od temperature sa različitim periodima brazde

Vidi se da smanjenjem periode, tačka gde je talas zaustavljen (intenzitet zvuka maksimalan) konvergira do kritične temperature. Tačka gde je talas zaustavljen je tačno tamo gde se struktura više ne može posmatrati kao efektivna sredina i to tačno gde je talasni broj $k_x < \pi/2d$. Primenom linearno promenljive temperature sa različitim gradijentom po dužini strukture talas se može zaustaviti na različitim mestima po dužini, a tačka zaustavljanja je uvek tamo gde je temperatura jednaka kritičnoj temperaturi. To je prikazano na Slici 22.

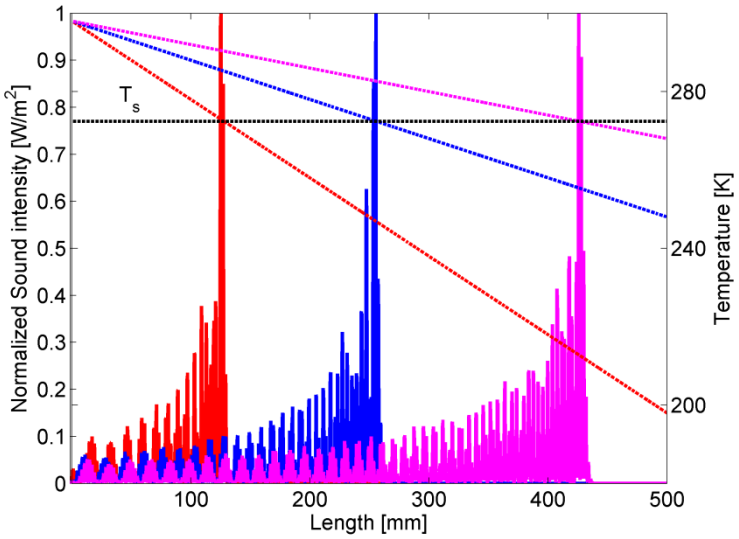

Slika 22 Zaustavljanje zvuka na različitim mestima pomoću različite temperaturne raspodele

Kao što se vidi iz izraza (4) kritična temperatura zavisi i od radne učestanosti, pa se u slučaju da talas nije prostoperiodičan, pomoću lineranog gradijenta temperature po dužinu strukture može razdvojiti na svoje prostoperiodične komponente i koristiti kao analizator spektra, Slika 23.

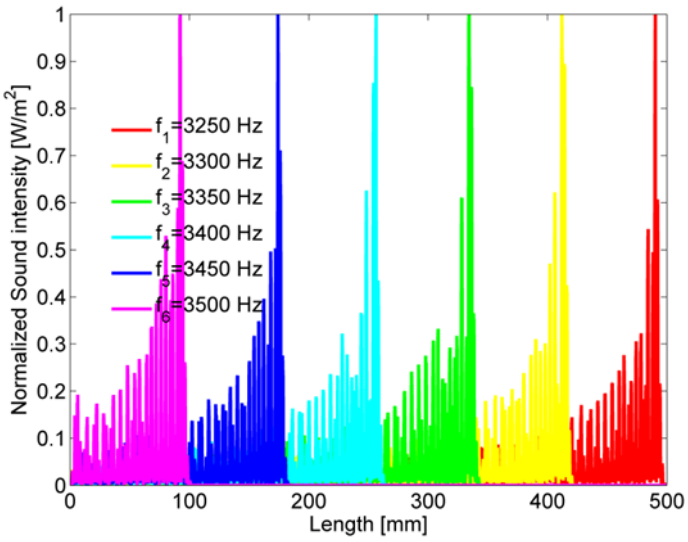

Slika 23 Razdvajanje složenog talas na prostoperiodične komponente pomoću linerane raspodele temperature po dužinu strukture

Do sada temperaturne promene smo primenili samo u pravcu prostiranja akustičkog površinskog talasa, ali to nije jedina mogućnost. Mogu se primeniti različiti temperaturni profili normalno na pravac prostiranja površinskih akustičkih talasa. Ovako dobijen medijum je medijum sa gradijentom indeksa prelamanja (GRIN), kod kojih se indeks prelamanja menja po dimenzijama po odgovarajućem profilu. Kontrolisanjem temperature omogućavamo da ovaj GRIN medijum bude promenljiv, tj. istim dimenzijama stukture dobijamo različite funkcije sitema. Korišćena su dva

različita profila, profil za savijanje površinskih talasa pod definisanim uglom i sočivo za fokusiranje ravanskih talasa u jednu tačku. Za savijanje talasa korišćen je profil:

$$n(x) = 1 + \frac{n_{max} - 1}{w} x, \tag{5}$$

gde je w širina sočiva, a n_{max} je maksimalna vrednost indeksa prelamanja u GRIN medijumu. Ugao savijanja je funkcija širine i debljina sočiva i maksimalna vrednost indeksa prelamanja može se izračunati kao:

$$n_{max} = \frac{w}{t} \sin \Theta + 1. \tag{6}$$

Iz vrednosti indeksa prelamanja može se izračunati odgovarajuća temperatura. U COMSOL modelu GRIN medijum je podeljen na 50 malih kanala koji imaju iste dimenzije, a na svim kanalima različita je tempreatura. Temperatura zavisi od željene primene. Raspodela temperature i raspodela faze akustičkog pritiska u GRIN medijumu u slučaju savijanja (Θ=30°) prikazane su na Slici 24.

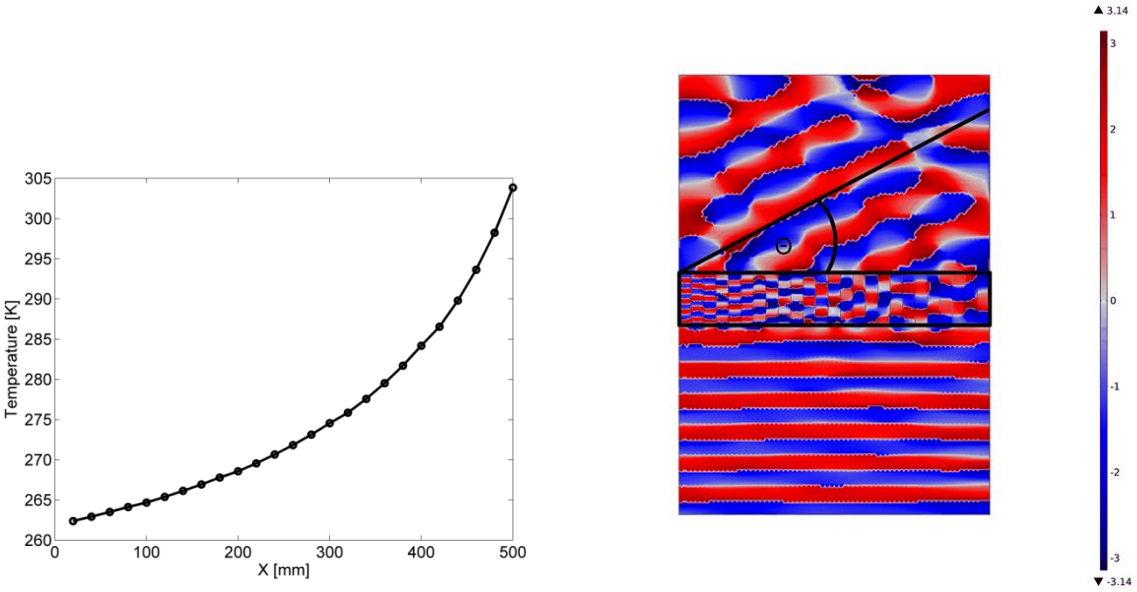

Slika 24 Raspodela temperature u GRIN medijumu i raspodela akustičkog pritiska na površinu

Na Slici 24 je prikazano kako se ravanski talas koji upada u GRIN medijum na izlazu savije pod odgovarajućim uglom Θ. Korišćen profil za fokusiranje talasa u jednu tačku je hiperbolik sekant raspodele indeksa prelamanja koji je dat izrazom

$$n(x) = n_0 \operatorname{sech}(\alpha x) \tag{7}$$

gde je n_0 indeks prelamanja u centru sočiva, a α gradijent parametar. Iz vrednosti indeksa prelamanja može da se izračuna odgovarajuća temperatura. Na Slici 25 je prikazana raspodela temperature u slučaju kada je indeks prelamanja u centru sočiva n_0 = 1.5, a sa strane n_w = 1. Na Slici 25 je prikazana raspodela temperatura u GRIN medijumu i intenzitet akustičkog talasa na površini.

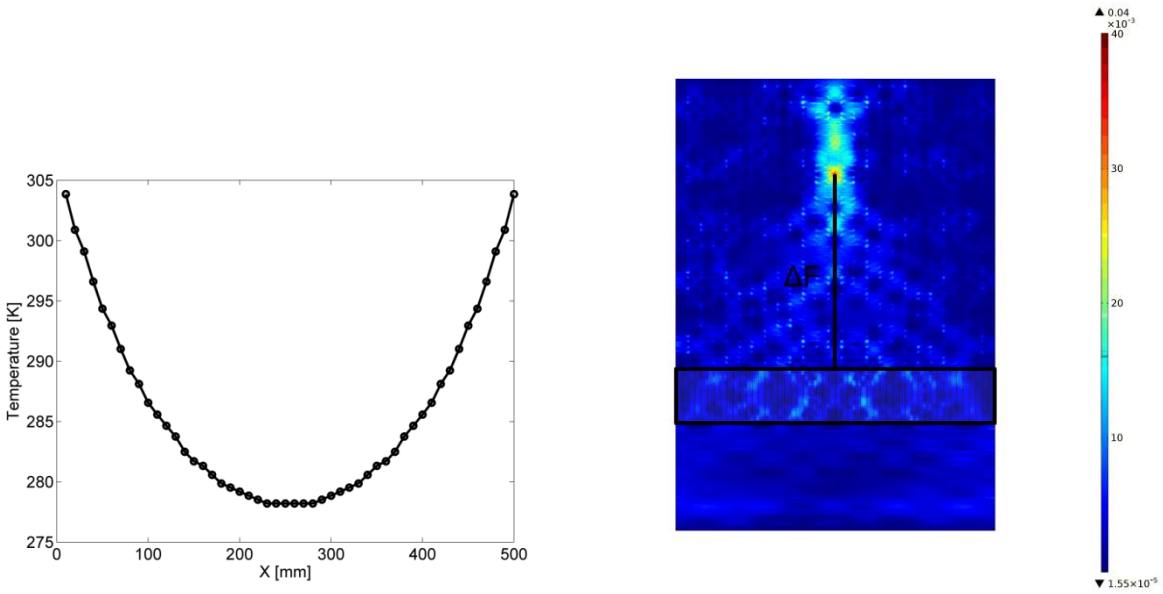

Slika 25 Raspodela temperature u GRIN medijumu i intenzitet akustičkog talasa na površini

Sa slike 25 vidi se da je intenzitet fokusiran u jednu tačku. Žižna daljina u ovom slučaju je $\Delta F =$ 360 mm, i može se proizvoljno promeniti promenom temperature u GRIN medijumu.

Table of contents

1. Introduction

The concept of metamaterials has opened a new perspective to looking at nature, and from this point of view one can realize phenomena which were impossible before, such as hyperlenses which break a diffraction limit or devices acting as cloaks of invisibility. At first metamaterials were used in electromagnetics and in optics but today the field of application of this concept is much wider. Today we encounter this term in a range of fields, from electromagnetics to acoustic and mechanics, and lately even in thermal application. Acoustic metamaterials are artificially created structures that allow the propagation of acoustic waves characterized with properties that are not found in nature. The development of acoustic metamaterials has been based on the existing knowledge about electromagnetic metamaterials and the analogies between acoustic, mechanical and electrical quantities. This area has great potential for both scientific research and for specific applications. For example, in recent years researchers have realized nonreciprocal acoustic devices such as acoustic diodes or acoustic circulators or acoustic cloaking devices which make objects undetectable with sound – all these devices are based on the metamaterial and effective medium concept. In this thesis we explore the topic of acoustic metamaterials, their design, analysis and applications of different types of non-conventional acoustic wave propagation in different artificial media comprised of metamaterial unit cells.

The thesis consists of nine chapters including the introduction and the concluding chapter, and can be separated into two sections. In the first section we realize and analyze different types of non-conventional acoustic wave propagation in 1D metamaterial media. In the second section we describe the propagation of acoustic surfaces on grooved surfaces and discuss ways to control it.

After the introduction, the second chapter gives a short overview of the theory of acoustic wave propagation and also gives basic concepts related to electroacoustic analogies and the theory of acoustic transmission lines.

The third chapter gives an overview of the proposed state-of-the-art metamaterial unit cells, single negative and double negative acoustic metamaterials and their applications.

The fourth chapter describes developed methods and models during research into the behavior of metamaterial unit cells in acoustic systems, including a method for the calculation of acoustic scattering parameters and a method for the extraction of effective material parameters of metamaterial unit cells. The principles of finite element method modeling of acoustic metamaterials in COMSOL Multiphysics simulator and a mathematical model based on the transmission line theory are also described in this chapter.

The fifth chapter describes a novel type of wave propagation, so called near zero propagation, which is wave propagation without phase change along the structure. In this type of metamaterials the main design criterion is that one of the two constitutive parameters (in the acoustic case density and compressibility) has to be equal or close to zero. Here we analyze compressibility near-zero

propagation realized using Helmholtz resonators. Beside the theoretical analysis, we also present numerical modeling results and an experimental verification of the structure, which is consistent with the theoretical predictions.

The sixth chapter describes a new resonant type acoustic metamaterial unit cell with negative density on a certain frequency range. The unit cell is analyzed theoretically and an expression for frequency dependent effective density is derived. The theoretical analysis is verified through a range of simulation models. In the end of the chapter possible applications of the new unit cell are given, such as a double negative single or dual band acoustic bandpass filter design. A new approach to obtain density near-zero propagation using the novel unit cell is also demonstrated.

Chapter seven, the opening chapter of the second section, gives the theory of acoustic wave propagation on grooved hard surfaces as well as an overview of the proposed state-of-the-art structures to control the wavenumber of the surface acoustic waves by changing geometrical parameters of the grooves. Possible applications, such as sound wave collimation or spatial spectral analysis, are also presented.

Chapter eight expands the opportunities for surface wave control on grooved surface. The principle and the concept for surface wave control by changing the parameters of the surrounding medium and without changing the geometrical parameters are also given. Temperature inequalities in the host medium affect the surface acoustic wave propagation constant, which means that the surface can be used as a temperature sensing element, or as a spatial acoustic spectrograph tunable by modifying only the temperature gradient along the structure, rather than any geometrical change of the structure. It is shown that by changing only the temperature distribution in the surrounding fluid medium the direction of the wave propagation can be controlled. It is also shown that using different temperature distribution profiles, the structure with constant geometrical parameters can be used to realize tunable applications such as bending acoustic surface waves or their focusing with tunable focal length.

The ninth chapter gives a general conclusion of the thesis, and is followed by Appendices.

The appendices A1 to A6 give Matlab codes related to numerical modeling, the extraction of effective parameters, calculation of scattering parameters as well as calculation of temperature distributions in appropriate structures.

The concluding section offers an overview of the literature referenced in the thesis.

2. Acoustic wave propagation

Mechanical waves are oscillations of particles in a continuous medium. They may be transversal, when the particle oscillation is in the direction perpendicular to the propagation direction, and longitudinal, when oscillation is performed in the direction of wave propagation [1]. Acoustical waves (sound waves) are longitudinal mechanical waves. Sound propagation exists in gaseous, liquid and in solid areas, in vacuum there is no sound propagation because there are no particles [2-5]. Acoustics is used in numbers of important applications, including electro-acoustic transducers such as microphones and loudspeakers, surface-acoustic-wave (SAW) devices are used as radio-frequency (RF) filters [6-7], acoustic-wave modulators diffract optical beams for real-time spectral analysis of RF signals [8], while mechanical crystal oscillators currently control the timing of most computers and clocks [9].

2.1 Acoustic wave equation

When a sound wave propagates, the particles of the medium undergo vibrations about their mean positions. In some regions they may be pushed together, whereas in others they are pulled apart. Once the wave has passed, the particles return to their original state. Consequently, the variations of both pressure and velocity occur as functions of time and space. Sound pressure is defined as the difference between the instantaneous pressure and the atmospheric static pressure. Pressure fluctuations that create audible noise are extremely small when compared to atmospheric pressure. The velocity of particle displacement is yet another important quantity characterizing a travelling sound wave. Pressure waves propagate through air without appreciable heat transfer taking place, i.e. acoustic processes are adiabatic. The wave equation in an ideal fluid can be derived from hydrodynamics. The linearized equation for conservation of mass and linearized Euler's equation (Newton's second law) are [1-5]:

$$\rho_0 \nabla \cdot \vec{v} = -\frac{\partial \rho}{\partial t} \tag{2.1}$$

$$\nabla p = -\rho_0 \frac{\partial \vec{v}}{\partial t} \tag{2.2}$$

where p is acoustic pressure, $\vec{v}$ is particle velocity, ρ_0 is the density of the environment (air) in which the acoustic wave propagates and ρ is the density. Newton's law (2.2) states that the pressure gradient will induce mass acceleration, while conservation of mass (2.1) states that velocity divergence is proportional to the negative time derivative of mass density. These two basic equations involve three variables: p, $\vec{v}$ and ρ; we need the acoustic constitutive relation to reduce this set to two variables. Most acoustic waves involve frequencies sufficiently high that the heating produced by wave compression has no time to escape by conduction or radiation, and thus this heat energy returns to the wave during the subsequent expansion without significant loss. Such adiabatic processes involve no heat transfer across populations of particles. The resulting adiabatic acoustic constitutive relation

states that the fractional change in density equals the fractional change in pressure, divided by the constant γ, called the adiabatic exponent:

$$\frac{\partial \rho}{\partial p} = \frac{\rho_0}{\gamma P_0} \tag{2.3}$$

where P_0 is the total pressure; that is, the acoustic pressure added to atmospheric pressure. After combining Eqs. (2.1) and (2.3) the mass conservation equation can be written in the form:

$$\nabla \cdot \vec{v} = -\beta \frac{\partial p}{\partial t} \tag{2.4}$$

where β is the compressibility of the material, equal to the reciprocal value of the bulk modulus:

$$\beta = \frac{1}{B} = \frac{1}{P_0 \gamma} \tag{2.5}$$

From Eqs. (2.2) and (2.4) the acoustic wave equation can be derived. The acoustic wave equation for acoustic pressure is:

$$\nabla^2 p = \frac{1}{c^2} \frac{\partial^2 p}{\partial t^2} \tag{2.6}$$

The wave equation for a particle velocity has a same form and is given by:

$$\nabla^2 \vec{v} = \frac{1}{c^2} \frac{\partial^2 \vec{v}}{\partial t^2} \tag{2.7}$$

These are the linear acoustic wave equations. Here:

$$c = \sqrt{\frac{P_0 \gamma}{\rho_0}} = \frac{1}{\sqrt{\beta \rho}} \tag{2..8}$$

is the speed of sound in air. The speed of sound is constant and independent from the frequency in dispersionless case. Since the entire sound field varies as $e^{j\omega t}$, the operator $\partial/\partial t$ can be replaced by $j\omega$ (because the derivative of $e^{j\omega t}$ with respect to time is $j\omega e^{j\omega t}$), and the operator $\partial^2/\partial t^2$ can be replaced by $-\omega^2$. Eqs (2.2) and (2.4) can thus be written in the form:

$$\nabla p = -j\omega \rho \vec{v} \tag{2.9}$$

$$\nabla \cdot \vec{v} = -j\omega \beta p \tag{2.10}$$

By solving this system the Helmholtz equations for p and $\vec{v}$ are obtained:

$$\nabla^2 p + k^2 p = 0 \tag{2.11}$$

$$\nabla^2 \vec{v} + k^2 \vec{v} = 0 \tag{2.12}$$

From the above expressions the wave number for a medium is:

$$k = \omega \sqrt{\beta \rho} \tag{2.13}$$

In a lossy medium the wavenumber has a complex value, where the real part is the attenuation coefficient and the imaginary part is the propagation constant in the medium. The phase velocity of the acoustic wave can be calculated as a ratio between the frequency and the wavenumber:

$$v_p = \frac{\omega}{k} = \sqrt{\frac{1}{\beta\rho}} \tag{2.14}$$

In a non-dispersive medium the acoustic phase velocity is equal to the speed of sound (2.8). The solutions of the Helmholtz equation provide all solutions of the wave equation. Direction of the acoustic wave propagation is the same as the direction of particle velocity. The intensity of the acoustic wave is defined as the product of the sound pressure and the particle velocity:

$$\vec{I} = p\vec{v} \tag{2.15}$$

2.1.1 Analogy between acoustic and electromagnetic waves

Differential equations (2.2) and (2.4) are roughly analogous to Maxwell's Eqs. (2.16) (Faraday's law) and (2.17) (Ampere's law) [10-11], and can be combined:

$$\nabla \times \vec{E} = -\mu \frac{\partial \vec{H}}{\partial t} \tag{2.16}$$

$$\nabla \times \vec{H} = \varepsilon \frac{\partial \vec{E}}{\partial t} \tag{2.17}$$

With laws that are listed above we can establish the analogy between acoustic and electromagnetic waves. Unlike electromagnetic waves, where the key fields are vectors transverse to the direction of propagation, the velocity vector for acoustic waves is in the direction of propagation and the pressure is a scalar. An analogy between electrical and acoustic quantities can be established when one of the fields (electric or magnetic) has just one directional component. Special polarizations like TM or TE propagation modes in waveguides fulfill this condition. Analogies between the corresponding acoustic and electrical quantities in TE and TM propagation modes are given in Table 2.1 and Table 2.2 respectively.

TABLE 2.1 ANALOGY BETWEEN ACOUSTIC AND ELECTROMAGNETIC QUANTITIES (TE MODE)

Acoustic	Electromagnetic	Analogy
Acoustic pressure p	Electric field E_z	$p \leftrightarrow E_z$
Particle velocity v_x, v_y	Magnetic field H_x, H_y	$-v_x \leftrightarrow H_y, v_y \leftrightarrow H_x$
Density ρ_x, ρ_y	Permeability μ_x, μ_y	$\rho_x \leftrightarrow \mu_y, \rho_y \leftrightarrow \mu_x$
Compressibility β	Permittivity ε_z	$\beta \leftrightarrow \varepsilon_z$

TABLE 2.2 ANALOGY BETWEEN ACOUSTIC AND ELECTROMAGNETIC QUANTITIES (TM MODE)

Acoustic	Electromagnetic	Analogy
Acoustic pressure p	Magnetic field H_z	$p \leftrightarrow H_z$
Particle velocity v_x, v_y	Electric field E_x, E_y	$-v_x \leftrightarrow E_y, v_y \leftrightarrow E_x$
Density ρ_x, ρ_y	Permittivity ε_x, ε_y	$\rho_x \leftrightarrow \varepsilon_y, \rho_y \leftrightarrow \varepsilon_x$
Compressibility β	Permeability μ_z	$\beta \leftrightarrow \mu_z$

The first set are the transverse magnetic (TM or p) modes, where only the field components E_x, E_y and H_z are nonzero, and the second set are the transverse electric (TE or s) modes, with only H_x, H_y and E_z being nonzero.

2.2 Acoustic circuit elements

A close analogy can be established between the propagation of sound in pipes and chambers and electrical circuits, which is a great aid in acoustical problems of many kinds, since all electrical circuit theorems may be applied [13-15]. When the dimensions of the region in which the sound propagates are much smaller than the wavelength, the flow is almost incompressible, and a lumped-parameter model is appropriate. On the other hand, a long pipe is the acoustical analogue of an electrical transmission line, specified with distributed parameters. The important acoustic variables will be taken to be the acoustic pressure p, and the volume velocity (volumetric flow) Q. Q is a conserved quantity, from the conservation of mass combined with the approximate constancy of the density. It would be more rigorous to use the mass rate of flow, but the volume rate of flow is equivalent in these problems. The product of p and Q has dimensions $(N/m^2)(m^3/s)$ = watt, and is a power, just like the product of voltage V and electrical current I. For the electro-acoustic analogy, we can take $p \leftrightarrow V$ and $Q \leftrightarrow I$, which is a so-called impedance analogy. Another analogy between acoustic and electrical parameters is a mobility analogy where $Q \leftrightarrow V$ and $p \leftrightarrow I$. Since the product of the voltage and current is power, as well as acoustic pressure and volumetric flow, this is consistent. If p and Q are phasor quantities, the ratio p/Q is analogous to the electrical impedance and it is called the acoustic impedance Z_a. Similarly to electrical impedance, acoustic impedance can be written in a general form as:

$$Z_a = R_a + j\left(\omega m_a - \frac{1}{\omega C_a}\right) \tag{2.18}$$

which defines acoustical resistance (R_a) with unit [$\mathrm{Nsm^{-5}}$], acoustic inductance (acoustic mass, m_a) with unit [$\mathrm{kgm^{-4}}$] and acoustic capacitance (C_a) with unit [$\mathrm{m^4s^2kg^{-1}}$]. Let us first consider a system of passageways and volumes whose maximum dimensions are much smaller than the wavelength. Lumped parameter results will be approximately valid if this dimension is taken to be less than $\lambda/4$. The essential assumption here is that the phase is approximately constant throughout the system.

2.2.1 Acoustic inductance

Let us consider the air in a section of a tube of length L and cross section area S (Fig. 2.1). Since all quantities are in phase, it moves as a rigid body with displacement ξ under the action of an unbalanced force $(p_1-p_2)S=pS$, the difference in the pressure on its ends.

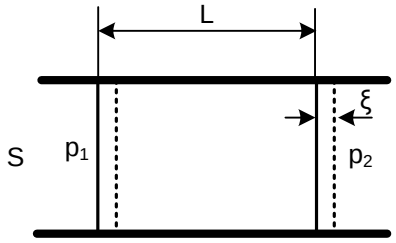

Figure 2.1 Short section of tube (acoustic inductance)

Mass of the air in the tube is ρSL and the acceleration is $\frac{dv}{dt}$ or $\frac{d^2\xi}{dt^2}$ so the second Newton's law can be written as

$$Sp = \rho SL\frac{dv}{dt}. \tag{2.19}$$

Dividing both sides of Eq.(2.19) by S and using volume flow instead of velocity it can be rewritten to:

$$p = \frac{\rho L}{S}\frac{dQ}{dt} \tag{2.20}$$

From the expressions (2.20) using impedance analogy the acoustic mass is:

$$m_a = \frac{\rho L}{S} \tag{2.21}$$

In case of sinusoidal excitation the velocity is $v = j\omega\xi$, so $p = j\omega(\rho L/A)Q$. Thus the acoustic impedance is:

$$Z_m = j\omega m_a \tag{2.22}$$

Acoustical inductance is the consequence of the kinetic energy of the air. This energy is, in fact, on the average equal to:

$$E = \frac{1}{2}m_a Q^2 \tag{2.23}$$

analogous to $(1/2)LI^2$ for the electrical quantities.

2.2.2 Acoustic capacitance

In Fig 2.1 a rigid container of volume V filled with air is shown. Air can enter or leave at the rate Q from an opening in the container, compressing or rarefying the air in the container, without producing significant velocity. The volume change of the air is ΔV (not a change in the size of the volume), so that the compression is equal to $s = -\Delta V/V$.

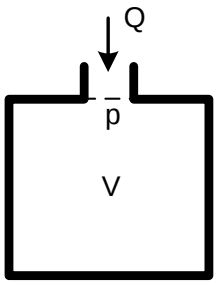

Figure 2.2 Rigid container filled with air (acoustic capacitance)

In terms of sinusoidal excitation the volumetric flow Q, $\Delta V = Q/j\omega$. Using the compressibility of air, ρc^2, it can be found that

$$p = \frac{\rho c^2}{j\omega V} Q \tag{2.24}$$

Acoustic impedance from Eq. (2.24) for the air filled container is

$$Z_C = \frac{1}{j\omega C_a} \tag{2.25}$$

where C_a is the acoustic capacitance, equal to:

$$C_a = \frac{V}{\rho c^2} \tag{2.26}$$

where c is the speed of sound in a given environment (air), ρ is the density of the environment (air), and V is the volume of the container. Again, this is completely analogous with electrical capacitance, and the energy stored in acoustic capacitance is

$$E = \frac{1}{2} C_a p^2 \tag{2.27}$$

Both L_a and C_a correspond to energy storage.

2.2.3 Acoustic resistance

With acoustic resistance R_a we can model losses in the acoustic systems, for example viscous frictions. The layout of the acoustic resistive tube is shown in Fig. 2.3.

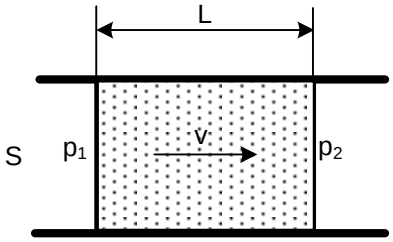

Figure 2.3 Short section of tube filled with viscous material

where S is a cross section area of the tube, v the particle velocity in viscous medium, p_1 and p_2 are the pressures between the ends of the resistive tube section and L is the length of the tube. In viscous flow, the particle velocity is proportional to the pressure gradient,

$$Q = vS = \frac{kS}{L}p \tag{2.28}$$

where p is the pressure difference ($p = p_2 - p_1$). Therefore, the acoustic resistance is

$$R_a = \frac{L}{kS} \tag{2.29}$$

The parameter k is the permeability, which represents the capacity for flow through porous material. Since $p = R_aQ$, the power dissipation is $P = Q^2R_a$. If the element is a capillary tube, the flow is viscous if the Reynolds number $Re = \rho vL/\eta$ is sufficiently small (less than 2000), where η is the dynamic viscosity of air, which is approximately independent of pressure. Poiseuille's formula for flow in a capillary is:

$$Q = \left(\frac{\pi a^4}{8\eta L}\right)p \tag{2.30}$$

where a is the radius of the capillary of length L. This yields the acoustic resistance:

$$R_a = \frac{8\eta L}{\pi a^4} \tag{2.31}$$

2.2.4 Acoustic transmission line

Based on the analogy given in the previous section, we can draw a unit cell of the lossless acoustic transmission line, a short section of tube can be modeled with lumped parameters, as shown in Fig. 2.4, long tube is modeled as a cascade of such sections.

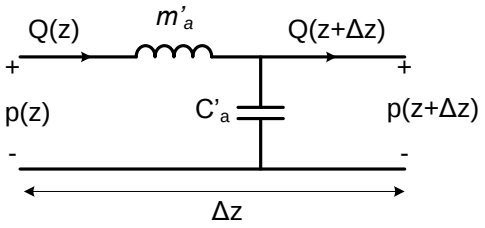

Figure 2.4 Model of the short section of the acoustic transmission line

The acoustic transmission line is an ordinary tube that is filled with air or some other fluid material, length of the tube is much longer than the guided wavelength and cannot be modeled with lumped elements. The acoustic transmission line is a network with distributed parameters, in which the amplitude and phase of pressure and volumetric flow changes along the acoustic transmission line. Unit length short section of the acoustic transmission line can be modeled with lumped elements of acoustic parameters which are given in the previous sections (acoustic mass and acoustic capacity). Unit-length acoustic mass and unit-length acoustic capacity are defined as:

$$m_a' = \frac{\rho}{S} \tag{2.32}$$

$$C_a' = \frac{S}{\rho c^2} \tag{2.33}$$

where ρ is the density of the material with which the tube is filled, S is the cross-section area of the acoustic tube, c is the speed of sound in a given environment. Through these parameters unit length acoustic mass and acoustic capacity of a short section of transmission line can be defined:

$$m_a = m_a' \Delta z \tag{2.34}$$

$$C_a = C_a' \Delta z \tag{2.35}$$

From Fig. 2.4, and if it is assumed that $\Delta z \to 0$, the differential equations for the pressure and flow of the acoustic transmission line in case of acoustic sinusoidal excitation are:

$$\frac{dp(z)}{dz} = -j\omega m_a' Q(z) \tag{2.36}$$

$$\frac{dQ(z)}{dz} = -j\omega C_a' p(z) \tag{2.37}$$

Eqs. (2.36) and (2.37) may be combined and rewritten into wave equations, one for p and one for Q:

$$\frac{d^2p(z)}{dz^2} - \gamma^2 p(z) = 0 \tag{2.38}$$

$$\frac{d^2Q(z)}{dz^2} - \gamma^2 Q(z) = 0 \tag{2.39}$$

where $\gamma = j\omega\sqrt{m_a' C_a'}$ is the propagation constant in acoustic transmission line. The solution in phasor form is:

$$p(z) = p_0^+ e^{-\gamma z} + p_0^- e^{+\gamma z} \tag{2.40}$$

$$Q(z) = Q_0^+ e^{-\gamma z} + Q_0^- e^{+\gamma z} \tag{2.41}$$

where $e^{-\gamma z}$ is the wave component which propagates to positive z direction, and the $e^{\gamma z}$ is the wave component which propagates to negative z direction. Hollow cylindrical tube, open at one end and closed at the other end with impedance Z_{AL} is shown in Fig. 2.5. If an incident wave travels in the positive z direction p_{ai}, when the wave reaches the point $x=L$, a reflected wave traveling in the negative x direction will in general be produced p_{ar}.

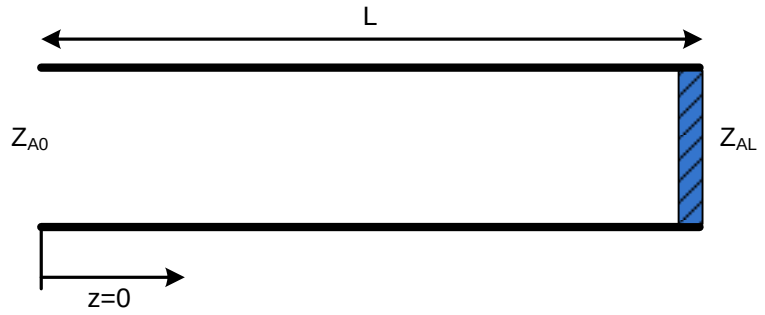

Figure 2.5 Acoustic transmission line closed with acoustic impedance Z_{AL}

Pressure and volumetric flow represent a sum of incident and reflected waves. Reflection from the end of the tube will be zero only in the case when the acoustic impedances are matched: $Z_{AL} = Z_{A0}$. Therefore, the input impedance of the transmission line depends on its length. The impedance at the distance L from the load is:

$$Z_{Ain} = Z_{A0} \frac{Z_{AL} + jZ_{A0} \tan(\gamma L)}{Z_{A0} + jZ_{AL} \tan(\gamma L)} \tag{2.42}$$

where Z_{AL} is load impedance, L is the length, γ is the propagation constant in the tube, and Z_{A0} is the characteristic acoustic impedance of the acoustic transmission line, defined as:

$$Z_{A0} = \sqrt{\frac{m'_a}{C'_a}} \tag{2.43}$$

Based on expressions (2.32) and (2.33), characteristic acoustic impedance can be written as:

$$Z_{A0} = \frac{\rho c}{S} \tag{2.44}$$

3. Acoustic metamaterials

The term metamaterial refers to a medium composed of subwavelength unit cells, specifically engineered to exhibit unusual properties in relation to wave propagation, generally not found in nature. Most research in this area has been dedicated to electromagnetic metamaterials, which offer the possibility of engineering effective permeability and permittivity, resulting in phenomena such as negative phase velocity, superlensing and cloaking [16-26]. However, in recent years a lot of attention has also been given to the study of acoustic metamaterials, where specific design is deployed to control the values of effective compressibility and mass density [27-39]. Similar phenomena like in electromagnetics can be achieved with acoustic metamaterials too, including acoustic superlensing [40-46], acoustic cloaking [47-59] negative phase velocity [60-64], nonreciprocal propagation of acoustic wave [65-67].

3.1 Introduction to acoustic metamaterials

Behavior of acoustic waves in fluid media can be described with two material parameters: density and compressibility. Using the effective medium theory and different design techniques any value of effective density or compressibility can be achieved with metamaterials, and wave propagation in a metamaterial medium can be controlled in an arbitrary way. Depending from the values of the effective density and effective compressibility of the metamaterials, they can be divided into classes such as metamaterials with a very large density (VLD), metamaterials with a very large compressibility (VLC), density near zero metamaterials (DNZ), or compressibility near zero metamaterials (CNZ). Using the concept of metamaterials, one can also obtain effective media with negative dynamic mass density or with negative compressibility. Metamaterials with one negative effective parameter are called single negative metamaterials (SNG). In the case of SNG metamaterials the wavenumber is purely imaginary, which means that the wave propagation is not possible, and that just the evanescent (exponential decay) modes can be observed. A special types of metamaterials are double negative (DNG) metamaterials. These types of metamaterials are characterized by both effective material parameters being negative, i.e. within a certain frequency range both the effective mass density and the effective compressibility are below zero. The first theoretical paper about these kinds of materials was written by Victor Veselago in 1967 [16]. He has shown that in a double negative electromagnetic medium the wave propagation is possible, but with a negative wavenumber, implying that the phase and the group velocity are antiparallel. When the phase velocity is negative the acoustic refractive index also has a negative value. Acoustic refractive index on the boundary of the air and another medium can be defined as:

$$n = \frac{c}{v_\phi} \tag{3.1}$$

where c is the speed of sound in the air and v_ϕ is the phase velocity in the second medium. In the situation when the second material is double negative and its phase velocity v_ϕ is below zero, the refractive index *n* is also negative, which is why this type of materials also called negative refractive index materials (NRI). From this it follows that some of the well-known physical principles, such as the Snell's law and the Doppler effect, are apparently reversed. Snell's law describes the refraction on the boundary of two isotropic media:

$$\frac{\sin\theta_i}{\sin\theta_t} = \frac{n_1}{n_2} \tag{3.2}$$

If the medium 2 is double negative, the refractive index is below zero (n_2<0) and from Snell's law it follows that the angle of refraction is also below zero (θ_t <0). From theoretical analysis it follows that by combining different signs of effective density and effective compressibility of the metamaterials different types of wave propagation can be obtained. When both parameters are positive the wave propagation is possible and the group and the phase velocity has the same direction. This is the case of conventional wave propagation with a real positive wavenumber. On the other hand, when both parameters are negative, the wave propagation is also possible but with a negative real wave number and with antiparallel phase and group velocity. This case is referred to as double negative or "left-handed" propagation. When the effective density and compressibility have different signs, only evanescent mode propagation exists, because the wavenumber is purely imaginary, i.e. it does not have a real component.

3.2 Resonant type acoustic metamaterials

3.2.1 Metamaterials based on Helmholtz resonator

Helmholtz resonator is a well-known acoustic resonance structure, consisting of a cavity of known volume with rigid walls connected to the host structure by a neck of known length and cross-sectional area. A typical Helmholtz resonator is shown in Fig. 3.1. In the equivalent electrical circuit of the resonator, the compliance of the fluid in the cavity to adiabatic compression and rarefaction can be modelled as acoustic compliance $C_r \propto V/\rho c^2$, while the inertia of the plug of fluid oscillating in the neck can be modelled as inductance $L_r \propto \rho l/S$, where V is the volume of the cavity, ρ is the density of the fluid, c is the velocity of sound, l is the effective length of the neck and S its cross-sectional area. The resonance in the Helmholtz resonator thus occurs at $f_r = 1/\left(2\pi\sqrt{L_r C_r}\right)$.

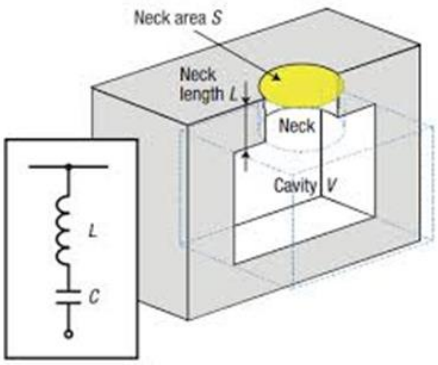

Figure 3.1 Helmholtz resonator with equivalent circuit. (From [27])

Helmholtz resonator does not use typical standing waves to create a resonance, and the dimension of each element can be made much smaller than the wavelength. From that it follows that the Helmholtz resonator can be modeled as a homogenized medium, and described with frequency dependent effective modulus, which is a reciprocal value of the compressibility and is equal to [27]:

$$E_{eff}^{-1}(\omega) = E_0^{-1}\left[1 - \frac{F\omega_0^2}{\omega^2 - \omega_0^2 + i\Gamma\omega}\right], \tag{3.3}$$

where F is a geometrical factor, $\omega_0 \approx c\sqrt{S/lV}$ is a resonant frequency and Γ is the dissipation loss in the resonating Helmholtz elements. Calculated effective modulus using Eq. (3.3) is shown in Fig. 3.2.

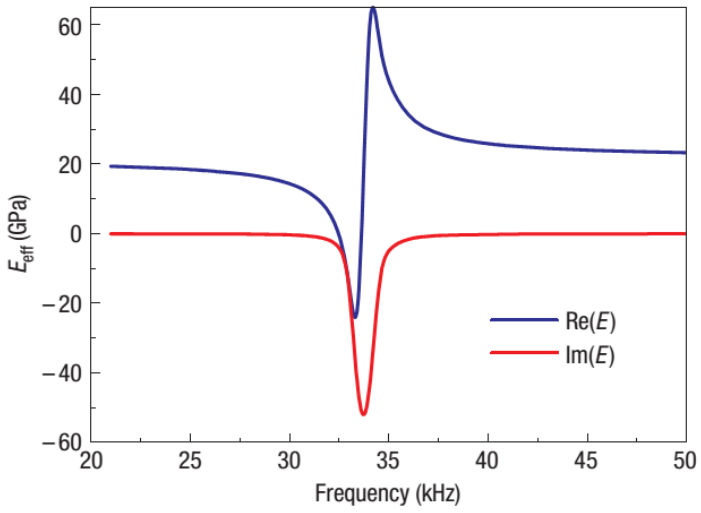

Figure 3.2 Calculated effective bulk modulus in the above one-dimensional subwavelength Helmholtz resonators. (From [27])

This frequency-dependent response is essential to the negative modulus over a range of frequencies. At frequencies near resonance, the induced displacement in the neck becomes very large, as is typical in resonance phenomena. The large response represents accumulation of energy over many cycles, such that a considerable amount of energy is stored in the resonator relative to the driving field. This stored energy is significant to maintain the sequence of displacement near resonance even when the excitation field changes the sign. That is, as the frequency of the driving pressure field is swept through the resonance, the instantaneous displacement of the mass center in the

unit cell flips from in-phase to out-of-phase with the driving field, and the material shows a negative response [27]. If a conventional hollow duct with an otherwise allpass frequency response is loaded with an array of the Helmholtz resonators, a notch in the frequency response at the resonant frequency can be observed. Such a transmission characteristic is shown in Fig. 3.3.

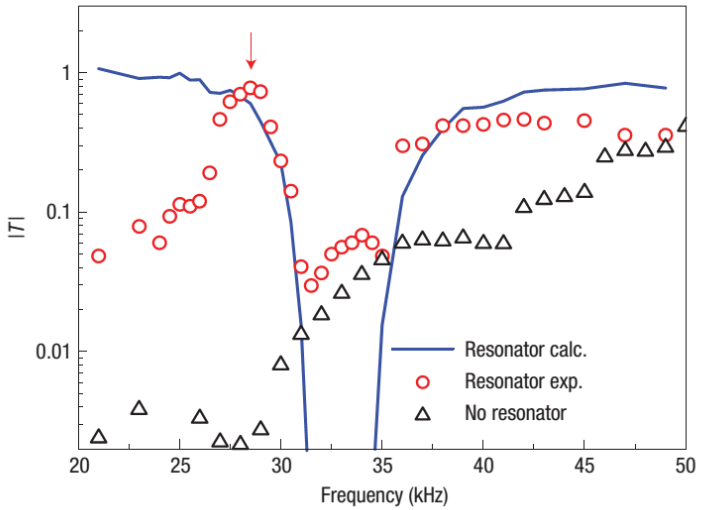

Figure 3.3 Transmission characteristic of the hollow duct loaded array of Helmholtz resonators. (From [27])

From Fig 3.3 it can be seen that around the resonance the value of bulk modulus is negative, the propagation does not exist and a stop band emerges. Negative bulk modulus has a similar effect on acoustic wave propagation as the negative permeability for electromagnetic wave propagation – both cause the waves to be evanescent in character.

3.2.2 Metamaterials based on sonic crystals

For two-component composite materials, the effective mass density is usually given by the volume-averaged value. An implicit assumption underlying the validity of the static mass density expression is that in the presence of wave motion, the two components of the composite move in unison [68]. For a composite which consist of a many identical local resonators (spring mass systems) embedded in a matrix material, at the resonant frequency the local resonators' masses move out of phase with the matrix displacement and we have a case in which the matrix and the resonators' masses display relative motion [68]. If the local resonators occupy a significant volume fraction, then within a particular frequency range the overall effective mass density can appear to be negative [29-31]. This is simply illustrated in a one-dimensional (1D) model [32], where cylindrical cavities of length *d* are embedded in a bar of rigid material. Within each cavity, a massive sphere is attached to the cavity wall by two identical springs. Figure 3.4a shows a cross-sectional image of the basic unit for a 3D locally resonant sonic material [29]. It consists of a metallic sphere of 5 mm in radius coated by a layer of silicone rubber. Figure 3.4b shows a cube assembled from basic units with epoxy, in a simple cubic structure with a lattice constant of 1.55 cm [29].

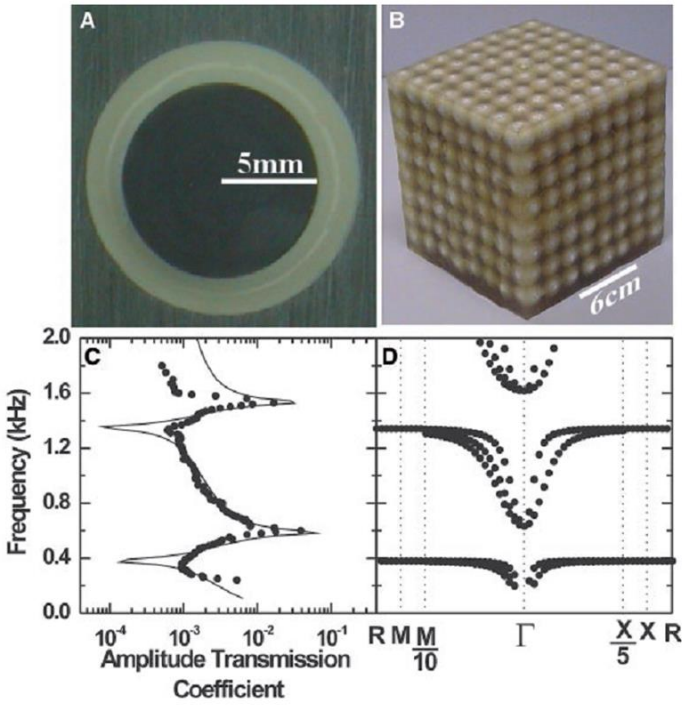

Figure 3.4 a) Local resonator unit, b) 8x8x8 matrix of unit cells, c) Transmission characteristic of the structure, d) band structure of the crystal. (From [29])

The metallic sphere of the basic unit acts as a heavy mass, with silicone rubber as a weak spring. Hence there must be a low-frequency resonance. Moreover, the resonance is local in character, to be distinguished from the structural resonances that are common to any mechanical object. Figures 3.4c and 3.4d shown the transmission characteristics and band structure of the crystal shown in Fig. 3.4b. A transmission dip can be observed at 380 Hz, followed by a transmission maximum at 610 Hz. This pattern is repeated at 1,340 Hz and 1,580 Hz. The solid line is the calculated transmission, and the solid circles are the measured data [29]. The calculated and measured data show a good agreement. In Fig. 3.4d, the calculated band structure is shown. The flat band edges, at 380 Hz and 1,340 Hz, are characteristic of local (anti-)resonances that are very weakly coupled to each other. It is seen that the structure shown in Fig. 3.4b has a complete bandgap between 380 Hz and 610 Hz. In contrast to phononic crystals, where the relevant wavelength corresponding to the primary bandgap frequency must be comparable to the lattice constant, here the wavelength (in epoxy) at 380 Hz is ~300 times the lattice constant [29]. The wavelength is much smaller than the lattice constant and the composite material can be homogenized and described by the effective density. However, close to the resonances, the large dispersion of the response function means that the effective wavelength is much smaller and becomes comparable to the lattice constant, hence the strong scattering. This peculiar material can break the so-called “mass density law” of sound transmission [29]. It should be noted that an attenuation gap can be due either to negative elastic constant or to negative dynamic mass density. In [29], the effect was wrongly attributed to negative elastic constant, but this has been

corrected in [30-31]. Calculated dynamic mass density D_{eff} for one unit cell of the locally resonant sonic material is shown in Fig. 3.5. Around 370 and 1,340 Hz, i.e., the transmission dip frequencies, the dynamic mass density clearly displays a resonance-like behavior [68].

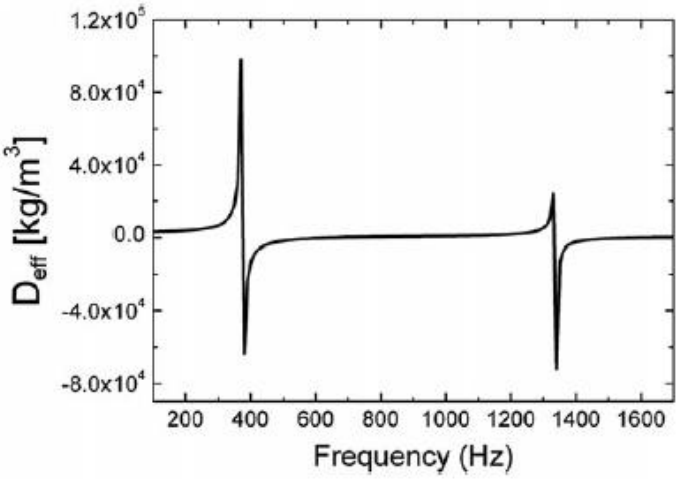

Figure 3.5 Effective mass density for a sonic crystal. (From [68])

The effective density has a resonant behavior and has a negative value where the transmission dips in the transmission characteristic. In this frequency region the wave propagation is not possible.

3.3 Acoustic CRLH (composite right/left handed) transmission line

Another approach to design metamaterials is using the transmission line concept. A short section of conventional (right handed) transmission line can be modeled with series acoustic inductance and shunt acoustic compliance. The left handed transmission line is an opposite of conventional transmission line and can be modeled with series compliance and shunt acoustic inductance. A clear left-handed transmission line does not exist, i.e. there is always a right handed component too. This type of structure is called composite right/left-handed transmission line (CRLH TL). The equivalent circuit for a short section of acoustic CRLH transmission line is shown in Fig. 3.6.

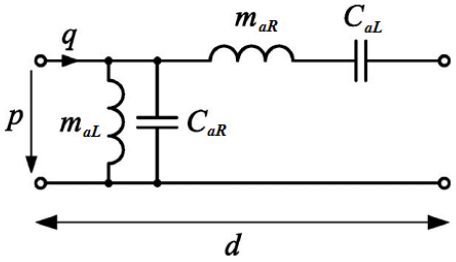

Figure 3.6 Equivalent circuit of short section acoustic CRLH transmission line. (From [63])

Acoustic impedance is defined as the ratio between acoustic pressure and the volumetric flow, the acoustic admittance is a reciprocal value of acoustic impedance. In that case acoustic impedance (Z_a') and acoustic admittance (Y_a') for an acoustic CRLH transmission line can be defined similarly to admittance and impedance for an electrical transmission line [24-25]:

$$Z'_a(\omega) = j\left(\omega m'_{aR} - \frac{1}{\omega C'_{aL}}\right), \tag{3.4}$$

$$Y'_a(\omega) = j\left(\omega C'_{aR} - \frac{1}{\omega m'_{aL}}\right), \tag{3.5}$$

where:

$$\begin{aligned} m'_{aR} &= \frac{m_{aR}}{d}, \\ m'_{aL} &= \frac{m_{aL}}{d}, \\ C'_{aR} &= \frac{C_{aR}}{d}, \\ C'_{aL} &= \frac{C_{aL}}{d}, \end{aligned} \tag{3.6}$$

are per unit length values for a series and shunt acoustic inductance and acoustic compliance. If d is small enough, the system can be described as was done in the case of electromagnetic CRLH transmission lines [24-25]. In that case the structure can be seen as a homogenous medium. Effective properties of the medium are specified with impedance and admittance of the small section of acoustic CRLH. The acoustic wave impedance for an arbitrary fluid medium is defined as:

$$\eta_a = \sqrt{\frac{\rho}{\beta}}, \tag{3.7}$$

If a transmission line is considered as a homogenous medium, wave impedance can be seen as equal to characteristic impedance. In acoustics it has to be divided with the cross section area, because in the wave equations are related to pressure and particle velocity, while in the acoustic circuit theory instead of particle velocity, volumetric velocity equal to $q = Sv$ is used. Hence:

$$Z_0 = \sqrt{\frac{Z'_a}{Y'_a}} = \sqrt{\frac{\rho}{\beta}}\frac{1}{S}, \tag{3.8}$$

Using the same principle the wavenumber is given as:

$$k'' = -j\sqrt{Z'_a Y'_a} = \omega\sqrt{\rho\beta}. \tag{3.9}$$

From Eqs. (3.4), (3.5), (3.8), (3.9) effective material parameters can be defined as functions of inductance and admittance of the transmission line:

$$\rho_{eff} = \frac{Z'_a(\omega)}{j\omega}S = \left(m'_{aR} - \frac{1}{\omega^2 C'_{aL}}\right)S, \tag{3.10}$$

$$\beta_{eff} = \frac{Y'_a(\omega)}{j\omega}\frac{1}{S} = \left(C'_{aR} - \frac{1}{\omega^2 m'_{aL}}\right)\frac{1}{S}. \tag{3.11}$$

From Eqs. (3.10) and (3.11) two resonant frequencies ω_1 i ω_2 can be determined and it can be seen that the effective density is less than zero below the frequency ω_1, and the bulk modulus (compressibility) B_{eff} is negative below the frequency ω_2:

$$\omega_1 = \frac{1}{\sqrt{m'_{aR} C'_{aL}}} \tag{3.12}$$

$$\omega_2 = \frac{1}{\sqrt{m'_{aL} C'_{aR}}} \tag{3.13}$$

In the frequency range where both parameters are negative the wavenumber has a real but negative value, the wave propagation is possible, and the structure is a double negative medium. In a frequency range where just one of the parameters is less than zero the wavenumber is imaginary and the wave propagation is not possible except for evanescent modes, i.e. the medium is a single negative medium. Clearly, in the frequency range where both parameters are larger than zero, the wave propagation exists and it is right-handed propagation with a positive real wavenumber.

3.3.1 Side holes

To realize the acoustic CRLH transmission line, shunt inductance and series capacitance sections should be included into in a conventional transmission line. One way to implement shunt inductance in the system is using a simple tube as a conventional host with drilled side holes [37], as shown in Fig 3.7.

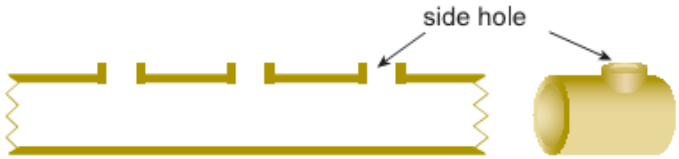

Figure 3.7 Hollow tubes with drilled side holes. (From [37])

In this structure the unit cell is not of resonant type. This structure has a negative compressibility (reciprocal value of bulk modulus), below the cut-off frequency. Acoustic wave propagation exists if the operating frequency is larger than cut-off frequency. This shape of effective compressibility is a Drude-like response, and like in noble metals, it has negative dielectric permittivity below plasma frequency [17]. Longitudinal mechanical waves (sound) propagate in the tube which is filled with air, which, fluctuating at the ends of the side holes changes the characteristics of the wave propagation. Air column above all these side holes have a mass given by $M = \rho l' S$ where ρ= 1.21 kgm^{-3} is the mass density of the air, l' is the effective length of the side hole and S is the cross section area of the hole. The distance between two side holes (d) is much smaller the guided wavelength and the medium can be seen like a homogeneous medium with effective material parameters. Using the second Newton's law for the structure and using a harmonic velocity source the effective compressibility can be derived as [37]:

$$\beta_{eff} = \beta \left(1 - \frac{\omega_{SH}^2}{\omega(\omega + i\gamma)}\right) \tag{3.14}$$

where γ is the damping term representing the sum of all the dissipating mechanisms for the propagating wave and ω_{SH} is the cut-off frequency, defined as:

$$\omega_{SH} = \sqrt{\frac{\sigma_{SH}^2}{\beta A \rho_{SH}}} \tag{3.15}$$

where β is the adiabatic compressibility of the air ($7.04 \cdot 10^{-6}$ Pa^{-1}), ρ_{SH} is side hole mass density and σ_{SH} is side hole area density, and $\rho_{SH} = nM$ and $\sigma_{SH} = nS$ where $n = 1/d$ (side holes per unit length). Phase velocity in the tube is:

$$v_{ph} = \sqrt{\frac{1}{\rho \beta_{eff}}} = \frac{v_0}{\sqrt{\left(1 - \omega_{SH}^2/\omega(\omega + i\gamma)\right)}} \tag{3.16}$$

Wave number can be calculated from the Eq. (3.16) and can be written as:

$$k(\omega) = \frac{\omega}{v_{ph}} = \frac{\sqrt{\omega^2 - \omega_{SH}^2/(1 + i\gamma/\omega)}}{v_0} \tag{3.17}$$

From Eq. (3.17) it can be obtained that when the operating frequency above the cut-off frequency the wavenumber is a purely imaginary number and the propagation does not exist. In the other case, when the frequency is larger than the cut-off frequency, the wave number is real and in that case the wave propagation is possible. Calculated transmission function for the lossless and the lossy case, together with experimental results of the metamaterial from [37], is shown in Fig. 3.8.

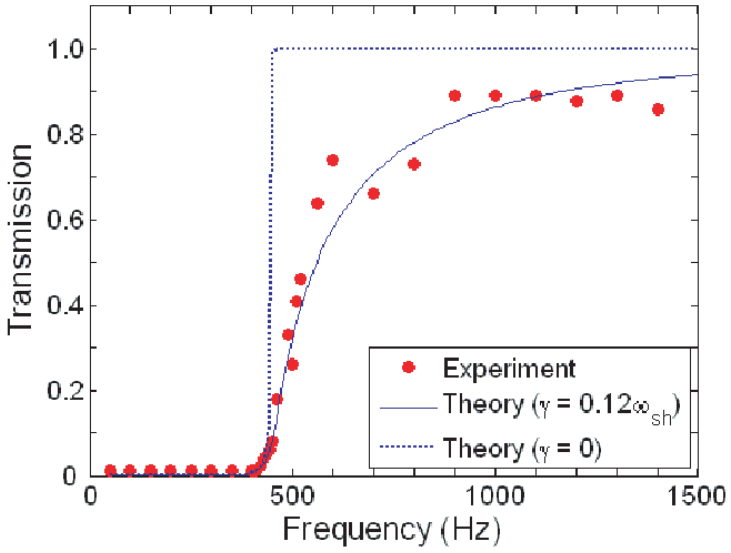

Figure 3.8 Normalized transmission characteristic simulation results in the lossless and lossy case, and experimental results. (From [37])

Below cut-off frequency there is no transmission, and above it there is. This type of structure is a metamaterial unit cell with negative effective compressibility. The effective compressibility has a Drude-like shape, it is negative below the cut-off frequency and positive after it.

3.3.2 Acoustic metamaterial with negative mass density (ρ)

For implementation of a series capacitance in the conventional acoustic transmission line a mechanical element (membrane) has to be used. The unit cell consists of a membrane which is placed in the tube [39], as shown in Fig. 3.9. The length of the unit cell is much smaller than the wavelength at the operating frequency. These types of unit cells produce negative effective mass density in a wide frequency range. The effective density shape follows the Drude model.

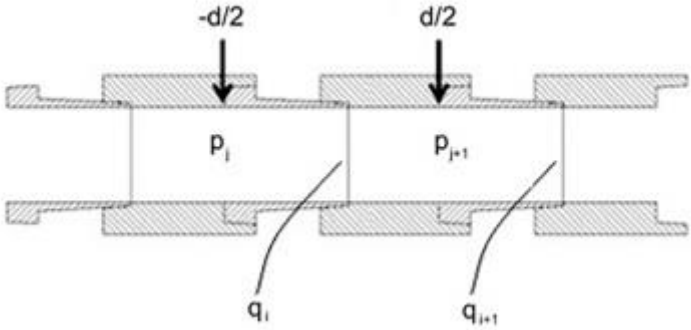

Figure 3.9 Hollow tube loaded with membranes. (From [39])

One-dimensional acoustic wave can be described by a one-dimensional acoustic wave equation, which includes pressure in tube p and longitudinal displacement q, which depend from time t and from the position in the one-dimensional tube z. If the j^{th} unit cell consists of the j^{th} membrane and a section of a hollow tube of length d, as in the Fig 3.9, the length of the unit cell is much smaller than the wavelength and a can be considered that the average longitudinal displacement in air inside the j^{th} unit cell and displacement of the membrane are both equal to the value q_j. In the case when the excitation is harmonic, from the one-dimensional equation of the dynamic equilibrium the effective mass density can be derived as [39]:

$$\rho_{eff} = \rho' - \frac{8\pi\tau}{\omega^2 A d} = \rho'\left(1 - \frac{\omega_c^2}{\omega^2}\right) \tag{3.18}$$

where A is the cross section area, d is the period of the unit cells, τ is the membrane tension and ρ' is defined as:

$$\rho' = \rho\left(1 + \frac{M}{\rho A d}\right) \tag{3.19}$$

where M is the mass of the membrane, while ω_c is the cut-off frequency, which can be calculated as:

$$\omega_c = \sqrt{\frac{8\pi\tau}{\rho A d + M}} \tag{3.20}$$

Phase velocity of the acoustic wave in the medium can be shown to be equal to:

$$v_{ph} = \sqrt{\frac{1}{\rho_{eff}\beta}} = \sqrt{\frac{1}{\beta\rho'\left(1 - \frac{\omega_c^2}{\omega^2}\right)}} \tag{3.21}$$

where β is the compressibility of the air. From the phase velocity the acoustic wavenumber can be calculated and it is:

$$k(\omega) = \sqrt{\beta\rho'(\omega^2 - \omega_c^2)} \tag{3.22}$$

From Eq.(3.22) it can be observed that, when the frequency is below the cut-off frequency, the wavenumber has an imaginary value, which means that the acoustic wave propagation does not exist in that frequency range, and that only evanescent modes propagate. Figure 3.10 shows the measured transfer function of this type of metamaterial from [39].

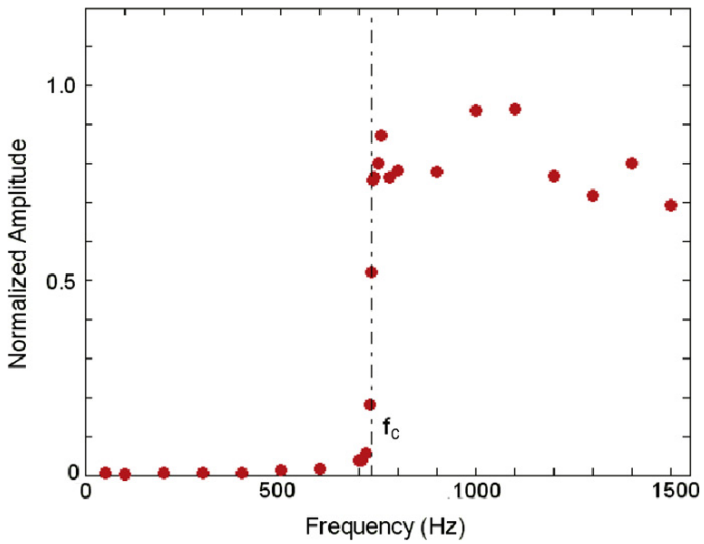

Figure 3.10 Normalized transfer function (From [39])

From Fig 3.10 it can be seen that below the cut-off frequency the transmission does not exist, above ω_c the structure behaves like a conventional tube and transmits the all energy. A conventional air duct loaded with membranes where the distances between the membranes are much smaller than the guided wavelength is thus a metamaterial unit cell with negative mass density in a wide frequency range (Drude-like model).

3.3.3 Realization of the acoustic CRLH transmission line

By composing two structures which were previously described we can realize an acoustic composite right-left handed transmission line (CRLH) [61]. Figure 3.11 shows the two previously described structures with negative mass density and compressibility respectively, and the composite double negative metamaterial.

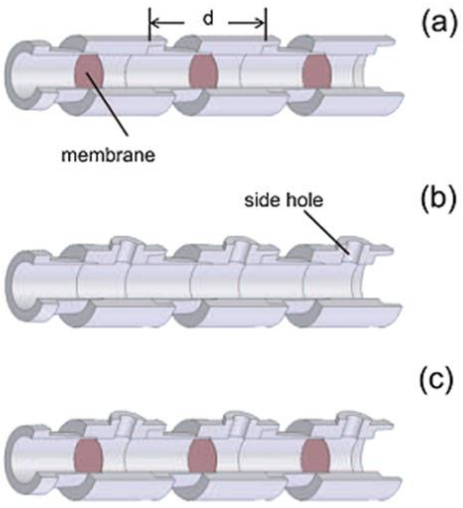

Figure 3.11 Acoustic metamaterials a) Metamaterial with negative effective mass density, b) Metamaterial with negative effective compressibility, c) Double-negative metamaterial. (From [61])

Effective mass density for a structure a) is defined with Eq. (3.18). Effective compressibility for the structure b) is defined with Eq. (3.14). Transfer functions for these two structures which are shown in the Figs. 3.8 and 3.10 now are together shown in the Fig 3.12a with both cut-off frequencies. Cut-off frequency for a structure a) is larger than the cut-off frequency for structure b). Composite structure which is a combination of the structures a) and b) is shown in Fig. 3.11c), and it inherits properties from both structures a) and b). It means that effective mass density and compressibility for the structure c) are given by Eqs. (3.14) and (3.18). For the structure c), effective compressibility is less than zero if the frequency is less than ω_{SH} (from eq. 3.14), and effective mass density is less than zero if the frequency is less than $\omega_{c.}$ The transmission characteristic of the composite structure is shown in Fig. 3.12b.

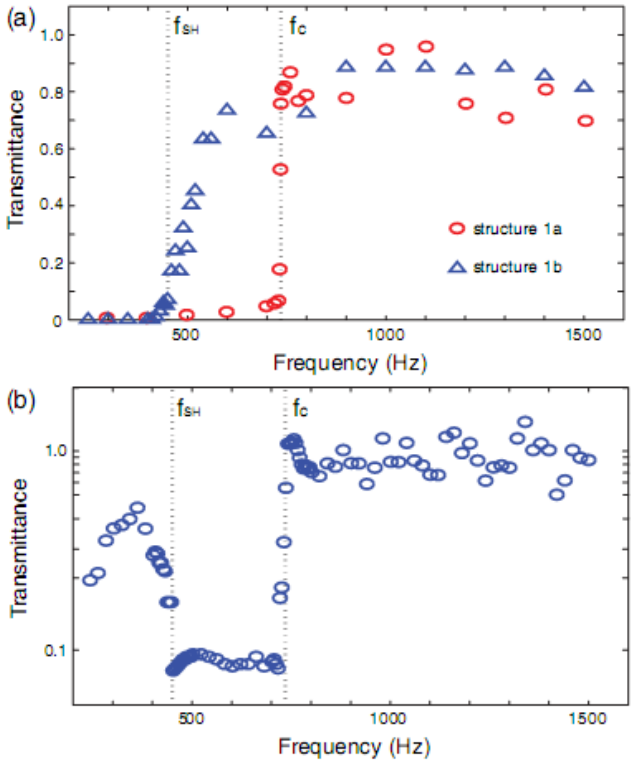

Figure 3.12 Transmission function, a) Structure a) i b) from Fig. 3.11, b) Structure c) from Fig. 3.11 (From [61])

From Fig. 3.12b it can be seen that the transmission does not exist just between two cut-off frequencies, where compressibility and density have opposite signs. Phase velocity for a structure c) can be derived as:

$$v_{ph} = \sqrt{\frac{1}{\beta_{eff}\rho_{eff}}} = \sqrt{\frac{1}{\beta\rho}}\left(\sqrt{1-\frac{\omega_{SH}^2}{\omega^2}}\sqrt{1-\frac{\omega_c^2}{\omega^2}}\right) \tag{3.23}$$

while the wavenumber can be derived as:

$$k(\omega) = \omega\sqrt{\rho\beta}\sqrt{1-\frac{\omega_{SH}^2}{\omega^2}}\sqrt{1-\frac{\omega_c^2}{\omega^2}} \tag{3.24}$$

From Eq. (3.24) wavenumber for a metamaterial between frequencies $0<\omega<\omega_{SH}$ is real and less than zero, because effective values of both material parameters (compressibility and mass density) are less than zero in the same frequency range. In this frequency range metamaterial behaves as a double negative material and can be characterized by antiparallel phase and group velocities. In frequency range $\omega_{SH}<\omega<\omega_c$ (between the cut-off frequencies), just one of the parameters is less than zero namely the mass density. In this case wavenumber is imaginary and only evanescent propagation exists. Above the second cut-off frequency both parameters are positive and the wave propagation is conventional.

4. Analysis of acoustic metamaterials

This chapter will describe characterization methods, parameters and simulation models which were used during the research. Based on electro-acoustic analogy we redefined and used parameters and techniques which are commonly used in electrical and microwave engineering, such as transmission line theory, two-port network parameters, circuit parameter transformations, effective medium theory etc.

4.1 Acoustic scattering parameters and extracting an acoustic S-matrix

Linear time-invariant two-port networks can be characterized by a number of equivalent circuit parameter sets, such as transfer matrix, impedance matrix, admittance matrix, and scattering matrix [69]. In this work we opted for the scattering matrix approach, as it is the basis of most methods for the analysis of electromagnetic metamaterials [70, 71] and it allows us to use the same methods in the analysis of acoustic metamaterials as well. Let us consider a slab of unknown acoustic medium with acoustic impedance Z_x and transmission coefficient γ inserted into a long acoustic duct filled with air, the acoustic impedance of which is Z_0, as shown in Fig. 4.1.

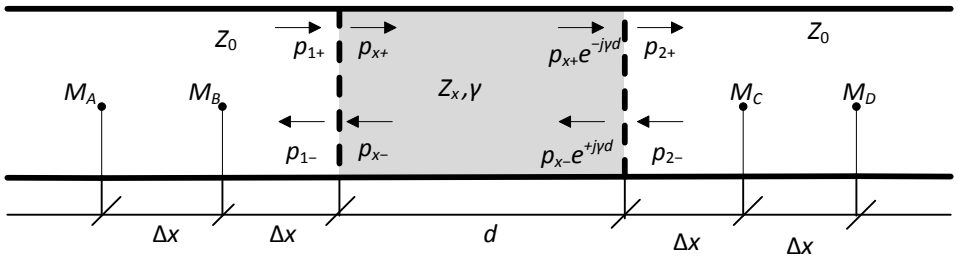

Figure 4.1 Extraction of complex acoustic S-parameters

Under the assumption that the structure allows the propagation of plane waves only, the definition of acoustic scattering parameters, by analogy with their definition in electromagnetics [69], is the following:

$$\begin{bmatrix} p_{1-} \\ p_{2+} \end{bmatrix} = \begin{bmatrix} S_{11} & S_{12} \\ S_{21} & S_{22} \end{bmatrix} \begin{bmatrix} p_{1+} \\ p_{2-} \end{bmatrix} \tag{4.1}$$

where p_{1+} and p_{1-} denote the phasors of transmitted and reflected acoustic waves in air at the left boundary between air and the unknown medium (port 1), and p_{2+} and p_{2-} denote the phasors of transmitted and reflected acoustic waves in air at the right boundary between the unknown medium and air (port 2). The acoustic scattering parameters describe the same physical properties as the electrical scattering parameters. S_{11} and S_{22} are the reflection parameters related to port 1 and port 2 respectively. S_{21} and S_{12} describe the transmission between port 1 to port 2 and vice versa.

As we are able to measure only the sum of the transmitted and the reflected wave at a certain point, the problem of calculating S-parameters amounts to the separation of measured values into their corresponding transmitted and reflected components. We measure acoustic pressure at 4 points, using

4 microphones located as shown in Fig. 4.1. For the sake of simplicity, the four distances (M_A to M_B, M_B to port 1, port 2 to M_C and M_C to M_D) are set to be identical and equal to Δx. The total pressures measured by the 4 microphones are given by Eq. (4.2):

$$\begin{aligned} p_A &= p_{1+}e^{jk_0 2\Delta x} + p_{1-}e^{-jk_0 2\Delta x}\ , \\ p_B &= p_{1+}e^{jk_0 \Delta x} + p_{1-}e^{-jk_0 \Delta x}\ , \\ p_C &= p_{2+}e^{-jk_0 \Delta x} + p_{2-}e^{jk_0 \Delta x}\ , \\ p_D &= p_{2+}e^{-jk_0 2\Delta x} + p_{2-}e^{jk_0 2\Delta x}\ , \end{aligned} \tag{4.2}$$

where $k_0 = \omega/c$ is the wave number in the air. Given this set of 4 equations with 4 unknowns, we can compute the transmitted and reflected components of pressuresp_{1+}, p_{2+}, p_{1-} and p_{2-}. In a general case this would have been insufficient to calculate the S-parameters, and it would have been necessary to perform two sets of measurements, one with the source on the left side and one with the source on the right side, resulting in a readily soluble system of 12 equations with 12 unknowns (p_{1+}^L, p_{2+}^L, p_{1-}^L, p_{2-}^L, p_{1+}^R, p_{2+}^R, p_{1-}^R, p_{2-}^R and the 4 S-parameters). However, under the assumption that the slab of unknown medium constitutes a symmetrical and reciprocal system, one set of measurements is sufficient, as $S_{11} = S_{22}$ and $S_{12} = S_{21}$ and the unknown 2 values of the complex S-parameters can be easily found from the matrix Eq. (4.1). The code for extraction and calculation of the acoustic scattering matrix was written in *Matlab* and is given in *Appendix A1*.

4.2. Extraction of complex effective material parameters

Effective material parameters of the acoustic metamaterials can be extracted from the scattering matrix using a method similar to the one used in the case of electromagnetic metamaterials, [70, 71]. Acoustic wave impedance Z_{eff} and acoustic refractive index N_{eff} are calculated directly from the S-matrix by adjusting formulas according to electro-acoustical analogies.

The extraction is based on the effective medium theory; the inhomogeneous structure (metamaterial unit cell) is replaced with equivalent duct with effective material parameters. Reflection coefficient Γ for a wave is given by:

$$\Gamma = \frac{Z_{eff} - Z^{TL}}{Z_{eff} + Z^{TL}}\ . \tag{4.3}$$

The two-port scattering parameters can be determined as a function of the reflection coefficient and the propagation factor $\tau = e^{\gamma L}$, where L is the length of the structure and γ is the complex propagation constant: [72].

$$\begin{aligned} S_{11} &= \frac{\Gamma(1-\tau^2)}{1-\Gamma^2\tau^2}\ , \\ S_{11} &= \frac{\tau(1-\Gamma^2)}{1-\Gamma^2\tau^2}\ . \end{aligned} \tag{4.4}$$

By solving Eq. (4.4) using the Nicolson-Ross-Weir (NRW) approach [73, 74], we can obtain the expression for Γ:

$$\Gamma = \chi \pm \sqrt{\chi^2 - 1}\,, \tag{4.5}$$

where the sign (±) is determined by $|\Gamma| \leq 1$ and:

$$\chi = \frac{S_{11}^2 - S_{21}^2 + 1}{2S_{11}}. \tag{4.6}$$

Hence, Z_{eff} can be obtained from Eq. (4.3):

$$Z_{eff} = \left(\frac{1+\Gamma}{1-\Gamma}\right) Z^{TL}\,, \tag{4.7}$$

where Z^{TL} can generally be calculated using Eq. (2.44). The reflection coefficient Γ can be calculated from the scattering parameters using Eqs. (4.5) and (4.6). With this method we can extract the effective impedance of the metamaterial unit cell from the acoustic S matrix.

The complex acoustic refractive index can be written in the following form:

$$N_{eff} = n_{\,eff} + i\kappa_{eff}\,. \tag{4.8}$$

where the real part n_{eff} is the acoustic refractive index and the imaginary part κ_{eff} is extinction coefficient, which indicates the amount of absorption losses. The value of the imaginary part κ_{eff} has to be positive because one part of the acoustic wave is absorbed in the material. In electromagnetics and in transmission line theory it is well known how the refractive index can be calculated from the scattering parameters [75]. Using electroacoustic analogy the equation in acoustic case can be written in the similar form, as:

$$e^{iN_{eff}k_0L_{eff}} = \frac{S_{21}}{1-S_{11}R_{01}}\,, \tag{4.9}$$

where k_0 is the wavenumber in the surrounding medium (air), L_{eff} is the length of the structure, S_{11} and S_{21} are the scattering parameters calculated using the method from the previous section and R_{01} is defined as:

$$R_{01} = \frac{Z_{eff}-1}{Z_{eff}+1}\,, \tag{4.10}$$

where Z_{eff} is the effective wave impedance of the medium calculated from Eq. (4.7). From (4.9) the refractive index is:

$$N_{eff} = \frac{1}{k_0L_{eff}}\left\{\mathrm{Im}\left[\ln\left(e^{iN_{eff}k_0L_{eff}}\right)\right] + 2m\pi - i\mathrm{Re}\left[\ln\left(e^{iN_{eff}k_0L_{eff}}\right)\right]\right\}. \tag{4.11}$$

The real and the imaginary part of the acoustic refractive index are, respectively:

$$n_{eff} = \frac{\mathrm{Im}\left[\ln\left(e^{iN_{eff}k_0L_{eff}}\right)\right]}{k_0L_{eff}} + \frac{2m\pi}{k_0L_{eff}} = n_{eff}^0 + \frac{2m\pi}{k_0L_{eff}}\,, \tag{4.12}$$

$$\kappa_{eff} = \frac{-\mathrm{Re}\left[\ln\left(e^{iN_{eff}k_0L_{eff}}\right)\right]}{k_0L_{eff}}\,, \tag{4.13}$$

where n_{eff}^0 is the acoustic refractive index corresponding to the principal branch of the complex logarithmic function and m is an integer [71]. The imaginary part of the refractive index is not affected by the branching problem. The imaginary part of the acoustic refractive index is also always positive, implying that the function is analytical (causality). Using the Kramers-Kronig relations we

can determine the real part of the acoustic refractive index from the imaginary part. The retrieved acoustic refractive index is calculated by the Kramers-Kronig relations as:

$$n^{KK}(\omega') = 1 + \frac{2}{\pi}\wp\int_0^{\infty}\frac{\omega\kappa_{eff}(\omega)}{\omega^2-\omega'^2}d\omega\ . \tag{4.14}$$

Where $\wp$ denotes the principal value of the improper integral [76]. Substituting the refractive index predicted by the Kramers-Kronig relation in Eq. (4.12), the branch number can be expressed as Eq. (4.15) where the function Round() rounds the argument towards the nearest integer: [71]

$$m = \text{Round}\left[\left(n^{KK} - n_{eff}^{0}\right)\frac{k_0 L_{eff}}{2\pi}\right]. \tag{4.15}$$

The acoustic refractive index is calculated so that we select the branch that is closest to the value predicted by the Kramers–Kronig relation. The branch number is substituted in Eq. (4.11), and the exact value of the acoustic refractive index is calculated. The algorithm then checks the continuity of the refractive index [71]. The acoustic refractive index and the acoustic wave impedance can be written as functions of the effective material parameters (mass density and compressibility):

$$N_{eff} = \sqrt{\rho_{eff}\beta_{eff}}\ , \tag{4.16}$$

$$Z_{eff} = \sqrt{\frac{\rho_{eff}}{\beta_{eff}}}\ . \tag{4.17}$$

Effective material parameters, namely the compressibility (β_{eff}) and density (ρ_{eff}), are analogous to the permittivity (ε_{eff}) and permeability (μ_{eff}), respectively, and can be calculated as: [77, 78]

$$\beta_{eff} = \frac{N_{eff}}{Z_{eff}}\ , \tag{4.18}$$

$$\rho_{eff} = N_{eff}Z_{eff}\ . \tag{4.19}$$

The *Matlab* code for the extraction of acoustic circuit parameters is given in the *Appendix A2.*

4.3 Simulation models of acoustic metamaterials

All structures were designed, modeled and simulated with two different numerical simulation models. The first one is a finite element method (FEM) simulation model, designed in the *COMSOL Multiphysics* simulator, and the second one, based on the transmission line model and the circuit theory (ABCD matrix, two-port network matrix transformations etc.), was designed in *Matlab*.

4.3.1 Finite element method (FEM) simulation model in *COMSOL Multiphysics*

COMSOL Multiphysics is a finite element analysis, solver and simulation software. *COMSOL* is a multiphysical simulator consisting of different physical modules which can be used separately or combined in order to analyze different physical phenomena together [79]. The different modules cover all topics of physics, from structural mechanics to chemical reactions. In this research we used the Acoustic module to model acoustic wave propagation in air [80], Structural Mechanics Module to model mechanical components in membrane type metamaterials [81] and the Heat transfer module to introduce temperature variation and analyze its effects on surface acoustic wave propagation [82].

All *COMSOL* modules are capable of defining models for structures in one, two or three dimensions as well as one- or two-dimensional axisymmetric structure models, the latter exploiting the axial symmetry to simplify the calculation process and decrease computational time. In this research 2D, 2D axisymmetric and 3D modules were used. In the Acoustic module port boundaries such as ones in Microwave module or in other electromagnetic wave simulators (*CST, HFSS* etc.) are not achievable. For that reason microphones (probes) capable of measuring acoustic S-parameters following the theory described in *Section 4.1* had to be made manually. Four boundary probes were placed into the system. The locations of the microphones and the distance between them were determined following the instructions from *Section 4.1*. Probes measured the average acoustic pressure defined by Eq. (4.20) on a specified surface where P_i is the pressure phasor, S_i is the area of the boundary probe, p is the acoustic pressure and the integer *i* in the subscript denotes the location:

$$P_i = \frac{1}{S_i}\int_{S_i} p dS_i \, . \tag{4.20}$$

Received pressure phasors on a specified location and on a specified frequency are suitable for the calculation of S-parameters and determination of spectral transmission and reflection characteristics of the analyzed structures.

Defining materials and their properties is a very important part of model design. In *COMSOL Multyphysics* a material library with specifications of properties of materials is available. In the Acoustic module the most important parameters are the density and the speed of sound in a material. Of course in a lossy case and temperature dependent simulations other important properties include viscosity, temperature and the specific gas constant when the medium is modeled as an ideal gas. The mechanical components (membranes, frames) which could constitute a part of a metamaterial structure are modeled by a special type of material model, so called linear elastic material model. Linear elastic material model is characterized with its density, Young's modulus and Poisson's coefficient, which is manually added to the model. Three more boundary conditions were used in every designed model. The Plane Wave Radiation Boundary was used as an acoustic source in systems with specified amplitude, phase and frequency. The Sound Hard Boundary, which is the acoustical counterpart of PEC (perfect electrical conductor) in electromagnetic simulations, was used to surround the structure, and with this type of wall we modelled closed structures (pipe walls, boxes etc. In cases when we used this boundary the vibrations in the hollow tubes and pipes were neglected. Perfectly Matched Layer (PML) boundary was used to model the open sections (open boxes, ends of tubes etc.). This type of boundary is a perfect absorber and there is no reflection when an acoustic wave interacts with it.

4.3.2 Transmission line model based on ABCD matrix

Transmission line model is based on concepts described in *Chapter 2*. Namely, every "acoustically short" section can be modeled with series impedance and shunt admittance, as shown in Fig. 4.2.

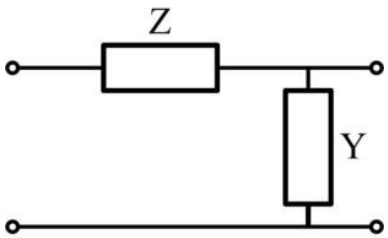

Figure 4.2 Transmission line model of a short section of an acoustic duct

A conventional transmission line can be modeled with series inductance and resistance (losses) and with shunt acoustic compliance and conductance. The left-handed transmission line is the opposite of the conventional one, in that the acoustic compliance is connected in series and the inductance in shunt. All circuit parameters depend from geometrical parameters and the properties of the fluid with which the tube is filled.

In all case in this research the fluid medium is air. Air's viscosity and heat conductivity are small enough and can be neglected. However, when the diameter of the pipe or the acoustic waveguide is too small the losses increase. This phenomenon is the so called "narrow pipe" effect, which was firstly described by Kirchhoff in 1868 [83]. This type of losses can be modeled by simply using the lossless model and adding losses as described in [84-87]. The series impedance and the shunt admittance in the lossy case can be described by Eqs. (4.21-4.22):

$$Z = j\left(\frac{\omega\rho_0}{\pi a^2}\right)(1 - F_v)^{-1}\,, \tag{4.21}$$

$$Y = j\left(\frac{\omega\pi a^2}{\rho_0 c^2}\right)(1 + (\gamma - 1)F_t)\,, \tag{4.22}$$

where a is the tube radius, ω is the angular frequency, ρ_0 is the density of the fluid (air), and c the sound velocity in the air.F_v and F_t are defined as:

$$F_v = \frac{2}{r_v\sqrt{-j}}\frac{\mathrm{J}_1(r_v\sqrt{-j})}{\mathrm{J}_0(r_v\sqrt{-j})}\,, \tag{4.23}$$

$$F_t = \frac{2}{r_t\sqrt{-j}}\frac{\mathrm{J}_1(r_t\sqrt{-j})}{\mathrm{J}_0(r_t\sqrt{-j})}\,, \tag{4.24}$$

where J_m is the Bessel function of the first kind, order m. Parameters r_v and r_t are defined as:

$$r_v = a\sqrt{\frac{\rho\omega}{\mu}}\,, \tag{4.25}$$

$$r_t = r_v\sqrt{\frac{\mu C_P}{\lambda}} = \sigma r_v\,, \tag{4.26}$$

where C_p is specific heat capacity at constant pressure, λ is heat conductivity, μ is the shear viscosity and σ is the square root of the Prandtl number. From series impedance and shunt admittance the characteristic impedance and the propagation constant can be calculated as:

$$Z_0 = \sqrt{\frac{Z}{Y}}\,, \tag{4.27}$$

$$\gamma = \sqrt{ZY}\,. \tag{4.28}$$

If the length of the transmission line is l, the circuit can be modeled as a two port network and the transfer matrix (ABCD) is:

$$\begin{pmatrix} p_i \\ v_i \end{pmatrix} = \begin{pmatrix} \cosh(\gamma l) & Z_0 \sinh(\gamma l) \\ {Z_0}^{-1} \sinh(\gamma l) & \cosh(\gamma l) \end{pmatrix} \begin{pmatrix} p_o \\ v_o \end{pmatrix}, \tag{4.29}$$

where v_i, v_o, p_i and p_o are the input and output velocities and pressures respectively. All short sections (comparing with the applied wavelength) which are modeled with their own ABCD matrices are parts of the acoustical system, and they are connected with other short sections. A benefit of this approach is that if multiple ABCD matrices are cascaded, the resultant ABCD matrix is the product of all matrices in the system. We use this property to describe our system and complex devices. In the case when parts of the structures are not connected in cascade with the system we used matrix transformations and with circuit transformations we obtained the final ABCD matrix. In next chapters particular acoustic systems that have been designed will be described and a detailed explanation of each step used for designing every particular circuit component in the simulations will be given.

5. Near-zero propagation of acoustic waves: compressibility near-zero metamaterials

Near-zero (NZ) metamaterials present a specific subclass of metamaterials, initially demonstrated in the electromagnetic domain [88-93]. Their operation relies on the fact that a non-zero frequency exists at which the wave number is equal to zero. This results in propagation characterized by a constant phase over physically long distances, and gives rise to interesting phenomena such as energy tunneling, super coupling and energy squeezing. By analogy with the EM case, an NZ acoustic metamaterial can be obtained in two ways: by tailoring either its effective mass density or its effective compressibility (the reciprocal of the bulk modulus) to obtain near-zero values at certain frequencies. Recently, different NZ acoustic metamaterials have been proposed [39, 94-98], all of them based on tailoring the effective mass density. In this research a novel class of one-dimensional NZ acoustic metamaterials, based on tailoring the effective compressibility, is analyzed and experimentally demonstrated. This is achieved using resonant-type metamaterials based on the Helmholtz resonator, which has been previously introduced in *Chapter 3* as a building block for single-negative acoustic metamaterials.

5.1 Theory of the near zero propagation

The Helmholtz resonator, used in this research to obtain the resonant behavior of compressibility, consists of a cavity of known volume with rigid walls connected to the host structure by a neck of known length and cross-sectional area. Unit cells based on Helmholtz resonators have already been used as building blocks for acoustic metamaterials, but primarily in the context of single-negative metamaterials that support only evanescent waves [27, 28, 34]. However, here it will be shown that Helmholtz resonators can be used to support near-zero propagation of acoustic waves as well, i.e., that they can be used to build compressibility near zero (CNZ) acoustic metamaterials [99]. In Fig. 5.1 a cross section of the cylindrical duct loaded by a Helmholtz resonator is shown.

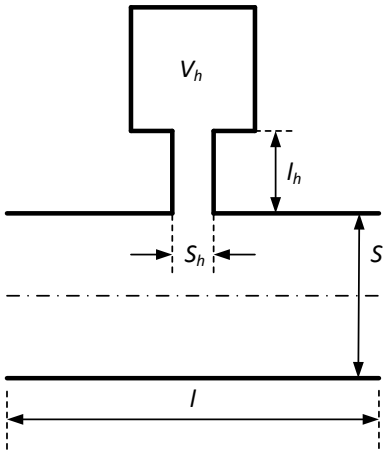

Figure 5.1 Cross section of the duct loaded with Helmholtz resonator with dimensions

In any section of an acoustic duct the difference between the particle velocities at its ends is related to the variability of the volume of the gas through the continuity equation. In the case of a

section of length l and cross-sectional area S, loaded with a Helmholtz resonator with cross-sectional area of the neck equal to S_h, and cavity of volume V_h, this relation can be expressed as follows:

$$dV = S\frac{\partial v}{\partial x}l \cdot dt + S_h \cdot d\xi, \tag{5.1}$$

where V is the volume of the gas in the acoustic duct, v is particle velocity and ξ is the displacement of the gas in the neck. Since $V = Sl$, this can be rewritten as:

$$\frac{dV}{V} = \frac{\partial v}{\partial x}dt + \frac{S_h}{V} \cdot d\xi. \tag{5.2}$$

Under the assumption that sound propagation is an adiabatic process, for which $pV^{\kappa} = \text{const.}$ (i.e. $\kappa p \cdot dV = -V \cdot dp$), where κ is the heat capacity ratio, the previous Eq. (5.2) yields:

$$-\frac{1}{\kappa}\frac{dp}{p} = \frac{\partial v}{\partial x}dt + \frac{S_h}{V} \cdot d\xi, \tag{5.3}$$

or, alternatively:

$$-\beta_0 \cdot dp = \frac{\partial v}{\partial x}dt + \frac{S_h}{V} \cdot d\xi, \tag{5.4}$$

where β_0 is the compressibility of the gas, which, for adiabatic processes, equals $(\kappa p)^{-1}$, and is reciprocal to the bulk modulus B of the gas. The neck of the Helmholtz resonator thus acts as a sink, which effectively modifies the continuity equation. However, if the proposed structure is considered to be a unit cell of an acoustic metamaterial, the influence of the Helmholtz resonator, which can be viewed as the "internal inhomogeneity" of the cell, can be expressed through the effective compressibility β_{eff} as follows:

$$-\beta_{\text{eff}} \cdot dp \overset{\text{def}}{=} \frac{\partial v}{\partial x}dt. \tag{5.5}$$

Combining the previous two Eqs. (5.5) and (5.4) yields:

$$\beta_{\text{eff}} = \beta_0 + \left(\frac{dp}{dt}\right)^{-1}\frac{S_h}{V} \cdot \frac{d\xi}{dt}. \tag{5.6}$$

Let us now consider the differential equation for the displacement of the gas in the neck of a Helmholtz resonator (if losses are neglected):

$$\rho l_h' \frac{d^2\xi}{dt^2} + \rho c^2 \frac{S_h}{V_h}\xi = p, \tag{5.7}$$

where $l_h' = l_h + \frac{16r_h}{3\pi}$ is the effective length of the neck, with $r_h = \sqrt{S_h/\pi}$ being its radius. The solution of the Eq. (5.7), if the harmonic expressions $p = Pe^{-i\omega t}$ and $\xi = \Xi e^{-i\omega t}$ are introduced, is the following:

$$\Xi = \frac{P}{\rho c^2 \frac{S_h}{V_h} - \rho l_h' \omega^2}. \tag{5.8}$$

Introducing this into the Eq. (5.6) rewritten in the complex form yields the expression for the effective compressibility of the proposed metamaterial unit cell:

$$\beta_{\text{eff}} = \beta_0\left(1 + \frac{S_h}{V} \cdot \frac{1}{\frac{S_h}{V_h} - l_h\frac{\omega^2}{c^2}}\right). \tag{5.9}$$

This expression suggests that it is possible to achieve zero effective compressibility at a certain frequency. In COMSOL we designed and simulated a simple air filled short section of an acoustic duct loaded with a Helmholtz resonator with dimensions S= 206 mm^2, S_h= π mm^2, c= 343.12 m/s (T= 293.15 K), β_0= 7.04 Pa^{-1}, l= 32 mm, l_h= 28 mm, V_h= 567 mm^3. The simulated response of the proposed structure (with losses) and its effective compressibility, extracted using the approach described in *Chapter 4*, reveal a notch in the frequency response due to negative values of effective compressibility around the resonance of the Helmholtz resonator, Fig. 5.2.

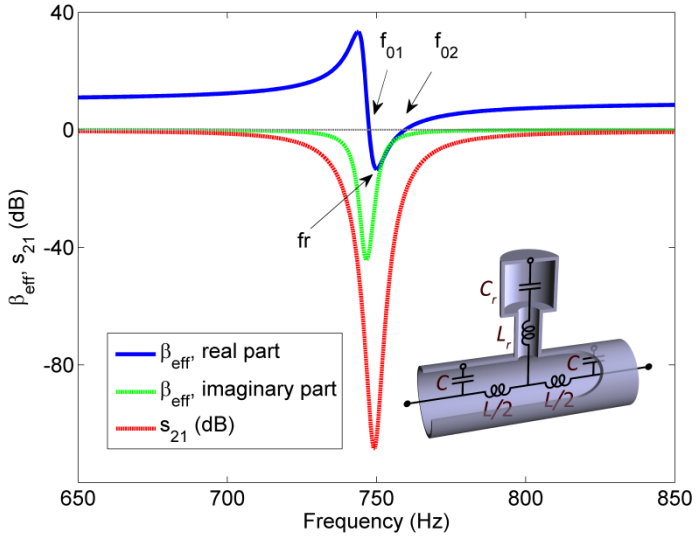

Figure 5.2 Typical transmission coefficient and effective compressibility of the unit cell (shown in the inset, with its equivalent electrical circuit).

To verify the results obtained from the simulation, the real part of the effective compressibility obtained from the Eq. (5.9) is plotted in Fig. 5.3, together with the real part of the effective compressibility obtained from numerical simulations.

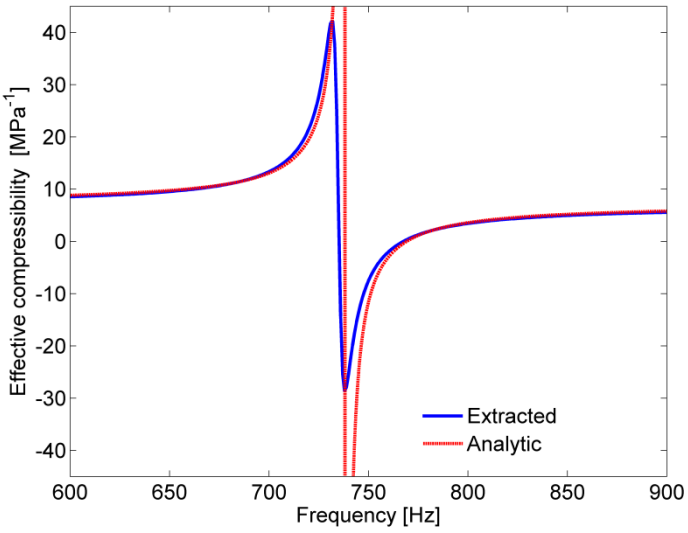

Figure 5.3 Comparison of the effective compressibility of the Helmholtz resonator obtained from the analytical expression and from FEM simulations

A very good agreement is observed, with the only difference due to losses, which are taken into account in COMSOL and disregarded in the analytical solution. Although it may seem at first that any metamaterial unit cell will support NZ propagation at a certain frequency, we show that the host structure needs to be carefully designed and that not one but two frequencies exist capable of supporting NZ propagation, finally leading to the development of NZ acoustic devices with novel characteristics. Furthermore, β_{eff} equals zero at not one but two frequencies in the vicinity of f_r, denoted f_{01} and f_{02}, where propagation of CNZ nature might be expected. However, the imaginary part of β_{eff} at f_{01} is very large, and therefore no propagation occurs due to high losses. At f_{02}, the imaginary part of β_{eff} is smaller, but still non-zero, and consequently the insertion loss is lower but still not negligible. Therefore, by using a simple short section of an acoustic duct as a host, CNZ propagation cannot be practically achieved either at f_{01} or at f_{02}.

Now the conditions needed to achieve CNZ propagation in practice will be analyzed in detail. Instead of a simple duct, a simple lowpass filter (LPF) of the 3rd order is proposed as a host structure, although it should be noted that this analysis can be applied to other hosts. A host has to have a stopband region around the resonance and cannot be a single negative medium to avoid the double negative propagation. The central section of the LPF is loaded with one Helmholtz resonator, designed so that its resonant frequency falls within the stopband of the LPF. Two LPFs were analyzed: CLC-LPF, modeled as shown in Fig. 5.4a, and its dual, LCL-LPF, modeled as shown in Fig. 5.4b.

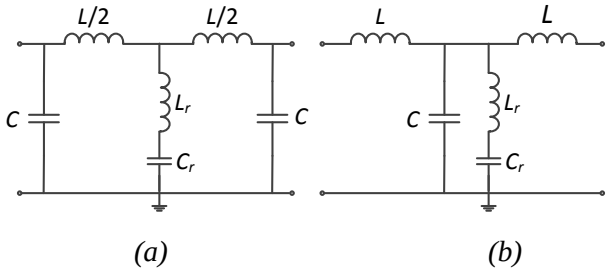

Figure 5.4 Equivalent circuit of the Helmholtz resonator-loaded (a) CLC-LPF, and (b) LCL-LPF. To preserve the symmetry, the inductor of CLC-LPF is modeled with two inductances equal to L/2

In such an environment, Helmholtz resonator is driven by pressure variations in the channel regardless of whether it is located at the inductive or the capacitive section of the acoustic filter. It should be noted that the equivalent circuits from Fig. 5.4 are in essence the same as those of a short section of a Helmholtz resonator loaded simple duct. The only difference is in the actual values of L and C: whereas in the case of LPF, L and C are significantly larger than L_r and C_r, in the case of a simple duct they are very similar. Therefore, to analyze the influence of the type of the host to CNZ propagation, the influence of decreasing L and C was analyzed. In Fig. 5.5, the responses of both circuits are compared to the responses of original LPFs.

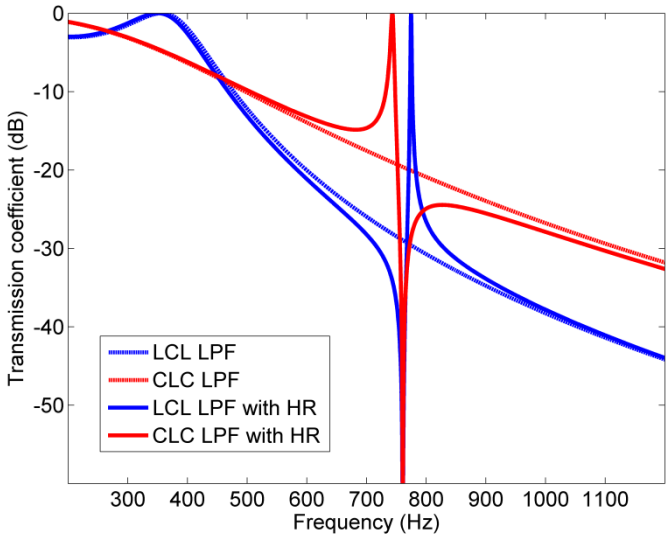

Figure 5.5 Comparison of simulated lossless responses of equivalent electrical circuits of acoustic CLC- and LCL- low-pass filters, and the same low-pass filters loaded with one Helmholtz resonator at their central sections.

It can be seen that the inclusion of the Helmholtz resonator in both cases results in a new transmission peak and a new transmission zero in the stopband of LPF. As expected, the transmission zero always occurs at f_r. However, the transmission peak occurs at a frequency higher than f_r for Helmholtz resonator coupled to the capacitive section and lower than f_r for Helmholtz resonator coupled to the inductive section of the filter. To analyze the nature of obtained transmission peaks, the frequency at which CNZ propagation occurs is derived analytically, for both Helmholtz resonator loaded CLC-LPF and LCL-LPF.

Provided that the overall length l of the analyzed structures is sufficiently small, they can be regarded as homogenous, and their effective wave number can be calculated. We note that this condition holds, although it might seem that in the actual implementation both structures are long with respect to the guided wavelength. However, as it will be shown, at the CNZ frequency the structures support CNZ propagation with constant phase over physically long distances, so they are in fact short with respect to the wavelength and the homogenization process can be applied. The complex wavenumber $k = k' + jk''$ can be calculated from the ABCD matrix as $kl = \arccos(D)$. In the case of the Helmholtz resonator loaded CLC-LPF, D can be obtained as:

$$D = 1 + \frac{\frac{1}{Z_L + 2Z_r} + j\omega C}{\frac{Z_r}{Z_L(Z_L + 2Z_r)}} \tag{5.10}$$

where $Z_L = j\omega L/2$ and $Z_r = \left(1 - \omega^2 L_r C_r\right) \Big/ j\omega C_r$. Similarly, for the Helmholtz resonator loaded LCL-LPF, D is equal to:

$$D = 1 - \frac{\omega^2 LC}{1 - \omega^2 L_r C_r}\left(1 + \frac{C_r}{C} - \omega^2 L_r C_r\right) \tag{5.11}$$

The attenuation constant k' and the wave number k'' obtained from Eqs. (5.10) and (5.11) are plotted in Fig. 5.6.

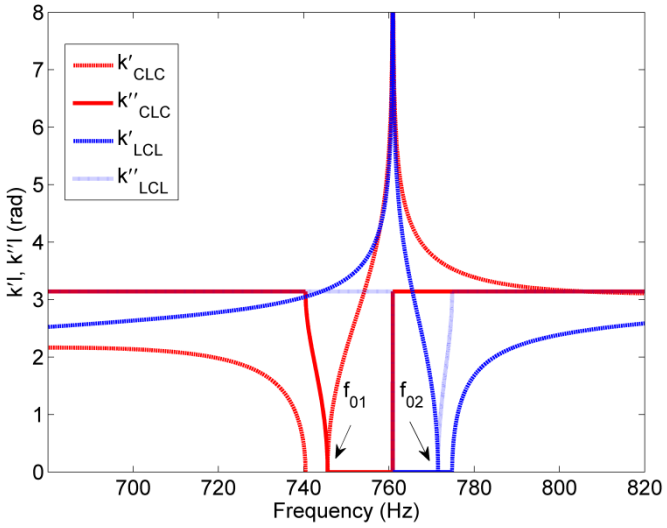

Figure 5.6 Attenuation constant k' and wave number k'' for the Helmholtz resonator loaded CLC-LPF and LCL-LPF. The values of circuit elements are chosen as typical for acoustic circuits: L= 2500 H_a, C= 0.14 nF_a, L_r= 11150 H_a, C_r= 3.93 pF_a (where units H_a and F_a are "acoustical" henry and "acoustical" farad, defined as H_a= kg/m^4 and F_a= m^3/Pa).

It can be seen that k'' equals zero at two different frequencies, f_{01} and f_{02}, the first one before and the other one after the stopband. In fact, CNZ propagation will be supported only at the one of these frequencies where the condition $D=1$ is fulfilled, i.e. where $k'=0$. In the case of the Helmholtz resonator loaded CLC-LPF, this frequency is f_{01}, which is obtained from Eq. (5.10) by equating D to 1:

$$f_{01}=\frac{1}{2\pi\sqrt{\frac{2CC_r}{2C+C_r}\left(L_r+\frac{L}{4}\right)}}. \tag{5.12}$$

In the case of the HR-loaded LCL-LPF, this frequency is f_{02}, obtained similarly from (5.11):

$$f_{02}=\frac{1}{2\pi\sqrt{L_rC_r}}\sqrt{1+\frac{C_r}{C}}, \tag{5.13}$$

CNZ frequencies f_{01} and f_{02} correspond to central frequencies of two transmission peaks in Fig. 5.5. It can thus be concluded that the frequency at which CNZ propagation actually occurs, f_{01} or f_{02}, depends on whether the host is inductive or capacitive. For a given Helmholtz resonator (i.e. for fixed L_r and C_r), the CNZ frequency of the Helmholtz resonator loaded LCL-LPF (5.13) depends only on C. It should be noted that since $f_{02}>f_r$ for all values of C, the CNZ transmission peak will always occur above the transmission zero at f_r, as was the case in Fig. 5.5. If C is sufficiently large, f_{02} approaches f_r. However, if C is significantly decreased, f_{02} increases quite rapidly, thus shifting the CNZ frequency out of the range of interest and finally into the range where the second harmonic of LPF is positioned. For that reason, a simple acoustic duct cannot be practically used as a host in CNZ structures since its capacitance C is too low. A similar analysis can be performed for Helmholtz

resonator loaded CLC-LPF. Apart from the host capacitance *C*, in this case the CNZ frequency depends also on the host inductance *L*, Eq. (5.12). For values of *L* and C typical for an acoustic LPF, e.g. for $L = 2500\ H_a$ and $C = 0.14\ nF_a$, are f_{01} will be smaller than f_r. This corresponds to a situation in which CNZ transmission peak occurs below the transmission zero at f_r, as was the case in Fig. 5.5. However, if *L* or *C* are decreased, f_{01} increases and eventually becomes larger than f_r. For sufficiently small *L* and *C*, f_{01} behaves as f_{02}, i.e. both types of LPFs behave as simple acoustic ducts, not suitable to be used as CNZ hosts.

5.2 Simulation models and results

A structure used to verify compressibility near-zero propagation was designed and simulated in the COMSOL multiphysics FEM simulator and transmission line model was designed based on ABCD matrices as described in the *Chapter 4*. To increase the visibility of the near-zero effect, we opted for a CLC-LPF and loaded each of its capacitive sections with one Helmholtz resonator, as shown in Fig. 5.7. Dimensions of Helmholtz resonator are: cavities $\varnothing 8.5 \times 10$ mm, cylindrical necks $\varnothing 2 \times 28$ mm, and of CLC-LPF: C sections $\varnothing 52 \times 20$ mm, L section $\varnothing 10 \times 80$ mm. The overall length of such a CNZ metamaterial is 120 mm i.e. approximately 0.3λ, where λ is the sound wavelength in the air at the CNZ frequency, arbitrarily chosen to be $f_0 = 760$ Hz. The CNZ metamaterial is inserted in an acoustic duct, $\varnothing 16 \times 500$ mm on both sides.

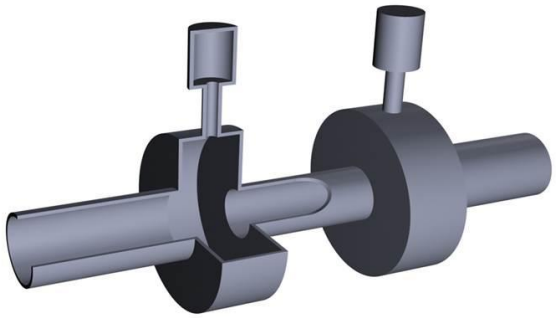

Figure 5.7 Compressibility near-zero (CNZ) metamaterial

5.2.1 Simulation model in COMSOL Multiphysics

The first model was designed and simulated in COMSOL Multiphysics FEM simulator. Two structures were designed, the compressibility near zero metamaterial (Fig. 5.7) and the CLC-LPF with same dimensions like in the near-zero structure just without Helmholtz resonators. From the layout of the structure it can be seen (Fig. 5.7) that the system does not contain any mechanical element such as a membrane and in this case the pressure acoustic model is enough for a complete modeling of the system. In this model just the inner part of the tubes was defined within the simulator and the walls of the tubes were modeled with hard wall boundary. Plane wave radiation was used as a sound source and the open end of the outlet tube was modeled with PML boundary condition. Four boundary probes were placed in the system as described in *Chapter 4*, and the obtained pressure values were

used to calculate the transmission (S_{21}) and reflection parameters (S_{11}) according to Eqs. (4.1) and (4.2). Frequency domain solver was used to simulate the metamaterial in the frequency range from 200 Hz to 2 kHz. Simulation was done without losses, the narrow pipe effect was not included, because in COMSOL 4.0 was not possible to include this type of losses and the viscous losses in the air itself are negligible. Simulation results (transmission parameters) for compressibility near-zero metamaterial and the conventional CLC-LPF in the lossless case are shown in Fig. 5.8.

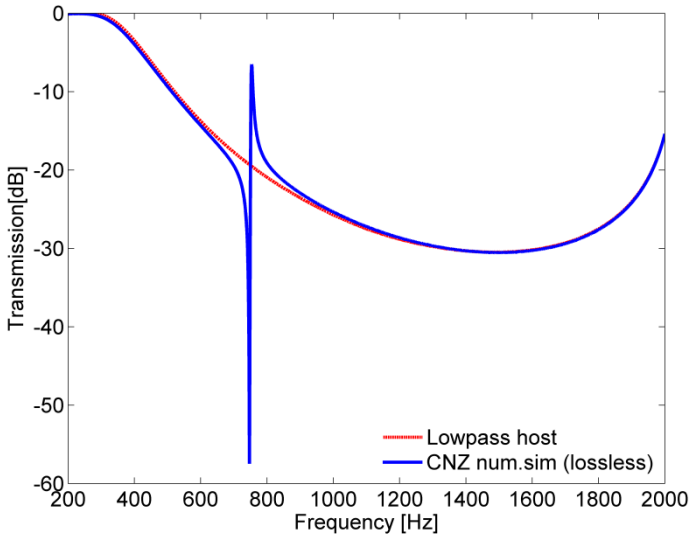

Figure 5.8 Simulated transmission coefficient of the CLC-LPF and the CNZ metamaterial (lossless)

From the simulation results it can be concluded that the theoretical prediction was right and a new transmission zero and a new transmission peak appear in the stopband region of the LPF. The transmission zero is on a lower frequency than the peak, exactly as predicted in the case of Helmholtz resonator loaded capacitive section. The compressibility near-zero nature of propagation in the narrow pass-band around f_0 is further validated by an almost constant value of phase along the axis of the compressibility near-zero metamaterial, Fig. 5.9. In the case of a conventional acoustic duct of the same length, a total phase shift of over 80° is accumulated. However, in the case of the compressibility near-zero metamaterial, this phase shift is reduced to only 5.7°. Although the compressibility near-zero metamaterial is long in terms of guided wavelengths, it exhibits a relatively constant phase, implying that an acoustic wave does not propagate but rather tunnels through it with an effectively infinite phase velocity. As a consequence, incoming waveforms are replicated at the output port, and the transmission properties of such a medium are uniquely characterized by its ports only. Moreover, the flat phase distribution in Fig. 5.9 demonstrates that compressibility near-zero propagation is not only an "effective" phenomenon visible solely at the ports, but rather a characteristic of the entire medium. For example, if two independent acoustic waves propagate through compressibility near-zero metamaterial, at any particular moment they interfere in an identical way at each point. This gives rise to another peculiarity of compressibility near-zero media:

since there is no phase change in the direction of propagation, unit cells can be of arbitrary length, not necessarily sub-wavelength. The unit cell of the proposed compressibility near-zero metamaterial could be identified in various ways, e.g. as a capacitive section loaded with a Helmholtz resonator followed by an inductive section. By cascading such unit cells, relatively large with respect to the wavelength, one-dimensional compressibility near-zero acoustic metamaterials of arbitrary length can be made.

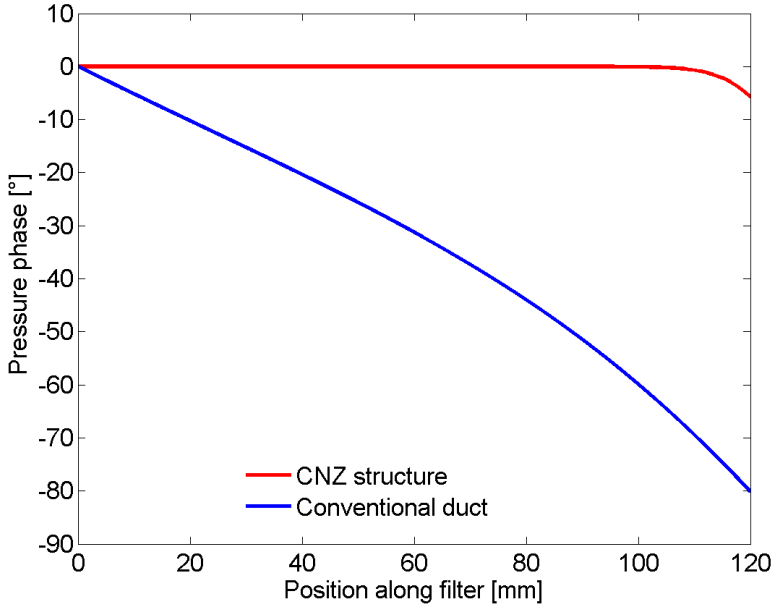

Figure 5.9 Simulated phase distribution along the axis of the CNZ metamaterial at the CNZ frequency $f_0 = 760$ Hz *compared to the phase along a conventional duct of the same overall length*

5.2.2 Transmission line simulation model for a compressibility near-zero structure

The compressibility near zero metamaterial also was modeled using transmission line theory (*Chapter 4*). Every section was modeled as a transmission line section with series acoustic impedance and shunt acoustic admittance and characterized by ABCD matrices. ABCD matrices for all sections were connected in cascade. The block diagram of a compressibility near-zero metamaterial is shown in Fig. 5.10.

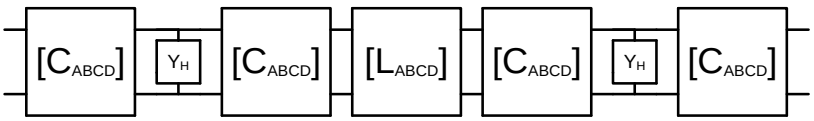

Figure 5.10 Block diagram of the near-zero metamaterial

The structure consists of seven blocks which are connected in cascade. C_{ABCD} block is the ABCD matrix for a half-length capacitive duct in the third order low pass filter, because the Helmholtz resonator is placed in the middle of the capacitive section and to model this, the capacitive section was split into two sections between which the Helmholtz resonator was placed. L_{ABCD} block is the ABCD matrix of the inductive section of the third order low pass filter. The Helmholtz resonator

was modeled with a shunt connected admittance matrix (Y_H block) and using matrix transformations it was transformed into the equivalent cascade connected ABCD matrix. After the transformation the equivalent ABCD matrix for the whole system was calculated in the frequency range from 200 Hz to 2 kHz and transformed to the final acoustic scattering matrix. The inner and outer duct were included in the system through the acoustic characteristic impedance $Z_0=2\cdot10^6$ [Pa·m^{-3}] in the transformation of the equivalent ABCD matrix to S matrix [69]. The *Matlab* code for modeling compressibility near zero metamaterial is given in *Appendix A3*. The calculated values of the unit length acoustic series inductance and the acoustic shunt capacitance for all tube sections in the system are given in Table 5.1.

TABLE 5.1 SERIES INDUCTANCE AND SHUNT CAPACITANCE VALUES

Elements	Unit length acoustic series inductance [kg/m^5]	Unit length acoustic shunt capacitance [m^2/Pa]
Inductive section in LPF	$1.5915\cdot10^4$	$5.4353\cdot10^{-10}$
Capacitive section in LPF	588.5908	$1.4697\cdot10^{-8}$
Inductive section HR	$3.9789\cdot10^5$	$2.1741\cdot10^{-11}$
Capacitive section HR	$2.2028\cdot10^4$	$3.9270\cdot10^{-10}$

Simulation was done without and with losses (narrow pipe effect). In the lossless case in the Eqs. (4.21) and (4.22) values of F_v and F_t were set to zero. The simulation results with and without losses are shown in Fig. 5.12.

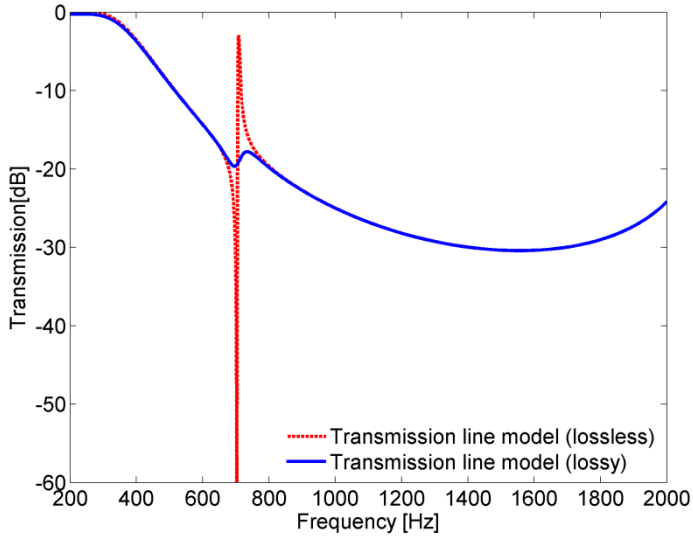

Figure 5.11 Simulated transmission coefficient of the compressibility near-zero metamaterial in transmission line model without and with losses

Transmission line simulation results are the same as the results from the FEM simulation. The new near-zero transmission peak is created at f_0= 760 Hz. When all losses are included in the model, it results in 15dB attenuation in the transmission peak. Due to narrow necks of the Helmholtz

resonator, thermo-viscous losses are significant, which explains relatively large insertion losses at f_0 in the lossy simulation model.

5.3 Fabrication and measurements

For experimental verification of theoretical and numerical results the compressibility near zero metamaterial from Fig. 5.7 was fabricated with the same dimensions as shown in previous section. Based on the method for extraction of acoustic scattering parameters from *Chapter 4*, laboratory measurement system for measurement acoustic S-parameters was developed and the CNZ structure was characterized with developed system and compared with simulation results.

5.3.1 Fabricated CNZ metamaterial

The entire CNZ structure and the feed acoustic ducts are made of steel. The cavity and neck of the Helmholtz resonators were engraved by mechanical drilling on metallic slabs before being assembled together with other elements. The fabricated structure is shown in Fig. 5.12.

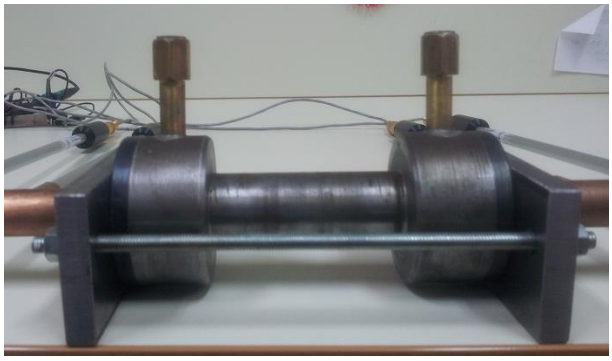

Figure 5.12 Fabricated CNZ structure

5.3.2 Experimental setup

The measurement of acoustic S-parameters was based on the method described in *Chapter 4.* Based on this method a laboratory measurement system for determining the acoustic S-parameters (an acoustic vector network analyzer) was developed. The laboratory measurement system is shown in Fig. 5.13.

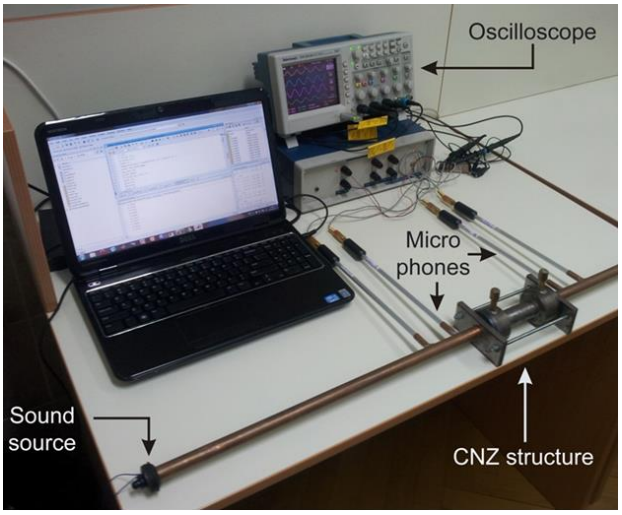

Figure 5.13 Laboratory measurement system for measuring acoustic S-parameters

The system consists of five basic elements: the sound source, four calibrated microphones, coaxial cables, digital oscilloscope and a computer used for signal generation, signal processing and acquisition. Sinusoidal signal of a certain frequency was generated by the program Audacity 1.3.13, on the computer with a sound controller of type IDT 92HD87B1, IDT High Definition Audio Codec. The signal was sent to electroacoustic transducers (speakers) of type FLAT 34 OD02902Y.L, as shown in Fig. 5.14.

Figure 5.14 Electroacoustic transducer (speaker) of type FLAT 34 OD02902Y.L

The sound was generated in the range of 200-1000 Hz with 20 Hz steps, decreased to 0.25 Hz in the near-zero range. The measurements were made using four calibrated microphones (EMM-8, iSEMcon) mounted with their front surfaces aligned flush with the internal duct wall, through small openings in the wall. Microphone EMM-8, iSEMcon with a small diameter (approx. 8 mm) and with length 314 mm shown in Fig. 5.15 is an electret condenser microphone and bias voltage (5V) was needed to supply the built in FET. The microphones were placed at the distances of 50 mm and 100 mm from each side of the CNZ structure, and the measured levels of acoustic pressure in the duct at these points were used to recover the direct and the reflected acoustic wave and calculate the S-parameters.

Figure 5.15 Microphone EMM-8 iSEMcon

Microphones were connected with four-channel digital oscilloscope Tektronix TDS 2024B via four coaxial cables of the same lengths. For the characterization of the coaxial cables, the impedance magnitude and the phase of the cables were measured with HP4194A Impedance/Gain Phase Analyzer in the frequency range from 100 Hz to 1 kHz. Measured impedance characteristic magnitude $|Z|$ and the phase Θ for four coaxial cables are shown in Figs. 5.16a and b.

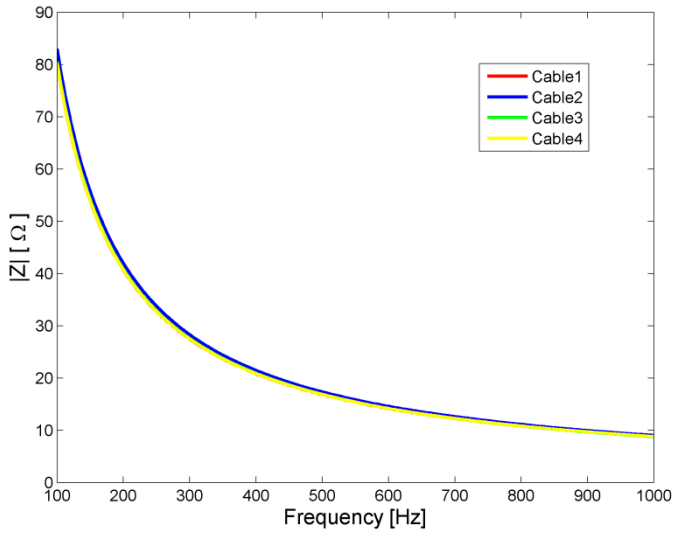

a)

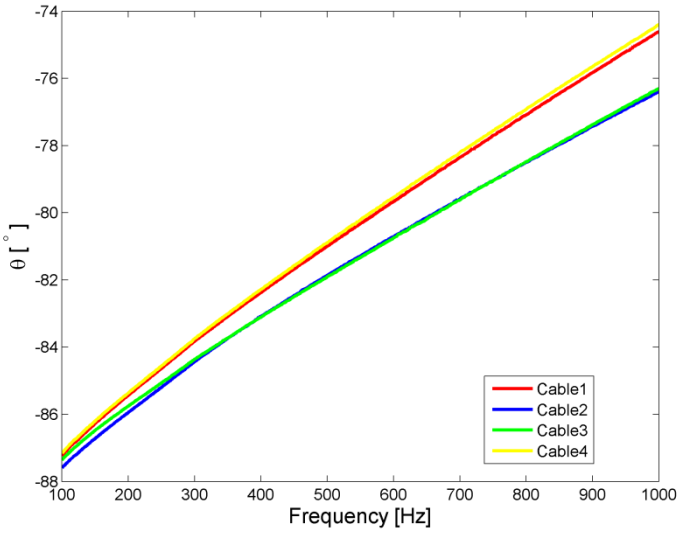

b)

Figure 5.16 Impedance characteristic of the coaxial cables which were used during the measurements: a) magnitude b) phase

From measured results it can be seen that the magnitude characteristics for the four cables overlap almost completely, just a slight difference can be observed. But as regards phase characteristics it can be seen that the first cable and the fourth overlap almost completely, as well as the second and the third cable, but between these pairs there is a difference of about 2°. This difference was significant and as it could distort the measured values, it had to be taken into account. Based on these measurement results the system was calibrated, and the differences in magnitudes and phases between the cables were automatically corrected by post-processing. A four-channel digital oscilloscope Tektronix TDS 2024B (Fig. 5.17) was used to measure the electrical signal from the microphones. In all channels the entire waveform (2500 samples on each channel) was measured and saved at the same time.

Figure 5.17 Four channel digital oscilloscope Tektronix TDS 2024B

From the digital oscilloscope measured signals were sent to the computer for further processing. The measured signals from all four channels, at the same frequency, which in this example is 710 Hz, are shown in Fig. 5.18.

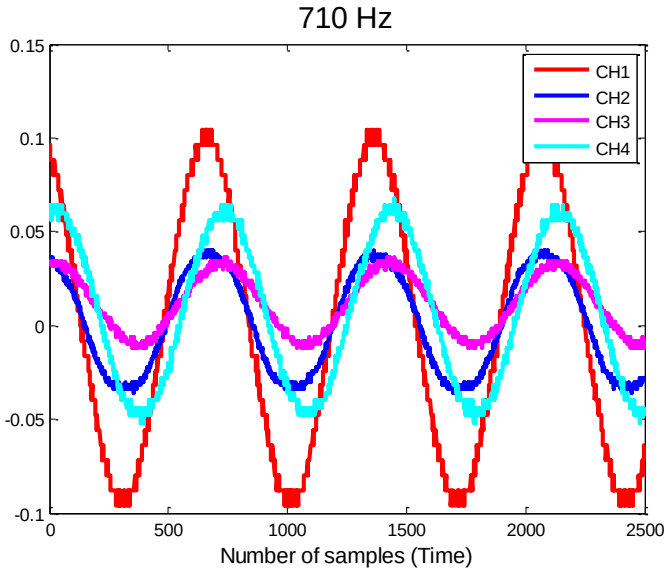

Figure 5.18 Measured signals from all four channels, at the same frequency (710 Hz)

The same process was repeated for all frequencies of interest, i.e. from 200 Hz to 1000 Hz with 20 Hz steps, decreased to 0.25 Hz in the NZ range (755 Hz-765 Hz). The measured signals were sent to the computer for signal processing.

5.3.3 Signal processing and data acquisition

Signal processing and data acquisition consist of three parts, noise reduction (filtering), estimation of the amplitude and phase of the measured signals, and calculating the acoustic S-matrix using Eqs. (4.1) and (4.2). The first part is the filtering of high frequency components of the measured signal (higher harmonics and noise). A 3dB digital resonator with the resonance frequency coresponding to the frequency of the excitation signal was implemented as a filtering element [100-101]. The block diagram of the implemented digital resonator and its transfer function are shown in Figs. 5.19a and b.

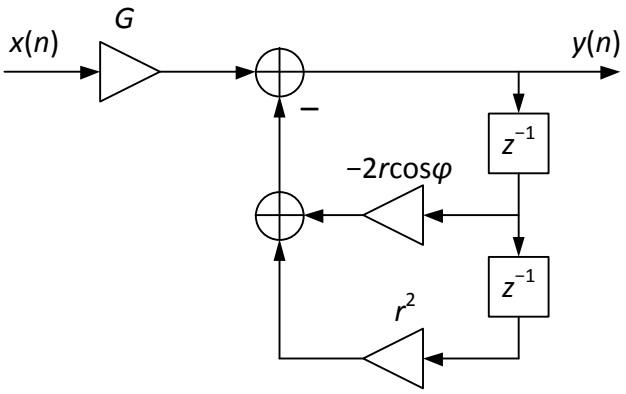

a)

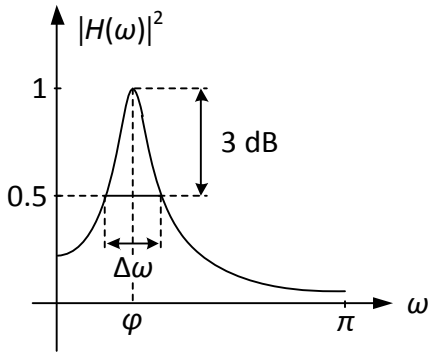

b)

Figure 5.19 Digital 3dB resonator a) block diagram, b) transfer function

The transfer function of the resonator in the complex domain is:

$$H(z) = \frac{G}{(1-re^{j\varphi}z^{-1})(1-re^{-j\varphi}z^{-1})}, \tag{5.14}$$

where:

$$G = (1-r)\sqrt{1-2\cos 2\varphi + r^2}\,. \tag{5.15}$$

The phase change $\Delta\varphi$ that occurs when the signal passes through the resonator is equal to:

$$\Delta\varphi = \arg\left(1 - 2r\cos\varphi\, e^{-j\varphi} + r^2 e^{-j2\varphi}\right), \tag{5.16}$$

where φ is the resonance frequency of the resonator normalized by the sampling frequency f_s:

$$\varphi = 2\pi\frac{f_0}{f_s}\,, \tag{5.17}$$

The parameter r is defined with respect to the 3 dB bandwidth $\Delta\omega$ as follows:

$$r = 1 - \frac{\Delta\omega}{2}\,, \tag{5.18}$$

where in this case $\Delta\omega = 0.02$. The output signal $Y(z)$ in the complex domain is:

$$Y(z) = H(z)X(z), \tag{5.19}$$

where *H(z)* is the transfer function of the resonator, defined by Eq. (5.14), and *X(z)* is the input signal in the complex domain. After the filtering just pure sinusoidal signals remain, at the desired frequency. In the second part of processing the amplitude and phase of the periodic signal are determined, thus obtaining the pressure phasor. The measured sinusoidal signal can be written in the following form:

$$y_M = A_M \sin(\omega_0 t + \Theta_M)\,, \tag{5.20}$$

where A_M *and* Θ_M have unknown values, amplitude and phase of the measured signal, respectively. The amplitude of the measured signal is determined as the square root of the signal power:

$$A_M = \sqrt{R_{yy}[0]} = \sqrt{P_y}\,, \tag{5.21}$$

which is calculated from the autocorrelation of the measured signal:

$$R_{yy}[n] = \sum_{k=0}^{N-1} y[k]\, y[n+k]\,. \tag{5.22}$$

Before determining the unknown phase of the measured signal, it is necessary to define a new sinusoidal signal with amplitude equal to one and zero initial phase, and with the same frequency like the unknown signal. The new sinusoidal signal is, therefore, defined as:

$$g = \sin(\omega_0 t). \tag{5.23}$$

Discrete (cyclic) convolution of the newly defined signal and the filtered input signal is given by:

$$\Xi = (g \circledast y_M)(n) = \sum_{n=1}^{N} y_M(m)\, g(n-m). \tag{5.24}$$

The convolution of two signals reaches an extreme value (peak) when the two signals are in phase folded, or when the signals are in phase. After processing, the unknown phase of the measured signal with the included phase shift from the digital resonator (Δφ) becomes:

$$\Theta_M = 2\pi \frac{n_M}{N} + \Delta\varphi \tag{5.25}$$

where *N* is the total number of samples. After determining the amplitude and phase of the measured signal it is possible to reconstruct the measured signal in the form Eq. (5.20). A comparison of the measured and reconstructed signals on all four channels at the same frequency is shown in Fig. 5.20.

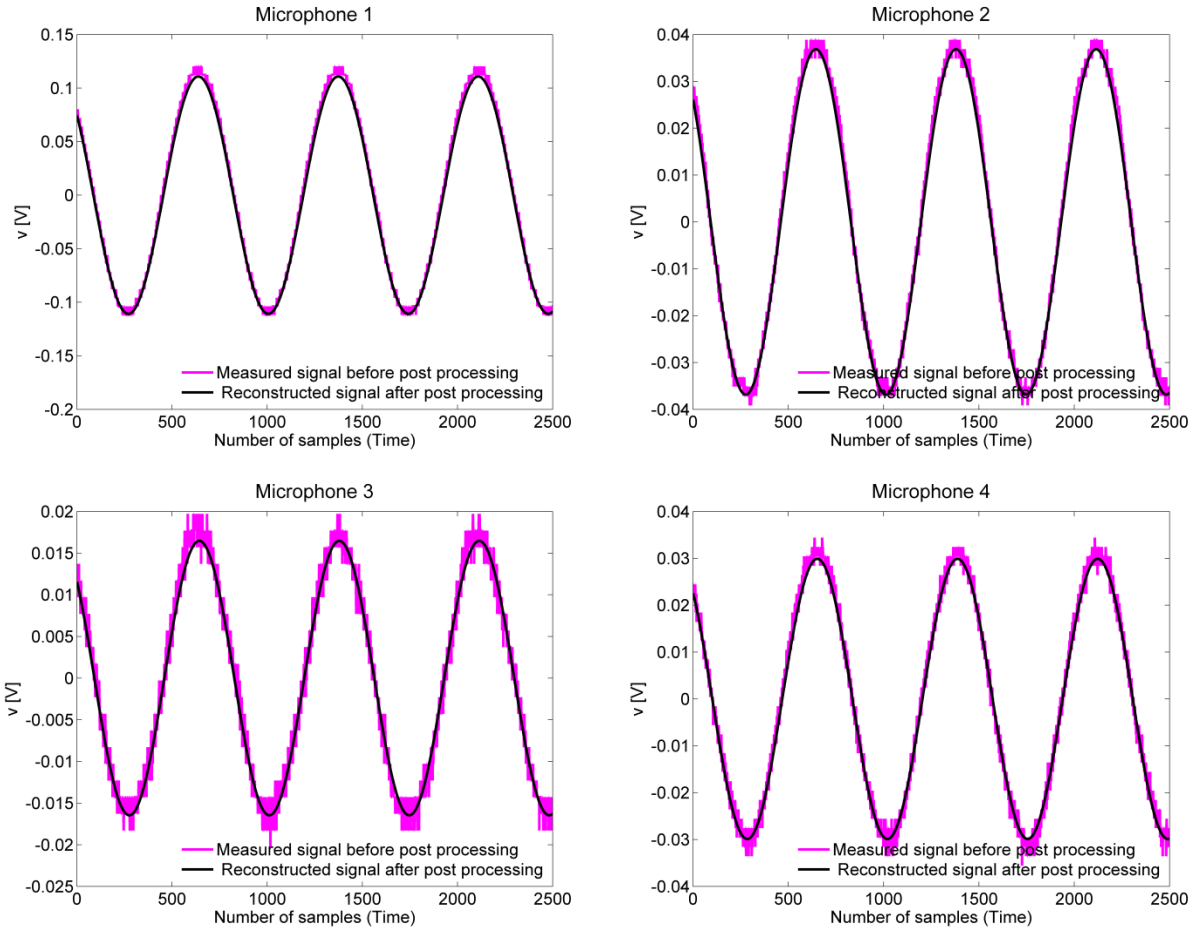

Figure 5.20 Measured (magenta) and reconstructed (black) signals

The reconstructed signal can be written in phasor form:

$$y_M = |A_M| e^{j\Theta_M} \tag{5.26}$$

Signals expressed in this form are convenient for use in Eqs. (4.1) and (4.2), from which the acoustic S-parameters for any unknown two port linear time invariant acoustic circuit can be obtained. *Matlab* code for a signal processing is given in *Appendix A4.*

5.4 Measurement results

The fabricated compressibility near-zero metamaterial was measured using the technique described in the previous section. Fig. 5.21 shows measured transmission coefficients from three sets of measurements in the frequency range from 600 Hz to 920 Hz.

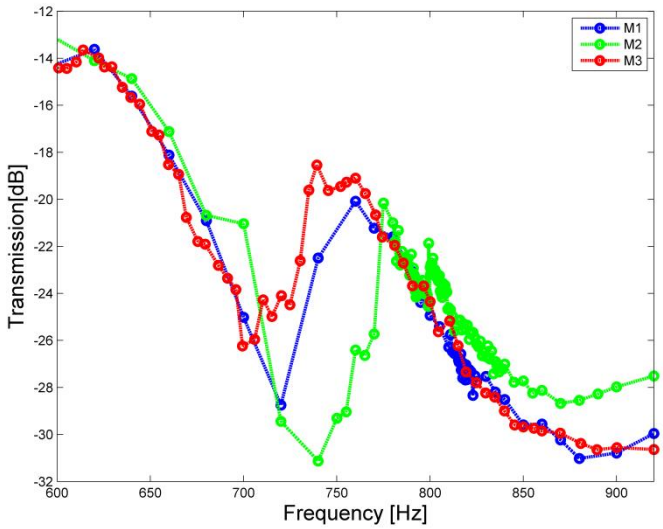

Figure 5.21 Measurement results for three sets of measurement

Between the different sets of measurement there is a good agreement with a slight shift of the resonant peak. This small variation is a result of external parameter variations, such as room temperature variation. The relatively large measured insertion losses at the near-zero frequency are the consequence of the significant narrow pipe effect in the necks of the Helmholtz resonators. Figure 5.22 shows the simulation results from FEM and transmission line model with and without losses compared with the measured results.

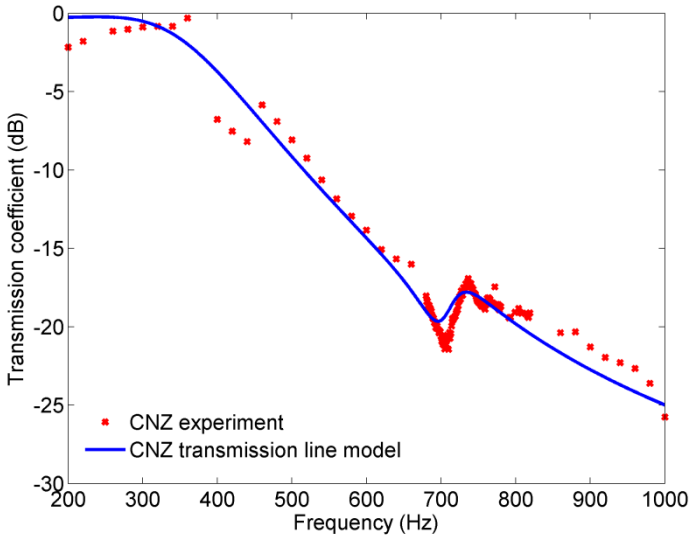

Figure 5.22 Compared simulation and measured results

Measured and the simulation results where all losses are included are in good agreement, which validates our theoretical predictions.

5.5 Applications of Helmholtz resonator based near-zero metamaterials

5.5.1 Reducing insertion losses and increasing near-zero bandwidth

To demonstrate the versatility of the approach, we varied the number of resonators loading each of the capacitive sections of the host filter, Fig. 5.23.

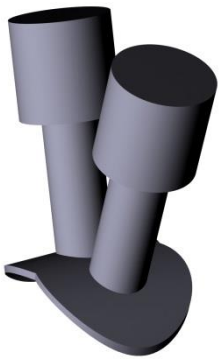

Figure 5.23 Multiple Helmholtz resonators

This affects the compressibility near-zero frequency only slightly, but it significantly reduces the insertion loss and increases the fractional bandwidth due to coupling between resonators. Such behavior is desirable from the point of view of practical applications and it can be controlled by conventional filter design methods. In Fig. 5.24 it is shown how the insertion losses decrease if the number of Helmholtz resonators increases.

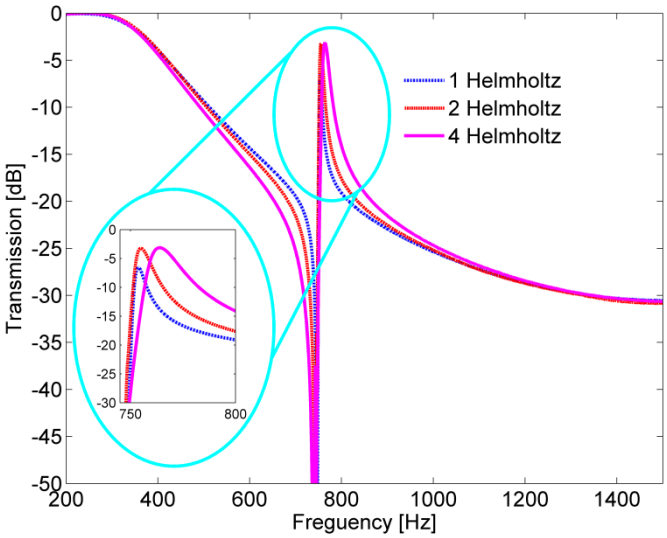

Figure 5.24 Reduced insertion losses and increased bandwidth

5.5.2 Multiband compressibility near-zero propagation

A similar approach can be used to achieve simultaneous compressibility near-zero propagation at multiple arbitrary frequencies, provided that unit cells with multiple resonant frequencies are used instead of regular Helmholtz resonators. For example, a double Helmholtz resonator [102], shown in Fig. 5.25, supports two resonant frequencies, which depend on the individual dimensions of cavities and necks and thus can be independently engineered.

a)

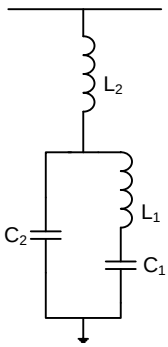

b)

Figure 5.25 Double Helmholtz resonator a) layout, b) equivalent circuit model

A double Helmholtz resonator connected to a conventional duct produces a double notch. Figure 5.26 shows the transmission and reflection characteristic of the conventional duct loaded by a double Helmholtz resonator.

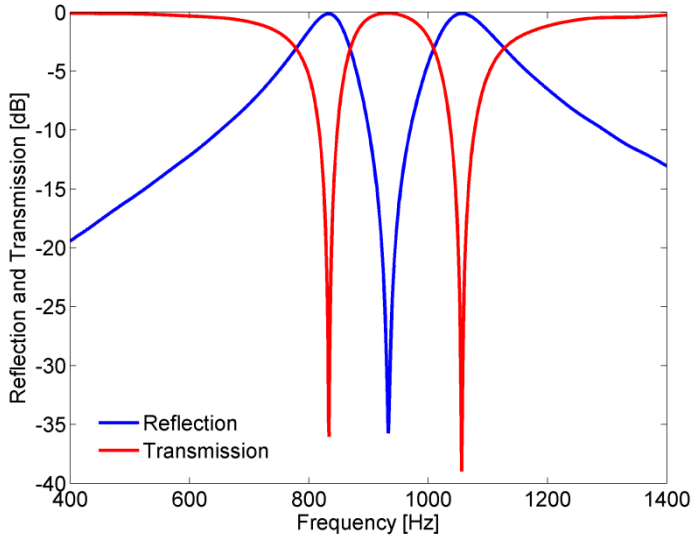

Figure 5.26 Reflection and transmission coefficient of the double Helmholtz Resonator

The resonant frequencies where the notches are located can be calculated from the equivalent circuit model:

$$f_{r1} = \sqrt{\frac{L_1C_1+L_2C_1+L_2C_2-\sqrt{(L_1C_1+L_2C_1+L_2C_2)^2-4L_1L_2C_1C_2}}{2L_1L_2C_1C_2}}, \tag{5.27}$$

$$f_{r2} = \sqrt{\frac{L_1C_1+L_2C_1+L_2C_2+\sqrt{(L_1C_1+L_2C_1+L_2C_2)^2-4L_1L_2C_1C_2}}{2L_1L_2C_1C_2}}. \tag{5.28}$$

The extracted real and imaginary parts of effective compressibility are shown in Fig. 5.27. At both resonant frequencies the effective compressibility has a negative value and follows the Lorentzian-type shape.

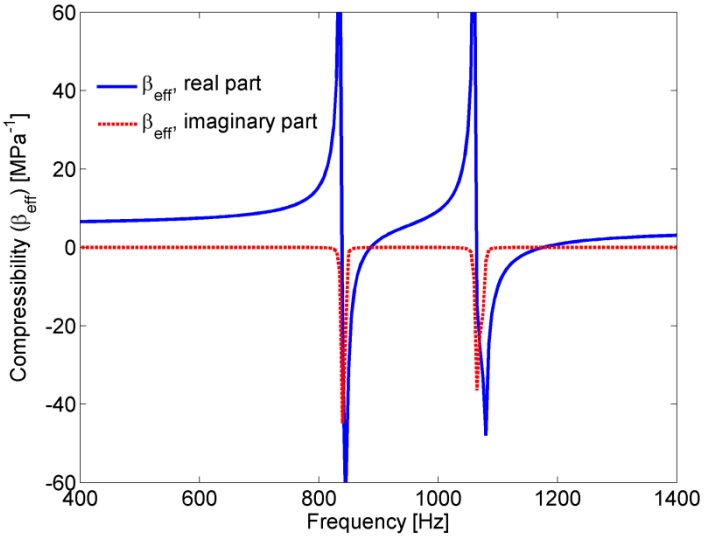

Figure 5.27 Extracted effective compressibility for a double Helmholtz resonator

By replacing Helmholtz resonators in the system shown in Fig. 5.7 with double Helmholtz resonators, simultaneous compressibility near-zero propagation at two independent frequencies can be obtained. Figure 5.28 shows the transmission coefficient of the proposed structure obtained from COMSOL simulation.

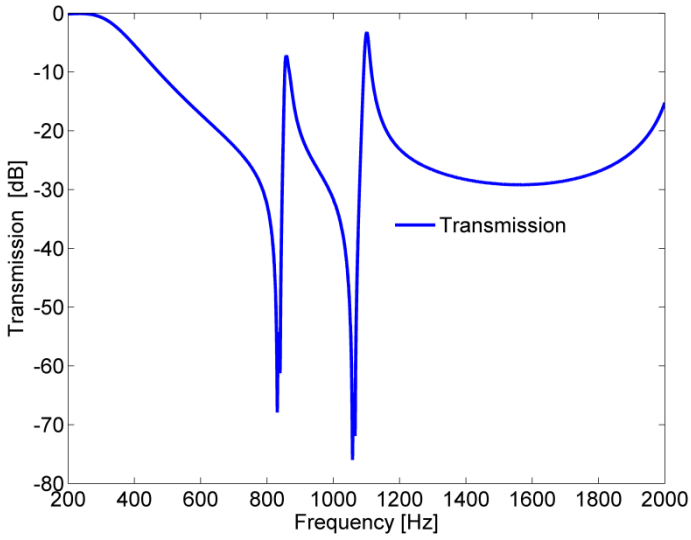

Figure 5.28 Simultaneous compressibility near-zero propagation at two independent frequencies.

The new unit cell produces two compressibility transmission peaks with transmission zeros on the left side. Transmission zeros are the results of negative values of the effective compressibility at the frequencies f_{r1} and f_{r2}.

5.5.3 Compressibility near-zero bandpass filter

Finally, to demonstrate the applicability of the near-zero concept, it will be shown that it is possible to simultaneously use both near-zero structures as building blocks to achieve a filtering function with a steep roll-off at both sides of the passband and with a small insertion loss. To illustrate this approach, a simple compressibility near-zero bandpass filter is designed, shown in Fig. 5.29. A CLC-LPF is used again as a host structure.

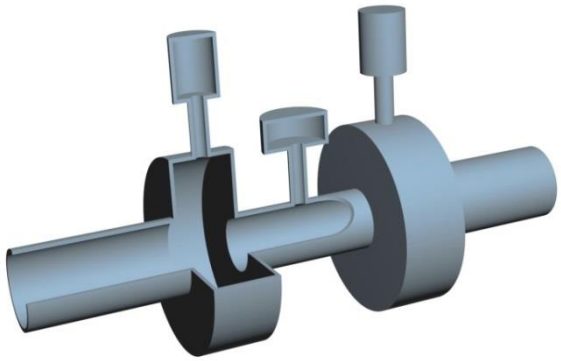

Figure 5.29 High-selectivity acoustic filter based on compressibility near-zero propagation

The third resonator, coupled to the inductive section of the lowpass filter, works at the first near-zero frequency f_{01}. The central frequency of the compressibility near-zero passband is determined by the dimensions of the outer resonators, while the dimensions of the inner resonator are fine-tuned to position the transmission zero on the right-hand side of the passband. Transmission and reflection coefficient are shown in Fig. 5.30. The central Helmholtz resonator has a cavity of Ø14.22x2.8 mm and a neck of Ø2x28 mm.

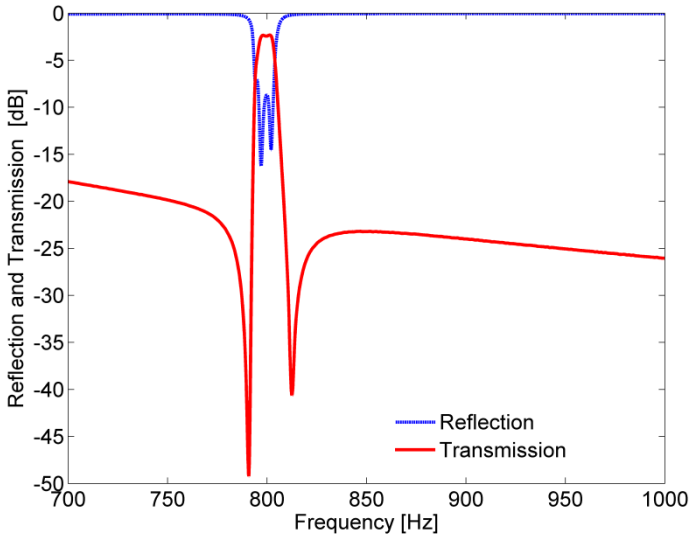

Figure 5.30 Transmission and reflection coefficients of the compressibility near-zero filter

The insertion loss is thus reduced to 2.3 dB while the fractional bandwidth, mainly determined by the slope of the effective compressibility function around the zero value, is equal to 1.2 %. Unlike left-handed structures, near-zero filters do not suffer from inherently large passband insertion losses. This is due to the fact that the imaginary part of the effective compressibility is relatively small around the CNZ frequency while it exhibits significantly larger values at frequencies where the real part of the effective compressibility is negative, i.e. at frequencies where left-handed acoustic devices operate, which results in large insertion losses.

6. Novel negative density resonant metamaterial unit cell and its applications

Negative values of effective mass density have so far been achieved using composites [29, 35-37], or exploiting the equivalence to the transmission-line-approach to metamaterials [39, 63, 103, 104]. In the latter case the frequency dependence of the effective density of unit cells exhibits the Drude behaviour, while no attempt has been made so far to design a unit cell with effective mass density of the Lorentzian type dispersion model. In electromagnetics the most well-known resonant type metamaterial unit cells are the split-ring-resonator (SRR) [18] and the complementary split-ring resonator (CSRR) [105, 106]. The acoustic equivalent of the CSRR, based on the analogy given in *Chapter* 2, is the Helmholtz resonator. On the other hand, the acoustic equivalent of the SRR, resonant type metamaterial unit cell with negative density, was unknown previous to this research.

6.1 Description and theoretical analysis of the novel unit cell

In the electromagnetic (EM) case, the most typical unit cell exhibiting Lorentzian-type permeability is the split-ring resonator (SRR). With the aim of obtaining a novel Lorentzian-type density acoustic unit cell, i.e. the acoustic counterpart of such an EM unit cell, we design its physical structure so as to match its lumped-element equivalent circuit to the one of the SRR-loaded microstrip, given in [107, 108] and shown in Fig. 6.1.

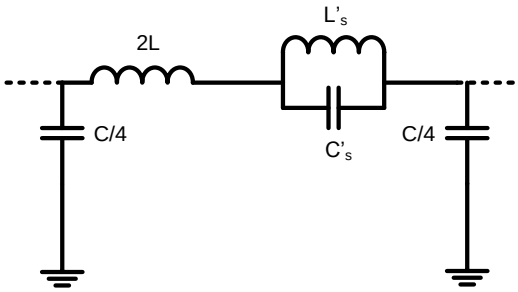

Figure 6.1 Lumped-element equivalent circuit of the SRR-loaded microstrip

Namely, in the EM case the equivalent circuit features a capacitor with both terminals at a potential other than ground. Such an element does not have a purely acoustic counterpart, but it can be introduced into the physical system as mechanical compliance. Following that line of reasoning, which relies on standard electromechanic and electroacoustic analogies, we propose that the corresponding acoustic unit cell is a thin elastic membrane placed in a short tube coaxial with an acoustic duct (acoustic split ring resonator – *aSRR*) [109], shown in Fig. 6.2 together with its equivalent circuit, which almost exactly matches that of the SRR-loaded microstrip.

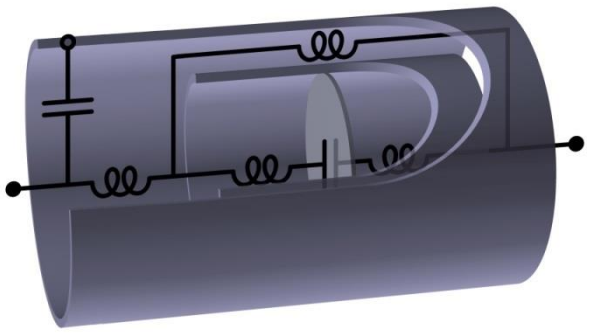

Figure 6.2 Layout and the equivalent electrical circuit of the proposed acoustic metamaterial unit cell

From the equivalent circuit we can see that it includes a series capacitance as was the case with the membrane type acoustic metamaterial unit cell described in *Chapter 3*. However, in this case there is another inductive branch which is connected in parallel with the series capacitance. This inductive line is very important in the realization of Lorentzian type dispersion, since without such a line the structure behaves as a high-pass filter, which blocks low frequency waves. It can be seen in other types of membrane based unit cells that they have a cut-off frequency, a so called "static limit" [110], and that their effective parameters have a Drude-like shape. The acoustic unit cell is not the exact counterpart of the electromagnetic unit cell, because in the capacitive branch we have an inductive section too. We cannot neglect inductances there because they model the mass of the membrane and the inertia of the air in the inner tube. However, the inductors connected in series with the capacitance can be absorbed into the outer inductance.

6.1.1 Analysis of the proposed unit cell

Figure 6.3 shows the cross section of the unit cell with its geometrical and physical parameters, where d is the length of the unit cell, M is the mass of the membrane, ρ is the density of the air, r and R are the radii of the inner and the outer tube respectively. It can be shown that the proposed unit cell indeed exhibits negative effective density at a particular range of frequencies.

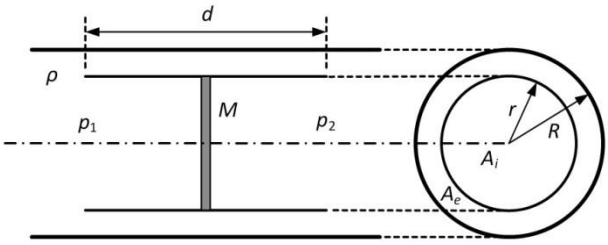

Figure 6.3 Cross section of the proposed acoustic metamaterial unit cell

In the external part of the acoustic duct (one that surrounds the tube), with cross section $A_e = (R^2 - r^2)\pi$, the total mass of the fluid is:

$$m_e = \rho_0 A_e d, \tag{6.1}$$

where d is the length of the tube. The external force acting on this mass is:

$$F_e = A_e(p_1 - p_2). \tag{6.2}$$

As d is significantly smaller than the wavelength, the previous expression corresponds to:

$$F_e = -A_e \frac{dp}{dz} d, \tag{6.3}$$

and Newton equation yields:

$$\rho_0 A_e d \frac{d^2 q_e}{dt^2} = -A_e \frac{dp}{dz} d, \tag{6.4}$$

where q_e is the displacement of the fluid particles in the external duct:

$$\rho_0 \frac{d^2 q_e}{dt^2} = -\frac{dp}{dz}. \tag{6.5}$$

On the other hand, the total mass in the tube (internal duct) with cross section $A_i = r^2\pi$ is:

$$m_i = \rho_0 A_i d + M, \tag{6.6}$$

where *M* is the mass of the membrane. Since the tube is short in comparison to the wavelength, the longitudinal displacement of the fluid particles varies linearly with z, and thus the average displacement of the membrane is equal to the average displacement of fluid particles in the tube. From the Hooke's law, under the linearity assumption, which holds when the membrane displacement q_i is small, we can obtain the total force acting on the total mass in the internal duct as:

$$F_i = A_i(p_1 - p_2) - 8\pi\tau q_i, \tag{6.7}$$

where τ is membrane tension. For the same reasons as above, the Newton equation gives:

$$(\rho_0 A_i d + M) \frac{d^2 q_i}{dt^2} = -A_i \frac{dp}{dz} d - 8\pi\tau q_i. \tag{6.8}$$

After division of both sides by $A_i d$ we obtain:

$$\rho_0 \left(1 + \frac{M}{\rho_0 A_i d}\right) \frac{d^2 q_i}{dt^2} = -\frac{dp}{dz} - \frac{8\pi\tau}{A_i d} q_i. \tag{6.9}$$

Under the assumption that the displacement is a harmonic function, $q_i = q_{i0} e^{-i\omega t}$, the relationship between the acceleration and displacement can be established as:

$$q_i = -\frac{1}{\omega^2} \frac{d^2 q_i}{dt^2}, \tag{6.10}$$

leading to:

$$\left(\rho' - \frac{8\pi\tau}{\omega^2 A_i d}\right) \frac{d^2 q_i}{dt^2} = -\frac{dp}{dz}, \tag{6.11}$$

where $\rho' = \rho_0 \left(1 + \frac{M}{\rho A_i d}\right)$ is the average density in the internal duct (that of the fluid loaded with the membrane).

The continuity equation at the edge of the unit cell yields:

$$A_e \frac{dq_e}{dt} + A_i \frac{dq_i}{dt} = (A_e + A_i) \frac{dq}{dt}, \tag{6.12}$$

where the right side denotes the total volume flow through the unit cell (both external and internal duct), with q denoting effective displacement corresponding to that volume flow. Another differentiation in time yields:

$$A_e \frac{d^2 q_e}{dt^2} + A_i \frac{d^2 q_i}{dt^2} = (A_e + A_i) \frac{d^2 q}{dt^2}. \tag{6.13}$$

Combining Eq. (6.13) with Eqs. (6.5) and (6.11), we obtain:

$$A_e \left(-\frac{1}{\rho_0} \frac{dp}{dz} \right) + A_i \frac{-\frac{dp}{dz}}{\left(\rho' - \frac{8\pi\tau}{\omega^2 A_i d} \right)} = (A_e + A_i) \frac{d^2 q}{dt^2}. \tag{6.14}$$

In any fluid effective density can be considered as the constant that defines the proportionality between gradient pressure force $-\frac{dp}{dz}$ and the acceleration of the fluid $\frac{d^2 q}{dt^2}$. While in regular fluids this constant is positive, which is the consequence of the fact that the direction of the acceleration and the force is the same, in metamaterials we can expect negative values of effective density at certain frequencies. Effective density as defined above can be easily obtained from the previous equation:

$$\rho_{\text{eff}} \stackrel{\text{def}}{=} \frac{-\frac{dp}{dz}}{\frac{d^2 q}{dt^2}} = \frac{A_e + A_i}{\frac{1}{\rho_0} A_e + \frac{1}{\left(\rho' - \frac{8\pi\tau}{\omega^2 A_i d} \right)} A_i}. \tag{6.15}$$

It can be noted that for very small values of A_e in relation to A_i (very thin external duct), this expression simplifies to:

$$\rho_{\text{eff}} = \rho' - \frac{8\pi\tau}{\omega^2 A_i d}, \tag{6.16}$$

which is the formula given in [39] for the effective density of a membrane in a (simple) hollow tube. It can be easily shown that the effective density as obtained above exhibits resonant behavior at the frequency:

$$f_r = \frac{1}{2\pi} \sqrt{\frac{8\pi\tau}{A_i d \left(\rho' + \frac{A_i}{A_e} \rho_0 \right)}} \tag{6.17}$$

and is equal to zero at the frequency:

$$f_0 = \frac{1}{2\pi} \sqrt{\frac{8\pi\tau}{A_i d \rho'}}. \tag{6.19}$$

The real part of the effective mass density obtained from Eq. (6.15) is plotted in Fig. 6.4. The following parameters of the aSRR have been used: $M = 88\ \mu\text{g}$, $d = 32\ \text{mm}$, $R = 8.1\ \text{mm}$, $r = 3\ \text{mm}$, $\tau = 5\ \text{N/m}$.

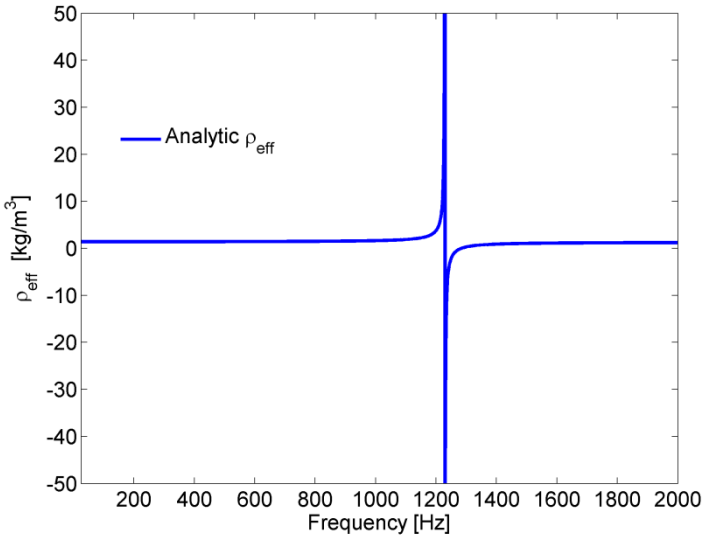

Figure 6.4 Effective density for a proposed unit cell (aSRR)

From figure 6.4 it can be concluded that the real part of mass density has a Lorentz-like shape, and that it has a negative value in a narrow frequency range. Furthermore, we can see that this type of unit cell has no cut-off frequency, i.e. the high wavelength waves can also pass.

6.2 Modeling the novel metamaterial unit cell

For the proposed unit cell two models were created. The first one is a FEM simulation model which was made in COMSOL Multiphysics simulator. The second one is a transmission line model which is based on electro-acoustical analogy and the circuit theory (ABCD matrix, matrix transformations etc.).

6.2.1 Finite element model in COMSOL Multiphysics

For modeling the proposed unit cell in COMSOL Multiphysics one special sub-module, the Acoustic-Structure interaction module, was used. The proposed unit cell is combination of acoustic and mechanical elements, which is why a simple pressure acoustic module was not sufficient for modeling. For simplifying the simulation and decreasing the simulation time a 2D axisymmetric model of the structure was created. The layout of the designed structure is shown in Fig. 6.5.

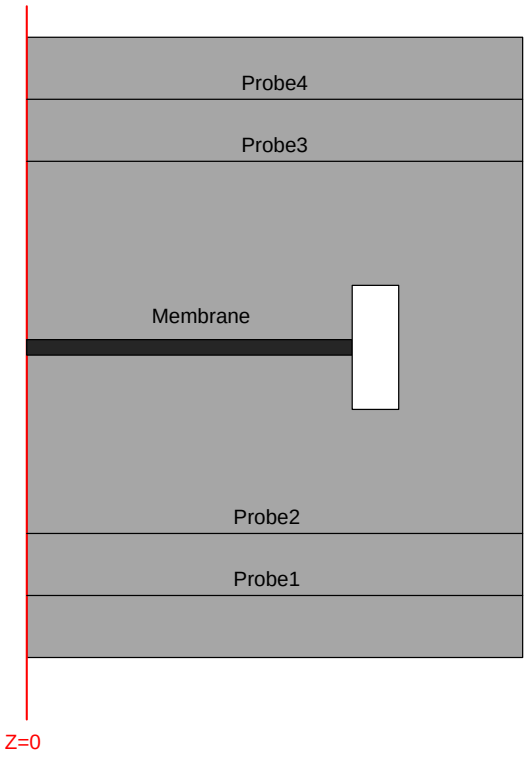

Figure 6.5 Layout of the structure in a 2D axisymmetric model

The unit cell was put in the long hollow cylindrical tube filled with air and the four probes were placed as described in *Chapter 4* (the extraction of the acoustic scattering matrix). The walls of the tube were modeled with hard-wall boundaries, which is the acoustic counterpart of a perfect electrical wall in electromagnetic simulators. The wall of the inner tube was also modeled with hard boundary condition. The membrane is a mechanical part of the cell, and it was modeled with linear elastic material model. Linear elastic material was characterized by its density (ρ_m), Young's modulus (E) and Poisson's coefficient (v). As material properties of the membrane we adopted values given for DuPont Kapton FPC. The characteristic values of the membrane were E= 2.758 GPa, ρ_m= 1420 kg/m^3, v= 0.34 and the thickness of the membrane was set to h= 22 μm. The membrane was connected to the wall and loaded with tension $\tau = 5$ N/m. Plane wave radiation was used as an acoustic source. The other end of the tube was closed by PML boundary to model the open end. Thermal and viscous losses have been modelled by the attenuation constant equal to 0.1 dB/m. Reflection and transmission coefficients in the frequency range from 1 kHz to 1.4 kHz are shown in Fig. 6.6.

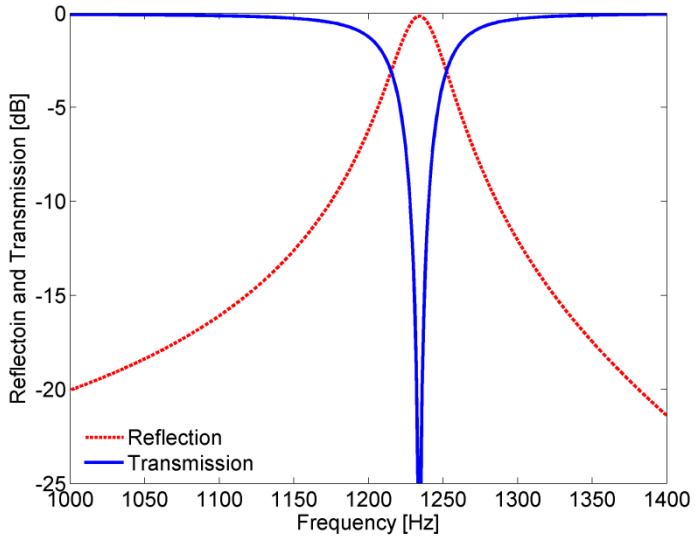

Figure 6.6 Reflection and transmission coefficients of the aSRR from FEM simulation

The results confirm that if a hollow duct with an otherwise allpass frequency response is loaded with such a unit cell, a notch in the frequency response at the resonant frequency can be observed. Namely, around f_r the structure behaves as a single-negative medium and does not support propagating modes.

The real part of the effective mass density obtained from Eq. (6.15) is plotted in Fig. 6.7, and compared to the same parameter extracted from FEM simulations in COMSOL Multiphysics using the approach described in *Chapter 4*.

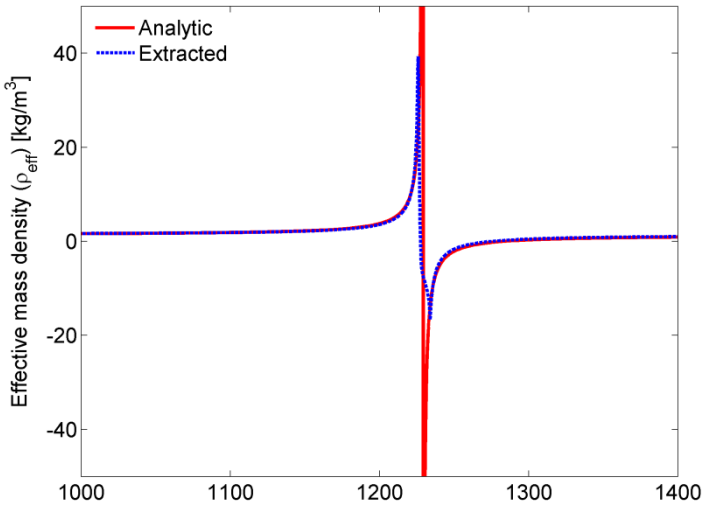

Figure 6.7 Comparison of the effective mass density of the proposed unit cell obtained from the analytical expression and from FEM simulations

A very good agreement between the calculated and extracted effective mass density can be observed, with a difference in the magnitude due to the fact that the analytical expression refers to the lossless case.

6.2.1 Transmission line model

It should be noted that this unit cell is more complicated than the CNZ structure, whose transmission line model was described in the previous section. In the middle of the unit cell there is a mechanical element (membrane), which cannot be modeled as a simple acoustic transmission line section. All other sections were modeled as transmission line sections with series acoustic impedances and shunt acoustic admittances and characterized by ABCD matrices, while the membrane was modeled as acoustic impedance. The block diagram representing the model of the novel metamaterial unit cell is shown in Fig. 6.8.

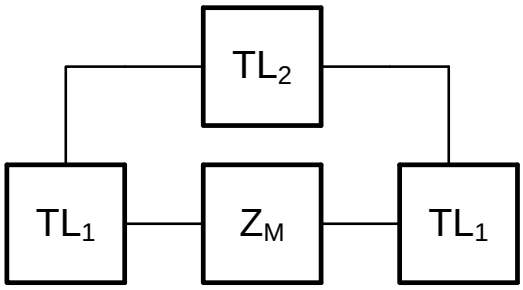

Figure 6.8 Block diagram of the aSRR

The structure consists of four blocks which are connected as shown in Fig. 6.8. Three of these four blocks can be modeled with acoustic transmission line model (ABCD matrix) following the method from *Chapter 4*, while the fourth one is the mechanical element (Z_M). The TL_1 block is the ABCD matrix for the half-length inner inductive tube in the unit cell (Fig. 6.2), having in mind that the membrane is placed in the middle of the inner inductive tube section. The TL_2 block is the ABCD matrix for the outer inductive section. Calculated values of the unit length acoustic series inductance and the acoustic shunt capacitance for the inner and outer tube sections are given in Table 6.1.

TABLE 6.1 SERIES INDUCTANCE AND SHUNT CAPACITANCE VALUES

Elements	Unit length acoustic series inductance [kg/m^5]	Unit length acoustic shunt capacitance [m^2/Pa]
Inner inductive sectionTL_1	$4.421 \cdot 10^4$	$1.9567 \cdot 10^{-10}$
Outer inductive section TL_2	$7.1051 \cdot 10^3$	$1.2175 \cdot 10^{-9}$

The membrane was modeled as a thin plate described by the transverse displacement which satisfies the flexural wave equation. [63, 111, 112, 113]. The mechanical impedance for a thin plate from [113] is

$$Z_M = -j\omega m \frac{\mathrm{I}_1(k_m r)J_0(k_m r) + \mathrm{J}_1(k_m r)\mathrm{I}_0(k_m r)}{\mathrm{I}_1(k_m r)\mathrm{J}_2(k_m r) - \mathrm{J}_1(k_m a)\mathrm{I}_2(k_m r)} \tag{6.20}$$

where r is the radius of the membrane, J_n and I_n are the regular and modified *n-th* ordered Bessel's functions, m is membrane mass, and k_m is the flexural wavenumber, which can be calculated as:

$$k_m^2 = \omega \sqrt{\frac{\rho_m''}{D}}, \tag{6.21}$$

where D is flexural rigidity, given by:

$$D = \frac{Eh^3}{12(1-v^2)}, \tag{6.22}$$

where E is the Young's modulus, v is the Poisson's coefficient and h is the thickness of the membrane. The term ρ_m'' represents surface mass density, defined as $\rho_m'' = \rho_m h$. From mechanical impedance the acoustic impedance can be calculated as:

$$Z_{am} = \frac{Z_M}{S^2} \tag{6.23}$$

where S is the cross-section area of the membrane. Using the transmission line theory the series connected acoustic impedance was transformed to a corresponding ABCD matrix and the whole system was transformed to its equivalent ABCD matrix. After the transformation the equivalent ABCD matrix for the whole system was calculated in the frequency range from 200Hz to 2 kHz and transformed to the final acoustic scattering matrix. The inlet and outlet duct were included into the system through the acoustic characteristic impedance $Z_0 = 2 \cdot 10^6$ [Pa·m^{-3}] in the transformation of the equivalent ABCD matrix to S matrix. *Matlab* code for transmission line modeling of the new metamaterial unit cell is given in *Appendix A5*. In this simulation model the same dimensions and parameters were used as in the FEM simulation model. The frequency response (reflection and transmission coefficients) of the aSRR from the transmission line model when all losses (thermal and viscous) are included is shown in Fig. 6.9.

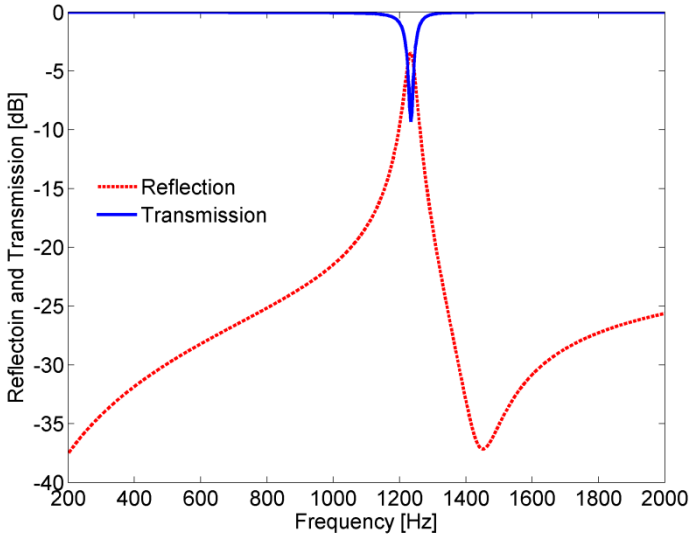

Figure 6.9 Reflection and transmission coefficients of the aSRR from the transmission line model

The response is same as in the case of the FEM simulation model. Figure 6.10 shows a comparison of transmission coefficients obtained from both simulation models.

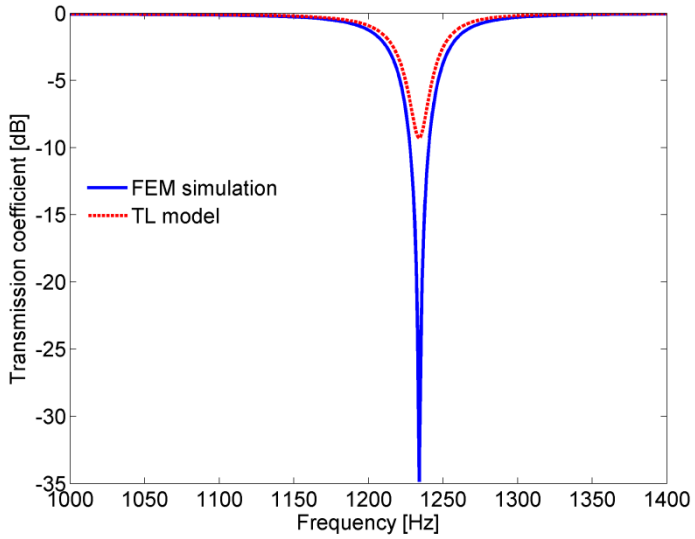

Figure 6.10 Comparison of the transmission coefficient the proposed unit cell obtained from the FEM simulation and from the transmission line model

The transmission characteristic exhibits a notch in a the narrow frequency range where the density is less than zero, the medium is single negative and thus propagation is not allowed. Figure 6.11 shows the extracted effective density from both models compared with the analytical expression for the effective density, given by Eq. (6.15).

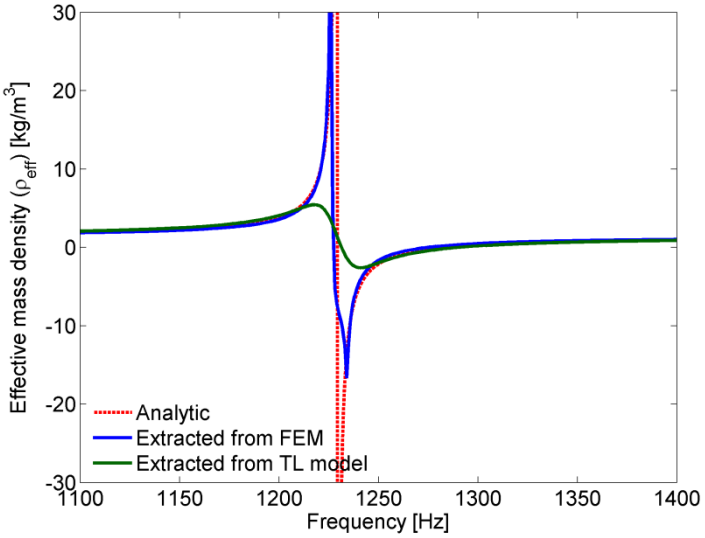

Figure 6.11 Comparison of the effective mass density of the proposed unit cell obtained from the analytical expression, from FEM and from the transmission line model

A very good agreement between the calculated and extracted effective mass density can be observed.

6.3 Applications of the novel unit cell

6.3.1 Bandstop (single negative) acoustic medium

To illustrate the versatility of the proposed unit cell, we first use it to design an evanescent bandstop acoustic medium. This structure is designed by cascading unit cells loading the host duct, as shown in Fig. 6.12.

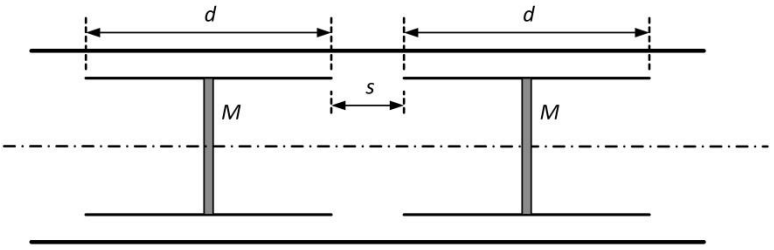

Figure 6.12 Acoustic bandstop medium (for convenience, only two unit cells are shown).

The bandwidth of such a medium can be controlled by conventional filter design methods, i.e. by varying the number of unit cells used and by tuning their mutual coupling. The medium composed of four unit cells positioned at distances equal to $s = 2$ mm, analysed in Fig. 6.13, exhibits stopband attenuation of more than 30 dB and a very steep roll-off. Such properties are quite desirable from the point of view of practical application in any system with a need for low radiated sound power at a particular frequency range.

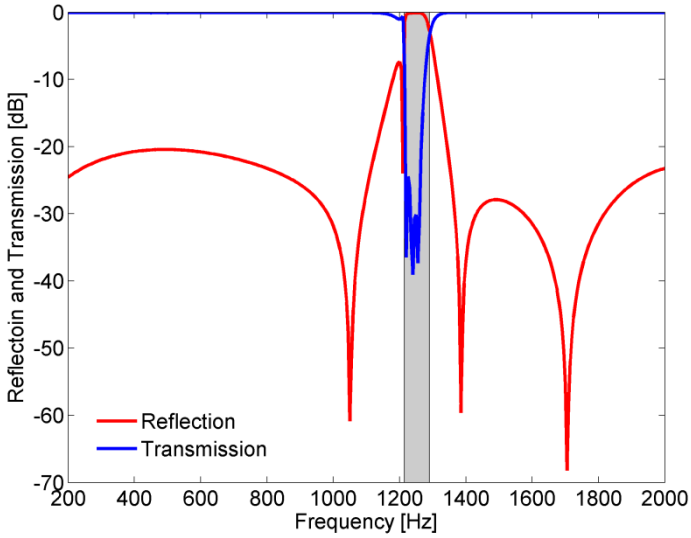

Figure 6.13 Simulated response of the acoustic bandstop medium

6.3.2 Dual aSRR

A modified version of aSRR is shown in Fig. 6.14. This modified unit cell is capable of operating at two independent frequencies, which are determined by individual sets of geometrical parameters of the structure and thus can be separately engineered.

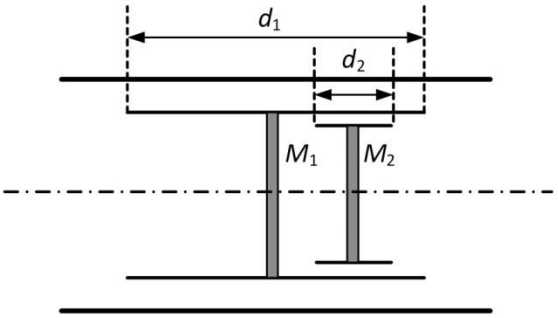

Figure 6.14 Modified (dual) aSRR

The modified unit cell produces negative effective mass density at the two different frequencies. The real and the imaginary part of the extracted effective density is shown in Fig. 6.15.

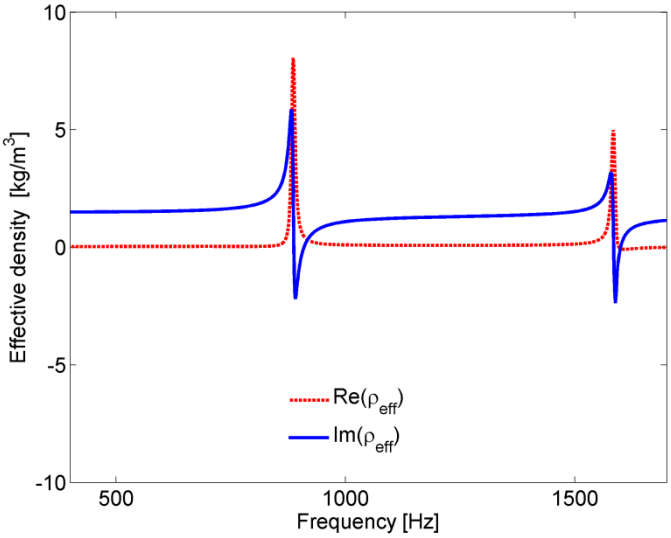

Figure6.15 Extracted effective density for a dual aSRR

The effective density is negative at two independent frequency ranges and in both cases it exhibits a Lorentzian shape. The independent resonant frequency control is illustrated in figure 6.16 where the first and the second resonant frequency are independently tuned only by modifying the diameter of the corresponding duct, namely by changing r_1 or r_2. It should be noted that the dimensions of the two inner ducts can be independently modified without affecting the rest of the structure as long as the modifications are relatively small. On the other hand, if the change in either r_1 or r_2 is significant, the other of the two parameters (and possibly *R* as well) would also have to be modified to account for the changes in the acoustic inductances due to modified widths of air channels in the system.

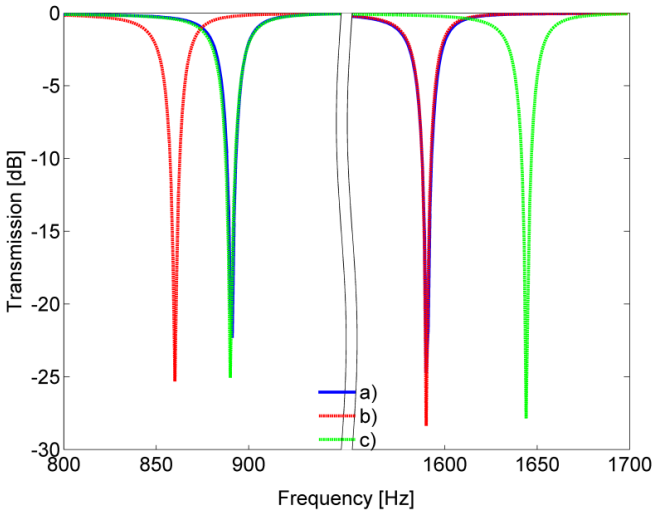

Figure 6.16 Independent control of operating frequencies is obtained by varying the diameters of inner acoustic ducts: $r_{1a} = r_{1c} = 3.2\ mm,\ \ r_{2a} = r_{2b} = 2.8\ mm,\ \ r_{1b} = 3.3\ mm\ , r_{2c} = 2.7\ mm.$

As three different scenarios are considered here, a), b) and c), there are three combinations of the mass values, because both M_1 and M_2 depend on the radii of the corresponding tubes, which are different for each of the scenarios. The mass per unit area of both membranes is equal to $m' = 3.124 \cdot 10^{-2}$ kg/m^2, from which the masses M_1 and M_2 can be easily calculated and in each case ($M_x = m' r_x^2 \pi$). By using a similar approach to the one presented above, a dual-band bandstop acoustic medium can be designed by loading the hollow duct with thus modified dual-band unit cells. Dimensions of the designed dual-band structure are equal to those used in case a above and $d_2 =$ 6 mm. Two dual-band unit cells were used and positioned at a distance of $s = 2$ mm. The mass of both membranes per unit area is $3.124 \cdot 10^{-2}$ kg/m^2. The simulated frequency response of such a medium composed of two unit cells is shown in Fig. 6.17 and the extracted effective mass density of the dual-band unit cell is shown in the inset.

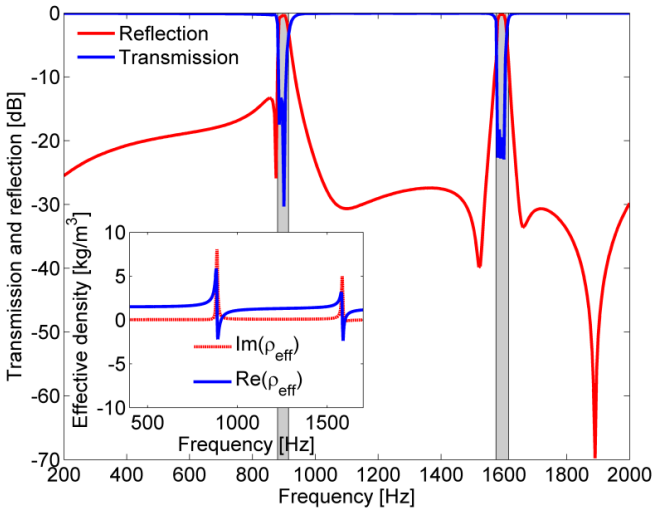

Figure 6.17 Simulated response of the acoustic dual-band bandstop medium and the extracted effective parameters (inset)

Even though composed of only two unit cells, the medium exhibits high selectivity, stopband attenuation of around 20 dB and 10dB-fractional bandwidths of 3% and 2%, respectively.

6.3.3 Double negative acoustic band-pass filter

The new unit cell (aSRR) can be used to design a novel acoustic double negative metamaterial. Namely, by combining aSRR with another structure capable of providing negative effective compressibility (negative bulk modulus) in the same frequency range, real but negative values of the wavenumber can be achieved, resulting in negative phase velocity i.e. in double negative propagation. In Fig. 6.18 a novel acoustic double negative metamaterial is shown, where side holes on an acoustic duct are used to realize negative effective compressibility of the Drude type [6.7], together with aSRRs which provide negative mass density of the Lorentz type.

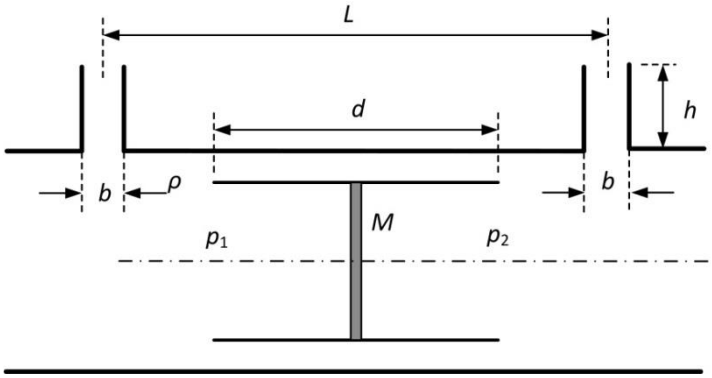

Figure 6.18 Double negative acoustic metamaterial

Dimensions of the designed structure are equal to those used previously and the side hole dimensions are $b = 5$ mm, $h = 48.95$ mm, $L = 34$ mm. The extracted effective parameters and the wavenumber of the double negative metamaterial are shown in Fig. 6.19.

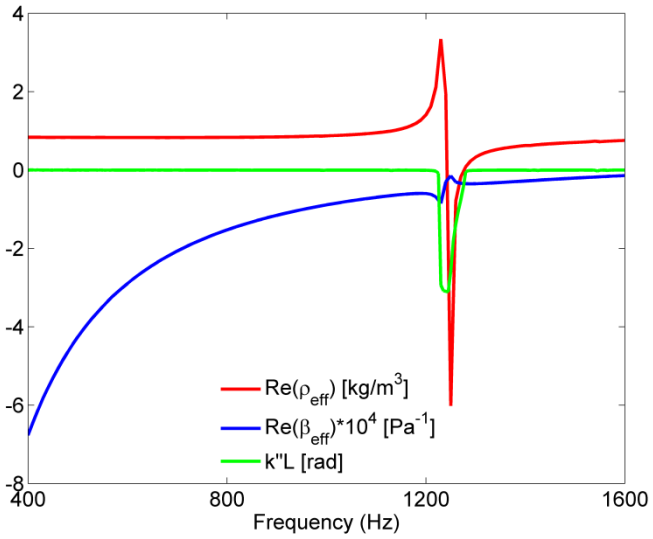

Figure 6.19 Extracted effective parameters and wavenumber of the double negative metamaterial

In the frequency range where both parameters are negative a new passband occurs, as shown in

Fig. 6.20. The passband is characterized by negative values of wavenumber k'', which proves that the propagation is indeed double negative.

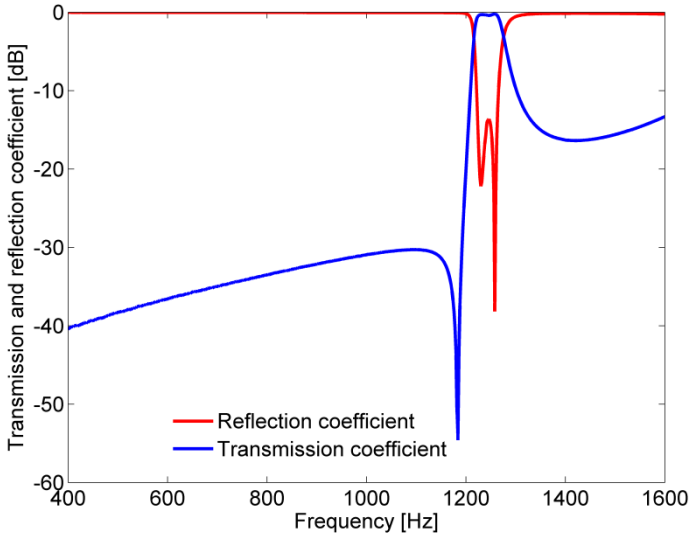

Figure 6.20 Reflection and transmission coefficients of the double negative acoustic metamaterial

6.3.4 Density near-zero metamaterial using aSRR

In this section will be shown that the proposed unit cell, with an appropriate choice of host medium, can be used to achieve near zero (NZ) acoustic wave propagation at the frequency where its effective density, given by Eq. (15), is equal to zero [114]. The values of the parameters used in both approaches were: $M = 0.88$ mg, $d = 18$ mm, $R = 4$ mm, $r = 3$ mm, $\tau = 5$ N/m, and the resulting resonant frequency was $f_r = 1175$ Hz. Fig. 6.21 shows the comparison between the effective density obtained from Eq. (15) and the same parameter obtained from TL model and FEM simulation. A good match between the results obtained from analytical expression, the model and the simulation can be seen.

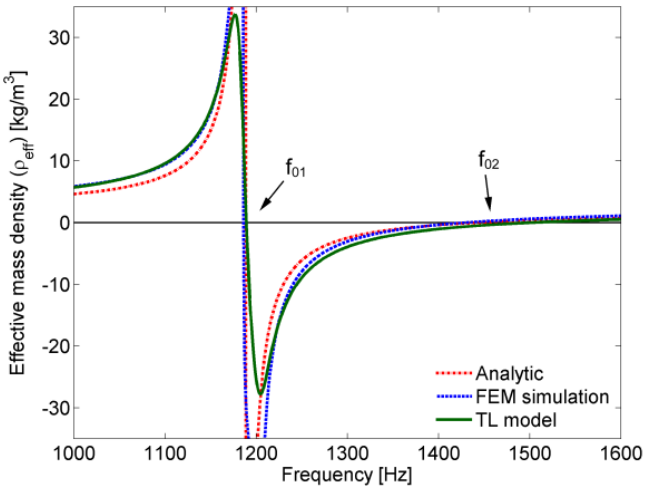

Figure 6.21 Effective mass density of the aSRR obtained from the analytical expression, TL model and FEM simulation

Effective density as a function of frequency exhibits resonant behaviour, and there are two frequencies, $f_{01} < f_r$ and $f_{02} > f_r$, at which its value is equal to zero. aSRR exhibits a notch around f_r, i.e., that the structure behaves as a single-negative metamaterial. For that reason, near-zero propagation at f_{01} is characterized by very high attenuation. At f_{02} attenuation is significantly lower, but the near-zero character of the propagation at f_{02} is not obvious because it is not easily distinguishable from conventional propagation at frequencies immediately above. It can be concluded that, for the purpose of clearly demonstrating near-zero propagation, an all-pass acoustic duct is not a convenient host medium. A convenient host should exhibit a stopband at the frequency range of interest and it should not support double negative (left-handed) wave propagation. In this specific case, where effective density can have both positive and negative values, this implies that the effective compressibility β_{eff} should be strictly positive. An example of such a host is a simple acoustic low-pass filter, either CLC or LCL, provided that the aSRR operates above its cut-off frequency. In order to demonstrate density near zero (DNZ) wave propagation we opted for a CLC filter as a host and loaded its inductive section with one aSRR, as shown in Fig. 6.22a (not to scale).

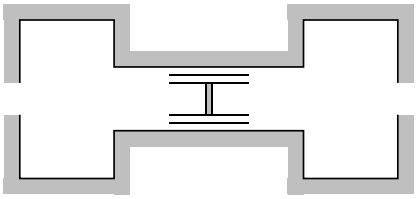

a)

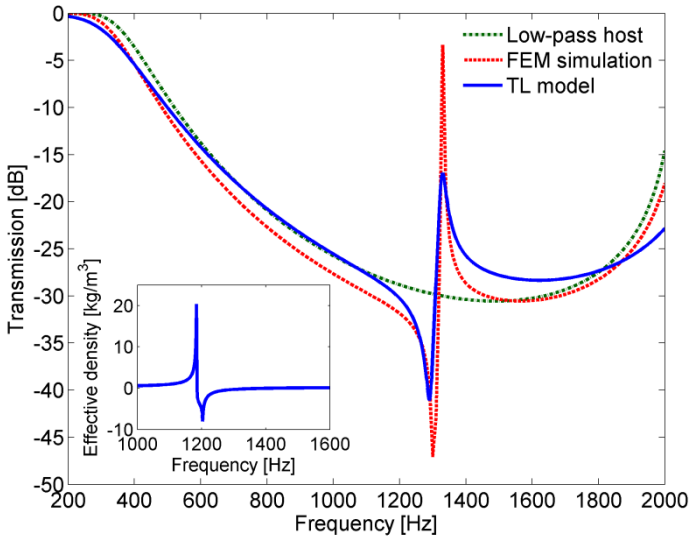

b)

Figure 6.22 Low-pass acoustic CLC filter (C sections ∅52×20 mm, L section ∅10×80 mm) loaded with one aSRR in the L section (a) Layout (b) Frequency response obtained through TL model and FEM simulation

A TL model was created, analogous to the one described in the previous section, and a corresponding FEM simulation was also carried out in COMSOL Multiphysics. The resulting transmission coefficient is shown in Fig. 6.22b, where a very good match between the TL model and

FEM simulation can be seen. The dotted green line indicates the frequency response of the host low-pass filter. The transmission peak in the stopband of the host corresponds to one of the frequencies where effective density is equal to zero, namely to f_{02}. The frequency response exhibits a transmission zero as well, and its frequency corresponds to the notch in the frequency response of the aSRR itself. It should be noted that in this case the frequency of the transmission peak is higher than the frequency of the transmission zero. It is also possible to demonstrate DNZ wave propagation by loading each of the two capacitive sections of the CLC host with an aSRR, as shown in Fig. 6.23a. A transmission peak and a transmission zero appear in the stopband of the host filter again, their frequencies corresponding to the zero value of the effective density and to the notch in the frequency response of the aSRR, respectively. However, in this case, the frequency of the transmission peak corresponds to f_{01}, and it is lower than the frequency of the transmission zero, as shown in Fig. 6.23b.

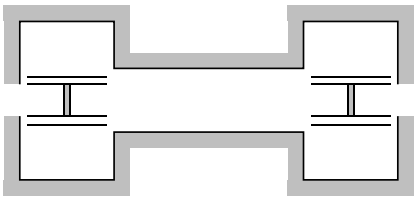

a)

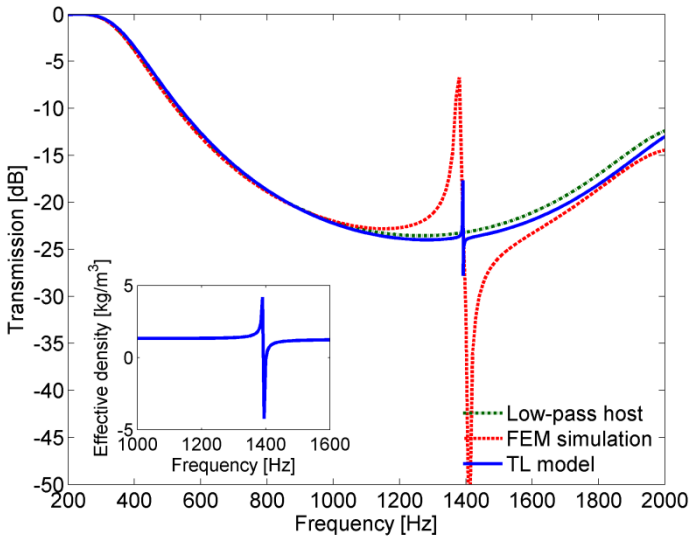

b)

Figure 6.23 Low-pass acoustic CLC filter loaded with two aSRR's in its capacitive sections (a) Layout (b) Frequency response

It should be noted that in case the unit cell is placed in a host structure, its effective density changes because the space between the unit cell and the wall of the host acts like an additional external duct. This includes an additional parallel inductance in the equivalent circuit, and eventually results in a shift of the resonant frequency of the aSRR, visible in both Figs. 6.22b and 6.23b. The shift in the case of the CLC host is more noticeable because the inductance of the additional external duct is significantly smaller than the inductance of the actual external duct of the aSRR. It can also be

shown that the situation does not change significantly if both inductive sections of an LCL low-pass host or just the single inductive section of a CLC low-pass host are loaded with an aSRR. Whether the transmission peak will be at a higher frequency than the transmission zero or vice versa depends only on whether the aSRR is located in the inductive or the capacitive section of the host filter.

6.3.4.1 Multiband density near-zero propagation

Previous research suggests that the mechanisms for reducing insertion loss, increasing the fractional bandwidth or achieving multiband propagation can be easily extended to the case of DNZ propagation as well. For example, a dual band aSRR, shown in Fig. 6.14, has been shown to be exhibit zero density at two independently engineered frequencies, and if placed in an otherwise all-pass acoustic duct, two notches in the frequency response can be observed. Here we show that the same unit cell can support simultaneous near zero propagation at two frequencies if placed in a convenient host, such as the L section of the CLC filter used in the previous simulations. To that aim, a FEM simulation was carried out, with results shown in Fig. 6.24, and it can be seen that two narrow passbands emerge in the stopband of the host. The dimensions used in the simulation were $R = 5$ mm, $r_1 = 3.2$ mm, $r_2 = 3$ mm, $d_1 = 32$ mm, $d_2 = 4$ mm, $M_1 = 1$ mg and $M_2 = 0.88$ mg, setting the two near-zero frequencies at $f_1 = 856$ Hz and $f_2 = 1566$ Hz. At these two frequencies the effective density is equal to zero, as shown in the inset of Fig. 6.24, which confirms the NZ character of acoustic wave propagation.

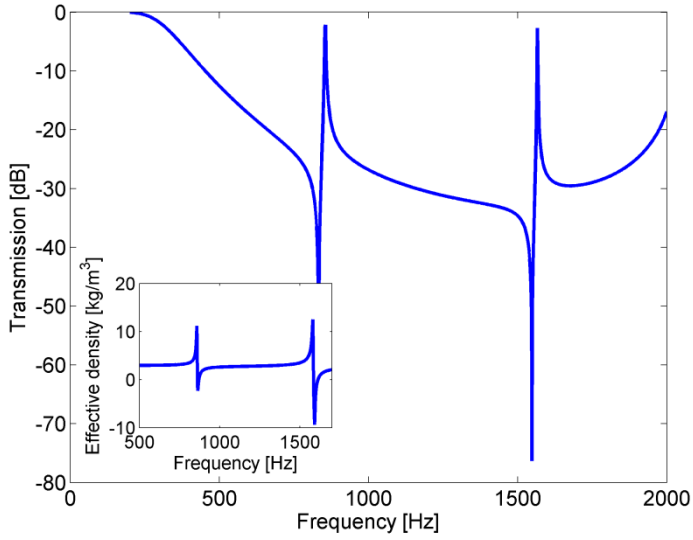

Figure 6.24 Near-zero wave propagation at two independently chosen frequencies, obtained by loading the inductive section of a CLC host with a dual-band aSRR

6.3.4.2 Near zero bandpass filtering

The versatility of the acoustic split ring resonator will be illustrated with an example of its use in NZ bandpass filtering. Namely, it has been shown that in case aSRR is located in the inductive section of the host filter, the transmission peak is at a higher frequency than the transmission zero, while in case it is located in the capacitive section of the host filter, the opposite holds. Let us suppose that all three

sections of a CLC host are loaded with one aSRR each, as shown in Fig. 6.25a, but that the dimensions of the aSRR's are slightly different, chosen so as to set their transmission peaks at the same frequency.

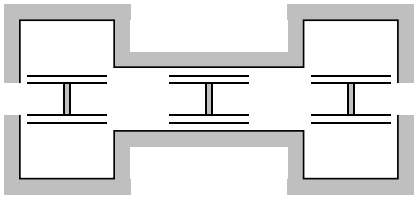

a)

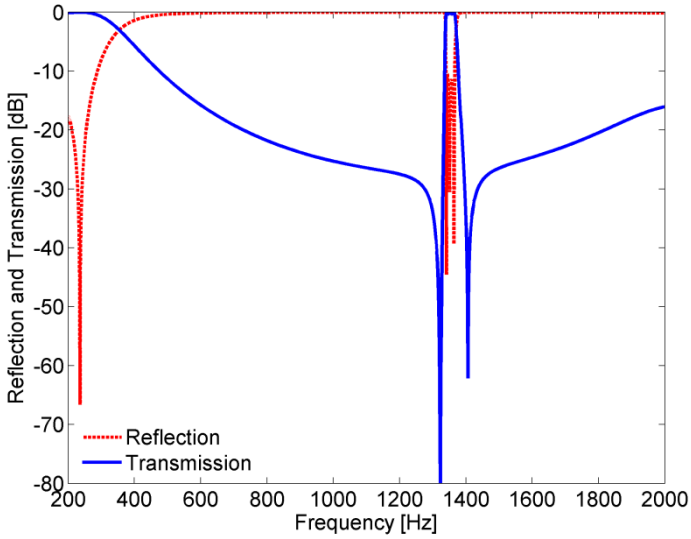

b)

Figure 6.25 Near-zero bandpass filter (a) Layout (dimensions are the same as in the previous case except for $d_1 = 18.95$ mm for the aSRR in the inductive section of the host, and $d_2 = 17.4$ mm for the aSRR in its capacitive sections) (b) Frequency response (FEM simulation)

The aSRR in the inductive section is expected to introduce a transmission zero at a frequency immediately below the transmission peak, while the aSRR's in the capacitive sections are expected to introduce transmission zeros at a frequency immediately above. The frequency response of the entire structure will thus correspond to a bandpass filter with very small fractional bandwidth and a steep roll-off. This expectation has been confirmed by a FEM simulation, whose results are shown in Fig. 6.25b. The bandwidth of the obtained filter is equal to 30 Hz (corresponding to a fractional bandwidth of 2.4%), while the insertion loss is as low as 0.2 dB. It should be noted that, unlike left-handed structures, NZ filters do not suffer from inherently high passband insertion losses.

7. Acoustic surface waves on grooved surfaces

In recent research in the field of materials science there have been attempts to identify the acoustic analogy of surface electromagnetic waves, particularly surface plasmon polaritons, which occur on boundaries between highly conductive and dielectric media [115-121]. The principal difficulty in this general case is the apparent nonexistence of an acoustic analogy of metals. However, in the case of spoof plasmons [122-130], electromagnetic surface modes observed on highly conducting grooved surfaces, a corresponding acoustic phenomenon exists and it is an acoustic surface wave propagating at the boundary between a fluid and a hard grooved surface [131-133]. The understanding of this analogy has given rise to new research in the field of controlling the behavior of surface acoustic waves by tailoring the period, the width and the depth of the grooves. It has been shown that by varying the geometry of the grooves in this way, the wave number of the propagating surface wave can be made different from its initial value k_0, even infinitely large [134-136]. This has led to a number of applications such as sound trapping, where a gradient change of the surface texture has been introduced to slow down and finally stop the surface wave at a desired position along the structure [134-136], collimation of sound [137-139], or acoustic lensing, where it has been used to tailor the phase pattern of the surface wave [140].

7.1 Introduction

There are many different types of acoustic surface waves depending on the nature of the two media forming the interface (solid–solid, solid–fluid, fluid–fluid and so on) [141]. Here we will focus on acoustic surface waves appearing on a fluid–fluid interface. The condition for the existence of an acoustic surface wave propagating at the interface between two semi-infinite fluids is very similar to the equation (Eq. 7.1) governing the presence of a surface electromagnetic mode running along the interface between two dielectric media [137]:

$$\frac{k_z^I}{\rho^I} + \frac{k_z^{II}}{\rho^{II}} = 0 \tag{7.1}$$

where k^{I}_z and k^{II}_z are the inverses of the decay lengths of the acoustic surface wave in media I and II, respectively, and ρ^{I} and ρ^{II} are the corresponding mass densities. The mass density plays the same role as the dielectric constant in the electromagnetic case. It is clear that if the two media have positive mass densities, there is no acoustic surface wave propagation at the I–II interface [137]. One possibility for generating acoustic surface waves is to place a fluid layer of uniform thickness on top of a semi-infinite fluid. Here, we consider a similar alternative, in which acoustic surface waves are created by periodically corrugating the interface between a rigid body and a fluid. The simplest way of doing this is by perforating a one-dimensional (1D) array of grooves. A rectangular-groove grating is presented in Fig. 7.1, with a surface wave propagating in direction *x*, parallel to the surface of the structure, in air.

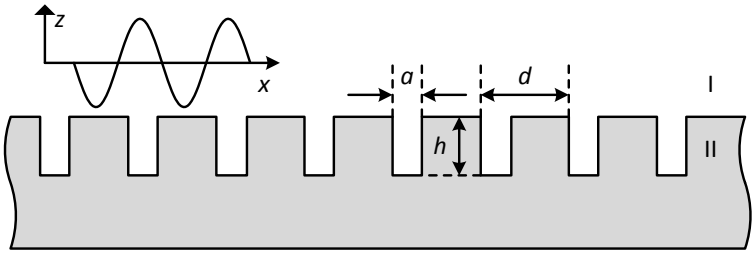

Figure 7.1 A typical grooved surface which supports propagation of acoustic surface waves.

The wave is purely evanescent in the direction *z* perpendicular to the surface. The reflection of acoustic waves, and the behavior of surface waves, can be described by the same formalism as for the transverse magnetic (TM) waves. The equations that describe the acoustic field and a TM field if the structure is perfectly conducting are the same, provided the right equivalent quantities are substituted. The magnetic field has a single component H_y different from zero, and is perpendicular to the incidence plane *xz* of Fig. 7.1. The electric field lies in the *xz* plane [131]. The fluid in region II of thickness *h* can be characterized effectively by a mass density that is different to the one associated with the fluid in semi-infinite medium I. In other words, we could say that medium II is an acoustic metamaterial. In the case of a grooved perfect rigid body, the dispersion relation (relation between frequency, ω, and wavenumber, *k*) of these geometry-induced acoustic surface waves is controlled by the geometrical parameters of the array of grooves and the density of the fluid. When the width of the grooves, *a*, is much smaller than the period of the array, *d*, a good approximation for $k(\omega)$ is given by [131, 137]:

$$k_x = k_0 \sqrt{1 + \left(\frac{a}{d}\right)^2 (\tan k_0 h)^2} \tag{7.2}$$

where $k_0 = \omega/c_S$, with c_S being the velocity of sound in medium I. Figure 7.2 shows the dispersion relation of the acoustic waves in air (blue line) and dispersion relation of the acoustic surface waves when the fluid medium I is air and the geometrical parameters are, d = 5 mm, a = 1 mm and h = 24 mm (red line).

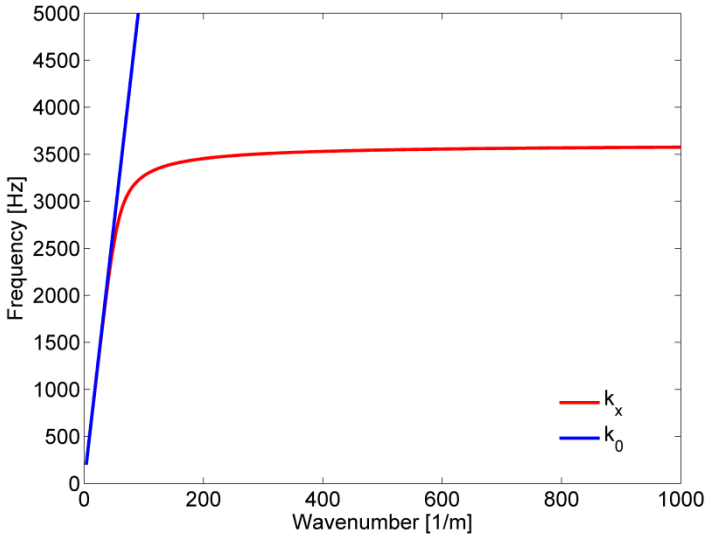

Figure 7.2 Dispersion diagram of the acoustic surface wave on grooved surface

In Fig. 7.2 it can be seen that the wavenumber for lower frequencies of the surface waves is similar to the wavenumber in the air. At higher frequencies the wavenumber start to increase and at a certain frequency it goes to infinity. This frequency is like the resonance frequency in the surface plasmon polariton (SPP) in optics. The acoustic "plasma" frequency f_{ap}, where the wavenumber reaches infinity, depends on the geometrical parameters of the grooved surface and can be calculated as,

$$f_{ap} = \frac{c_0}{4h} \tag{7.3}$$

where c_0 is the speed of sound in the medium I and h is the depth of the grooves. For frequencies above f_{ap} the surface wave propagation is not possible.

7.2 Applications

Owing to their strong dispersion nature, acoustic surface waves on grooved surfaces can be used in many applications such a acoustic wave trapping, extraordinary transmission etc.

7.2.1 Slowing down acoustic surface waves on a grooved surface

Slowing down optical waves with resonating photonic structures introduces controllable optical delays and allows temporary storages of light such as all-optical memories and switches [135]. Acoustic surface wave propagation along a periodically grooved rigid surface surrounded by air can be engineered with their propagation properties controlled by geometrical means. These highly localized acoustic surface waves give rise to strong acoustical field confinement along the grooved rigid surface, whereas the slowing down of sound can eventually reduce the group velocity to zero [134]. In [135] a metamaterial was designed, consisting of an array of grooves with constant

periodicity and graded depths perforated on a rigid plate, as shown in Fig. 7.3, to control the acoustic propagation.

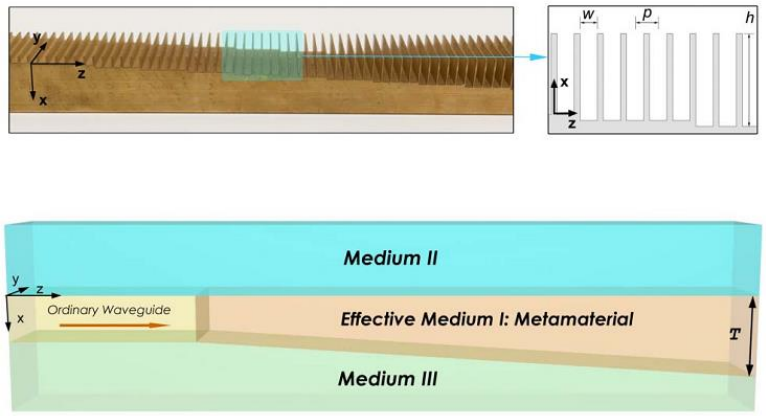

Figure 7.3 Metamaterial with graded depths perforated on a rigid plate and the effective medium model of the composite structure. (From [135])

The acoustic dispersion relation on this graded structure was analyzed by the effective medium model. The group velocity of the acoustic surface wave can be calculated from the Eq. 7.2 and it is equal to:

$$v_g = \frac{c_0}{\sqrt{1+\frac{k_0}{k_x}(\tan k_0 h)^2} + k_0 h \left(\frac{k_0}{k_x}\right) \frac{(\tan(k_0 h))^2+1}{\sqrt{(\cot(k_0 h))^2+\frac{k_0}{k_x}}}} \tag{7.4}$$

where c_0 is the sound speed in the air, k_0 is the wavenumber in the air, h is the depth of the grooves and k_x the surface wave number calculated from the dispersion relation (Eq. 7.2). Graded acoustic artificial structures can control not only the propagation direction of the wave but also the spatial distribution of the energy. Figure 7.4 shows the group velocity along the graded metamaterial normalized with respect to the speed of sound in the air.

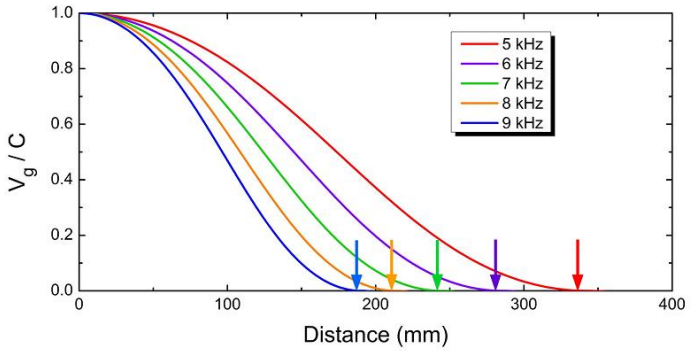

Figure 7.4 Calculated group velocities of acoustic waves (normalized to the sound speed in air). (From [135])

From Fig. 7.4 it can be seen that the surface acoustic wave slowed down and stopped. Also it can be noted that different frequencies stop at different locations. With a decrease in group velocity the wavelength of the surface wave also decreases. In Fig. 7.5 it is shown how the wavelength

changes depending on the depth of the grooves at a constant frequency (d= 5 *mm*, a= 1 *mm*, f=3.4 *kHz*).

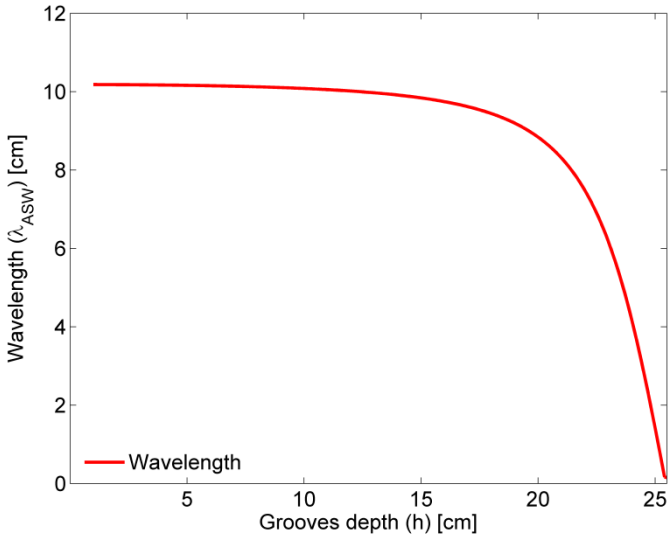

Figure 7.5 Dependence of the wavelength of the acoustic surface wave on the depth of the grooves at a constant frequency

When the gradual change in the groove depth is linear (with a constant angle Θ) the stop position z can be calculated as [135]

$$z = \frac{c_0}{4\theta f} \tag{7.5}$$

as the effective wavelength of acoustic wave is progressively decreased. Therefore these unit cells are no longer subwavelength in size, which leads to the breakdown of effective medium model, and to a deviation in predicting where exactly the acoustic wave will be trapped and how its intensity will be distributed around the stop position [135]. Experimental results for the sound intensity distribution on the surface from [135] are shown in Fig. 7.6. It can be seen that different frequencies slow down and stop at different positions. The stop positions depend on the frequency and also from the angle of the linear change in the depth of the grooves.

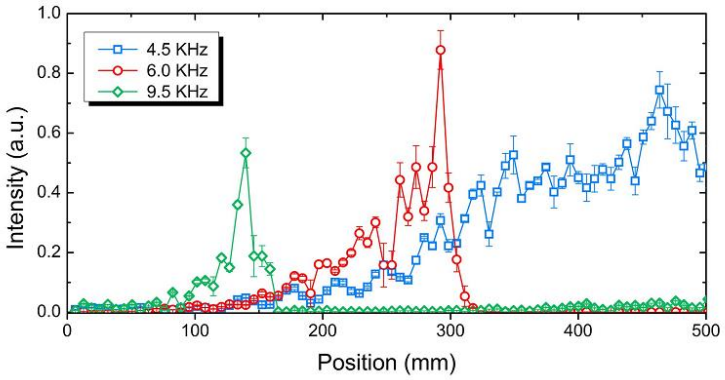

Figure 7.6 Experimental results of acoustic field intensity variation along the metamaterial. (From [135])

The same phenomena can be realized by linearly changing another geometrical surface parameter instead of the depth, for example the width of the grooves can also be changed, as shown in [136]. Furthermore, the shape of the graded surface does not have to be a plate in order to realize spatial frequency separation, it can be e.g. a cylindrical rod with gradually changing geometrical parameters [134].

7.2.2 Extraordinary transmission assisted by acoustic surface waves

Discovery of the extraordinary optical transmission through a two-dimensional array of subwavelength holes in a metallic film has opened a new line of research within optics [118]. Transferring light efficiently from the input to the output side is realized by surface plasmons. This fundamental knowledge enabled the extension of this surface-plasmon ability to achieve extraordinary optical transmission and strong collimation of light in a single hole surrounded by a finite periodic array of indentations. In analogy with the electromagnetic case, the main actors necessary for the appearance of both enhanced transmission and collimation in acoustics are the acoustic surface waves [137]. To realize the extraordinary transmission of acoustic surface wave one can use a grooved surface such as the one shown in Fig 7.1. Figure 7.7 shows the normalized-to-area transmission spectrum for a normal incident acoustic plane wave propagating in air across the single subwavelength slit (inset of Fig. 7.7), as well as the transmission spectrum in case the aperture is a slit of the same size but flanked by periodic grooves [137].

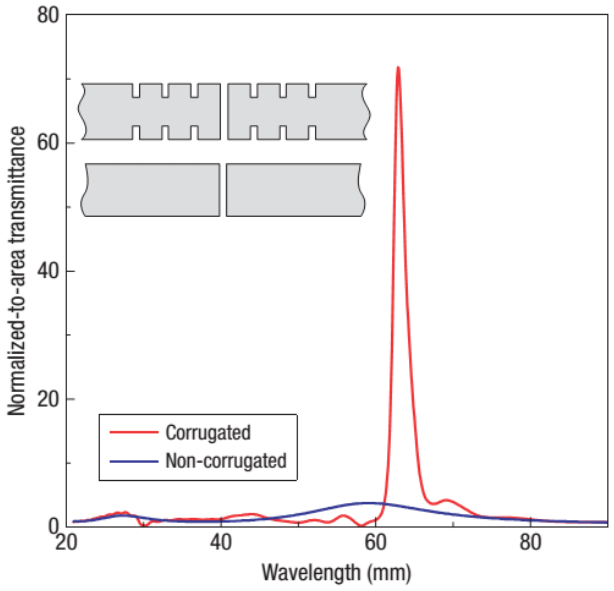

Figure 7.7 Transmission of sound through a single subwavelength slit (From [137])

A resonant peak appearing at a wavelength close to the period of the array clearly dominates the spectrum. For sound of that particular wavelength, the transmitted intensity is 70 times larger than the one impinging directly at the slit opening. This means that a significant portion (30%) of the

intensity incident on the finite array of grooves is collected by the acoustic surface waves and funneled through the central slit [137]. Detailed theoretical analyses of the extraordinary transmission phenomena are given in [138, 139].

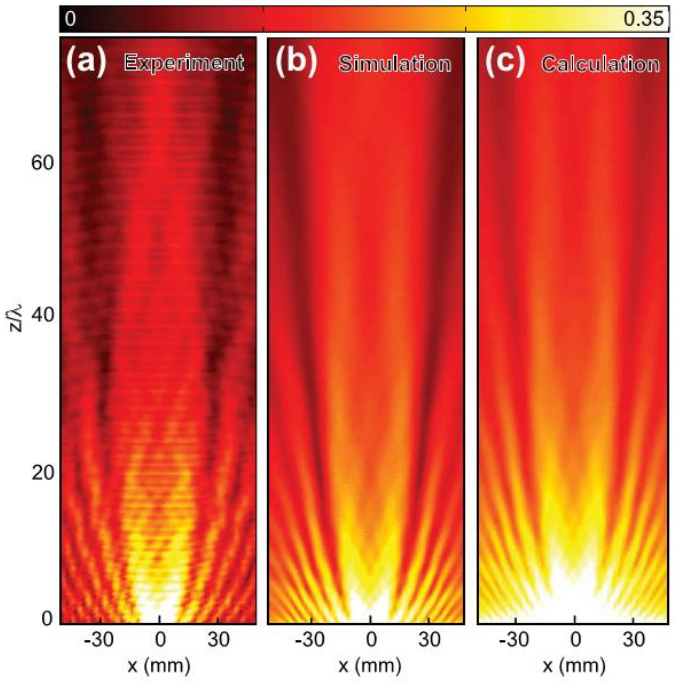

Figure 7.8 (a) Experimental, (b) simulated (c) calculated result of full-range intensity field pattern in the xz plane at the resonance frequency, showing the collimation effect. (From [139])

At the output side, the grooves act as radiators to effectively couple acoustic surface waves to radiative waves in free space when the phases are matched. [139] Figure 7.8 shows the experimental results of the full range intensity field pattern at the resonance frequency, which agrees with simulations and calculation results, also shown in Fig 7.8.

8. Temperature-controlled acoustic surface waves

In the previous chapter it was shown how the wave number on the surface can be controlled by varying geometrical parameters of the grooved surface. However, the main drawback of the proposed technique for manipulating surface acoustic waves is that the effect depends directly on the geometry of the grooves, and that it can thus be tuned only through physical modifications of the geometry. In this chapter it will be demonstrated that a surface acoustic wave propagating at the boundary between a fluid and a hard grooved surface can be efficiently controlled by varying just the temperature of the fluid, while the geometry of the grooved surface remains unchanged. This opens up a way for a number of new applications, all easily tunable by external means. Following the theoretical considerations, we will demonstrate temperature-controlled sound trapping and its applications in acoustic spectral analysis and temperature sensing. We will also present a temperature-controlled gradient refractive index (GRIN) acoustic medium and apply it to achieve temperature-controlled acoustic focusing and bending acoustic plane wave on a surface for an arbitrary angle.

8.1 Theoretical description

A typical example of a grooved surface used to support surface acoustic waves is shown in Fig. 8.1, where *d*, *a*, and *h* represent the period, the width and the depth of the grooves, respectively.

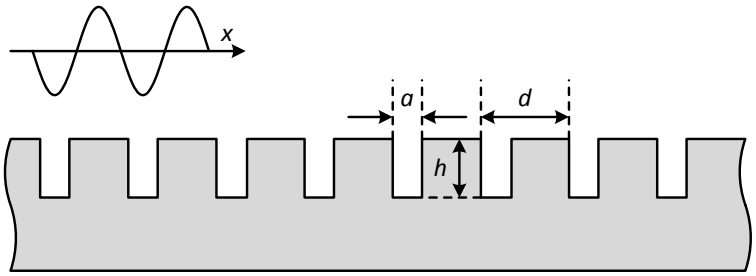

Figure 8.1 A typical grooved surface which supports propagation of acoustic surface waves.

When the period of the grooves is much smaller than the guided wavelength of the propagating acoustic surface wave, the grooved surface can be considered as an effective medium and characterized by an effective density tensor. For an acoustic surface wave propagating along the direction *x*, the effective dispersion relation of such a medium is [131]

$$k_x = k_0 \sqrt{1 + \left(\frac{a}{d}\right)^2 \tan^2(hk_0)}, \tag{8.1}$$

where k_0 denotes the wavenumber in free space, considered here to be dry air and modeled as an ideal gas. To express the effective dispersion relation as a function of temperature, we first note that the wavenumber k_0 in any ideal gas is the following function of temperature:

$$k_0(T) = \omega \sqrt{\frac{\rho_0(T)}{\kappa p}}, \tag{8.2}$$

where ρ_0 is the gas density, κ is the adiabatic constant and p is the atmospheric pressure. From the ideal gas state equation, the gas density can be obtained as a function of temperature:

$$\rho_0(T) = \frac{p}{RT}, \tag{8.3}$$

where R denotes the specific gas constant, and T is the temperature in K. In case of dry air, $\kappa = 1.4$, $R = 287.05\,\mathrm{J/kgK}$ and the atmospheric pressure is $p = 101325\,\mathrm{Pa}$. Finally, the effective wavenumber is obtained in the temperature dependent form as [142]:

$$k_x(T) = \omega\sqrt{\frac{1}{\kappa RT}}\sqrt{1 + \left(\frac{a}{d}\right)^2 \tan^2\left(h\omega\sqrt{\frac{1}{\kappa RT}}\right)} \tag{8.4}$$

and plotted in Fig. 8.2 for a range of temperatures, when the geometrical parameters of the surface are constants and have been arbitrarily chosen to be a = 0.2 mm, d = 1 mm, and h = 24 mm. It can be seen that, for a given temperature, the medium is non-dispersive at low frequencies. However, as frequency increases, strong dispersion occurs, the effective wavenumber asymptotically approaches infinity and finally a stop-band appears. It can also be seen that the frequency at which dispersion occurs and the position of the stop-band depend on the temperature. To validate the analytical solution (8.4), the results of 2-D full-wave FEM simulations for the case of T = 298 K are also shown in Fig. 8.2. The simulations have been performed in COMSOL Multiphysics 4.4 using pressure acoustic module. The temperature in the whole system was defined as a constant value T = 298 K and the air was modeled as an ideal gas. It can be seen that a very good agreement exists between the analytical and full-wave solutions. We note here that (8.1) is strictly valid for an infinitely wide grooved surface. However, it has been shown that it actually holds as long as the width of the surface is larger than the period of the grooves d [127, 128]. This is confirmed in Fig. 8.2 where COMSOL simulations of the grooved surface with finite overall width equal to 10d = 10 mm are also shown, and they agree very well with the 2-D simulation results. As it was shown in the previous chapter, the wavenumber can be changed by varying external parameters, and Fig. 8.3 shows the dependence of the wavenumber k_x on the temperature at the operating frequency of 3.4 kHz, when the geometrical parameters are kept constant. This frequency has been chosen arbitrarily within the range in which prominent dispersion occurs. Figure 8.3 also shows the phase velocity of the surface wave.

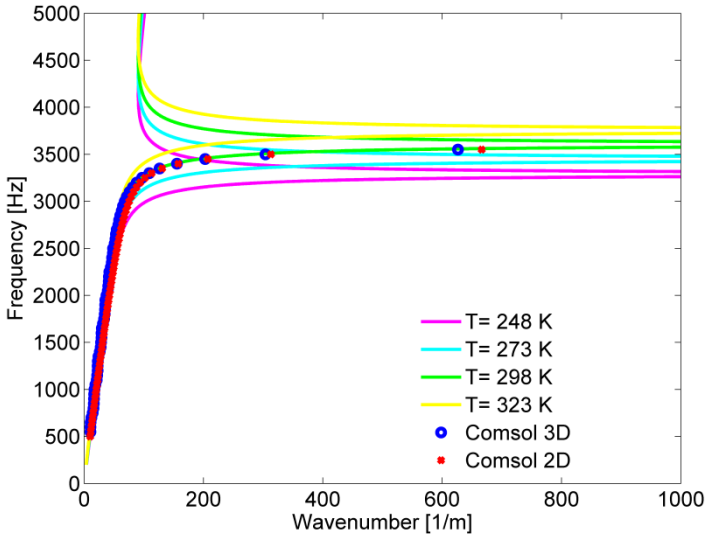

Figure 8.2 Dispersion relation of acoustic surface waves as a function of temperature. Analytical solutions (8.4) are shown with solid lines, while the dashed line represents 2-D and 3D full-wave FEM simulations for the case T = 298 K.

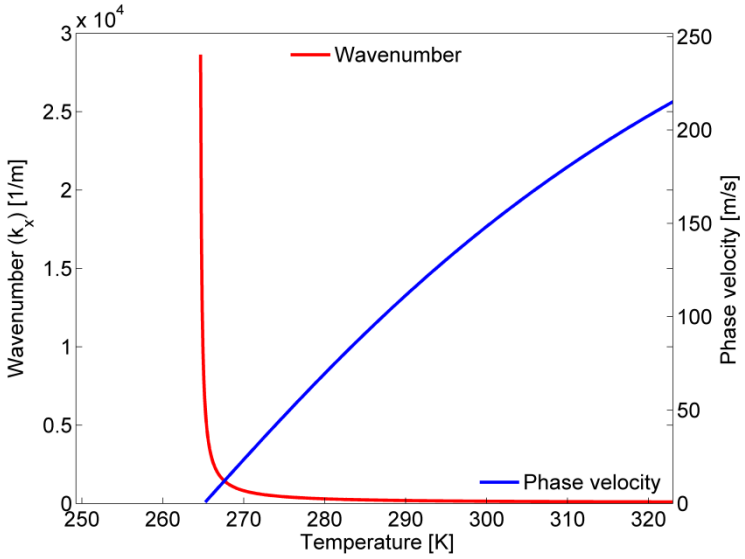

Figure 8.3 The temperature dependence of the phase velocity and wavenumber at 3400 Hz.

It can be seen that the wavenumber increases slowly and the phase velocity decreases with decreasing temperature until the temperature reaches a critical value T_c, at which the wavenumber increases extremely, theoretically to infinity. Below T_c no propagation can occur. The critical temperature T_c can be obtained from Eq. (8.4) as a function of the operating frequency f and the depth of the grooves h:

$$T_c = \frac{16h^2 f^2}{\kappa R}. \tag{8.5}$$

For the given operating frequency and geometrical parameters, T_c equals 264.9 K. It should be noted that the discussion above does not hold in the close vicinity of T_c, where the wavenumber becomes too large and the effective medium concept is lost since the guided wavelength becomes

comparable with the period d. The effective media concept can thus be applied as long as the guided wavelength is larger than approximately $4d$, i.e. $k_x < \pi/2d$. In the previous chapter it was shown that with increasing wavenumber the wave slows down and the sound intensity also increases to a maximal value immediately before the surface wave stops. For that reason the sound intensity was used to show where the surface wave stops. In COMSOL FEM simulator three grooved surface with same length (L= 500 mm) were designed, with a different period d, and with a constant ratio a/d = 0.2 to keep the same dispersion characteristic (Eq. 8.4). Linear temperature variation was used along the structure, with the same linear temperature gradient for all three models. Figure 8.4 shows the normalized sound intensities for the acoustic surface wave, as well as the calculated critical temperature.

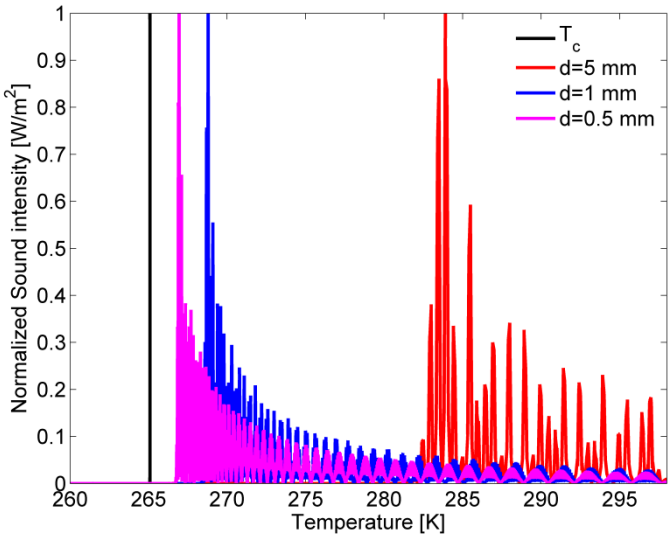

Figure 8.4. Normalized sound intensity dependence from temperature on same frequency (3.4 kHz) with different period d

It can be seen that the wave propagating along structures with different periods and with same dispersion characteristics stops at different temperatures, and with decreasing the period these temperatures converge to T_c. The temperature at which the wave stops (T_s) are $T_{S1} \approx 283$ K, $T_{S2} \approx 268$ K, $T_{S3} \approx 266$ K for periods $d_1 = 5$ mm, $d_2 = 1$ mm, $d_3 = 0.5$ mm respectively. In Fig. 8.3 it can be seen that the temperatures T_s are exactly those at which the wavelength becomes comparable with the period ($d \approx \lambda/4$) and the effective medium theory is inadequate. The results presented above indicate that a good control of the surface acoustic waves can be obtained by varying the temperature alone, while the grooved surface remains unchanged. This is illustrated in Fig. 8.5 where the acoustic pressure field distribution over a grooved surface is shown for four different values of the temperature of the surrounding medium, all within the limits of room temperatures. For the same applied frequency, the wavelength of the surface acoustic wave varies significantly. Namely, it changes from 40 mm to 14 mm when the temperature is decreased from 303 K to 283 K.

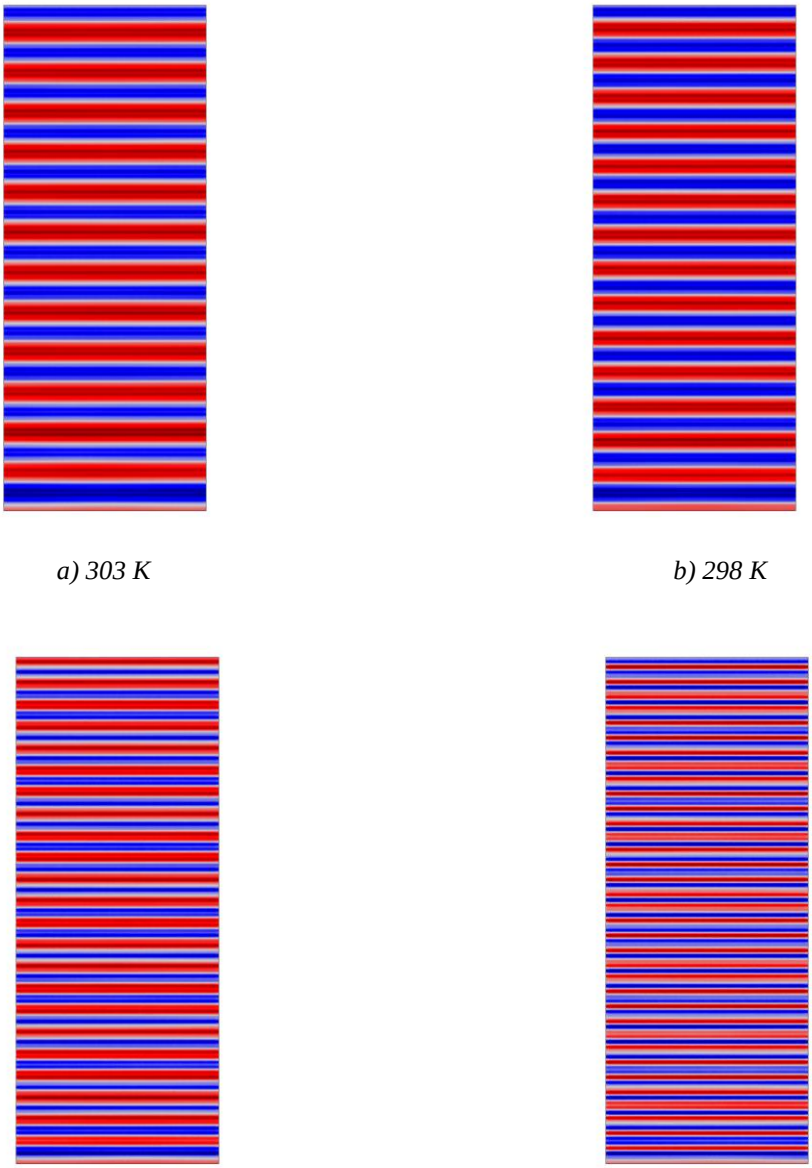

a) 303 K *b) 298 K*

c) 288 K *d) 283 K*

Figure 8.5 Acoustic pressure distribution when the temperature is constant on the whole surface (d = 1 mm, a = 0.2 mm, h = 24 mm), indicating the dependence of wavelength on temperature variation

8.2 Acoustic surface wave trapping and spatial acoustic spectral analysis

If the temperature of the surrounding medium decreases gradually along the propagation direction, the acoustic surface wave will slow down and stop when the temperature reaches T_s. In this way, an acoustic wave of a given frequency can be trapped at any desired point along the surface, simply by tuning the temperature of the surrounding medium. This is illustrated in Fig. 8.6 where three arbitrary cases are shown, each obtained by using a different linear temperature gradient (shown in the inset), the trapping temperature is also shown in inset (black horizontal line). In each case, the trapping occurs at the position along the grooved surface where the surrounding temperature reaches T_s.

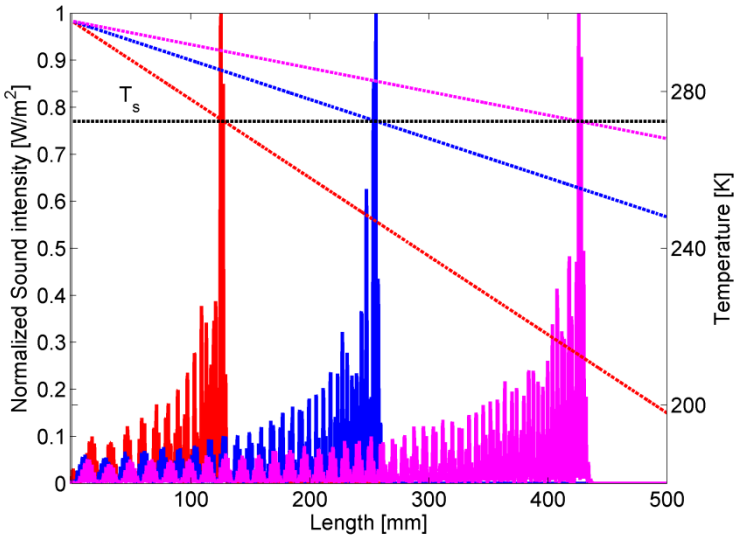

Figure 8.6 Acoustic surface wave trapping at arbitrary locations along the grooved medium is obtained by applying different temperature gradients (f=3.4 kHz).

Alternatively, for a given temperature gradient, surface waves of different frequencies will be trapped at different points along the surface, as shown in Fig. 8.7. In this way, spatial spectral analysis of acoustic surface waves can easily be realized.

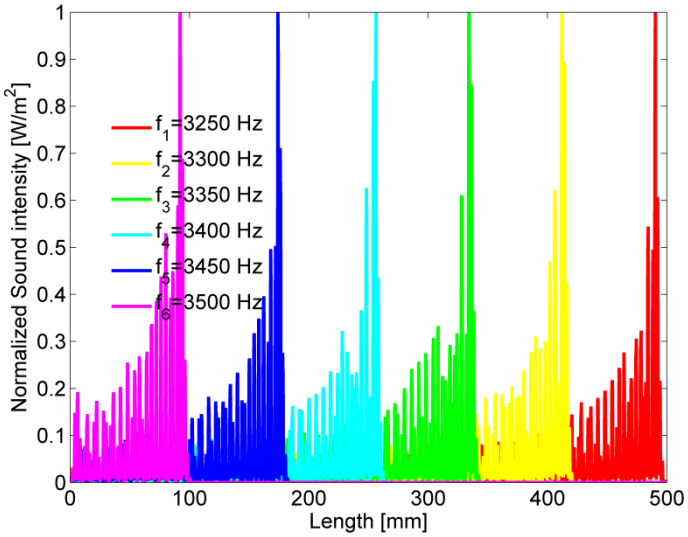

Figure 8.7 Spatial acoustic spectral analysis is obtained as acoustic waves of different frequencies are trapped at different positions along the surface.

8.3 Temperature sensing (Temperature mapping)

Another application of the proposed concept is temperature sensing (i.e. temperature mapping), where the temperature is estimated from the distribution of acoustic pressure on the grooved surface. To illustrate this concept, a grooved surface with two arbitrarily positioned radiation heat sources is shown in Fig. 8.8, together with the corresponding temperature distribution. A multiphysic simulation model was designed in COMSOL combining Acoustic and Heat transfer modules. The simulation

consists of two steps. The first step is in time domain, radiation sources start to radiate from 0 *s* to a certain end time, which was arbitrarily set to 60 s. The resulting temperature distribution is shown in Fig. 8.8. The second step is in frequency domain, with the acoustic plane wave source working at the defined frequency (3.4 kHz), while the medium has a temperature distribution equal to the one observed in the first simulation step. The resulting pressure field distribution is shown in Fig. 8.8. It can be seen that the guided wavelength increases proportionally to the temperature, due to the decreased wavenumber in warmer regions. Therefore, the temperature can be uniquely estimated from the guided wavelength, which can easily be determined from phase measurements at two close locations along the structure.

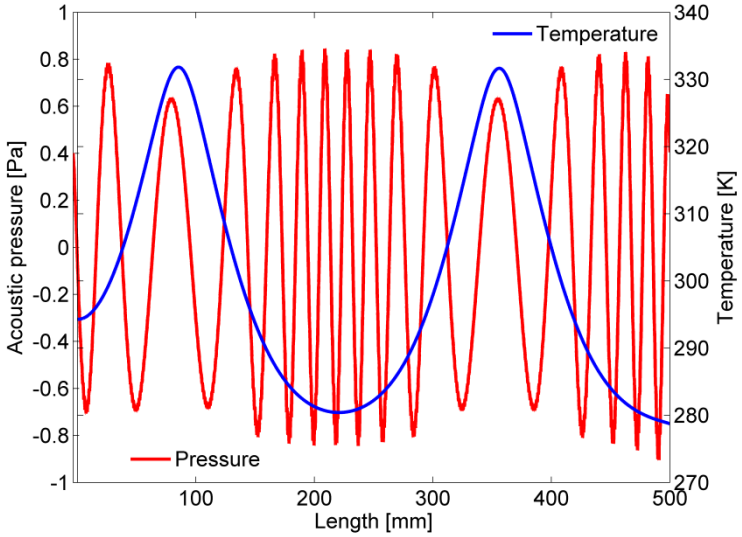

Figure 8.8 Temperature distributions in the surround medium (blue). Acoustic pressure field distributions along the grooved surface (red)

8.4 Temperature-controlled gradient refractive index (GRIN) acoustic medium

In the preceding analysis, temperature gradient has been applied along the propagation direction of surface waves. However, the temperature gradient can also be applied in a direction transverse to the propagation direction. In that way, an acoustic gradient refractive index (GRIN) medium can be obtained [45, 140, 143, 144, 145]. To illustrate this, an acoustic surface host waveguide (medium) with width w = 500 mm and length L = 850 mm has been designed. In the middle of the structure one rectangular section with the thickness t = 100 mm was cut along the propagation direction into 50 uniform waveguides with individual widths of 10 mm. Since the width of each waveguide is 10 times larger than the applied period (d = 1 mm), the dispersion relation (8.1) is valid and the effective medium concept can be applied. The structure is shown in the Fig 8.9.

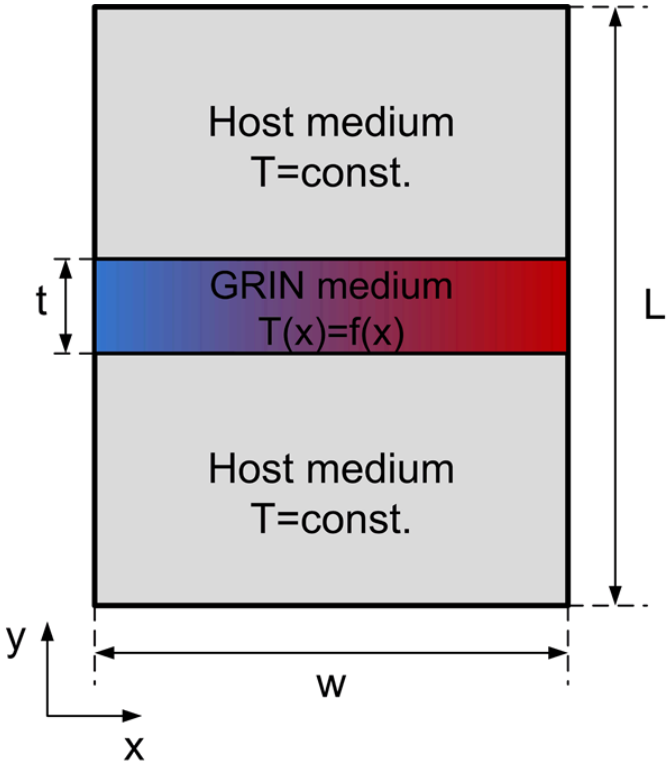

Figure 8.9. Illustration of the designed GRIN structure

The structure has been simulated in COMSOL Multiphysics 4.4, with ideal thermal isolation assumed between its different regions. The temperature in the host waveguide is kept constant and equal to T_0 = 306 K. The temperatures in individual regions of the structure have been calculated by combining Eq. (8.4) and the desired refractive index profile function along the direction transversal to the propagation. The refractive index between the host waveguide and the GRIN lens can be calculated as the ratio between the wavenumbers in two different media:

$$n_i = \frac{k_i}{k_0}, \tag{8.6}$$

where n_i is the refractive index between the *i*-th medium with wavenumber k_i and the host medium with wavenumber k_0. During this research we have designed a range of of GRIN media with same geometrical parameters and with different temperature distribution, different refractive index profiles, specified profile function for bending acoustic plane waves by different angles [144] and the hyperbolic secant refractive index profile function for a focusing [45, 140, 145, 146], and thus we have shown that the proposed structure is indeed suitable for tunable applications.

8.4.1 Bending an acoustic surface plane wave

With linear refractive index profile in the GRIN medium the incident plane wave can be bent by an arbitrary angle [143]:

$$n(x) = 1 + \frac{n_{max} - 1}{w} x, \tag{8.7}$$

where w is the width of the lens and n_{max} is the maximal value of refractive index in GRIN medium. The bending angle is a function of the width and the thickness of the lens and the maximal value of the refractive index and can be calculated as:

$$\Theta = \sin^{-1}\left[\frac{t}{w}(n_{max} - 1)\right]. \tag{8.8}$$

In case when the bending angle is defined the maximal refractive index can be calculated by inverting Eq. (8.8) into:

$$n_{max} = \frac{w}{t}\sin\Theta + 1. \tag{8.9}$$

Using the refractive index profile given by Eq. (8.7) and combining Eqs. (8.4) and (8.6), the wavenumber and the temperature in all regions can be calculated. Matlab code for calculating temperature distribution for a wave bending GRIN medium is given in *Appendix A6*. In COMSOL model the GRIN medium consists of 50 uniform regions and a thermal isolation boundary is positioned between them. The calculated temperature distribution in the GRIN medium for 15° bending is shown in Fig.8.10.

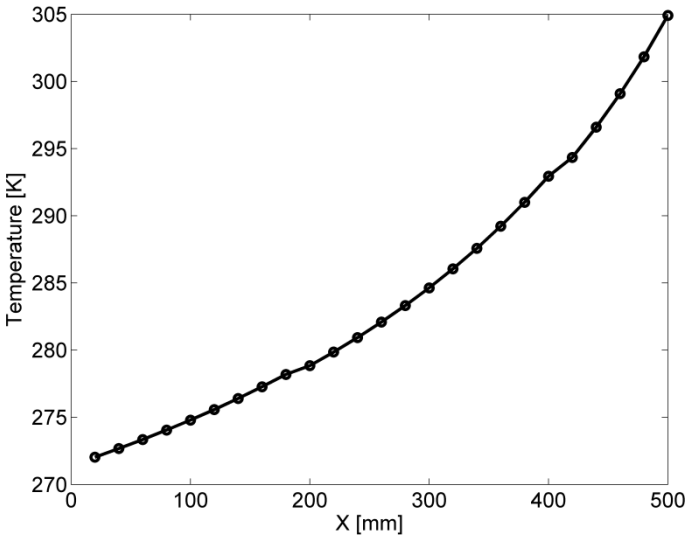

Figure 8.10. Temperature T_i [K] in the lens along the direction transverse to propagation direction for bending the acoustic surface wave by Θ= 15°

In this situation the maximal value of the refractive index is n_{max}= 1.78 and the temperature difference between the two sides of the lens is 32.8 K. The acoustic pressure phase distribution on the surface is shown in Fig. 8.11.

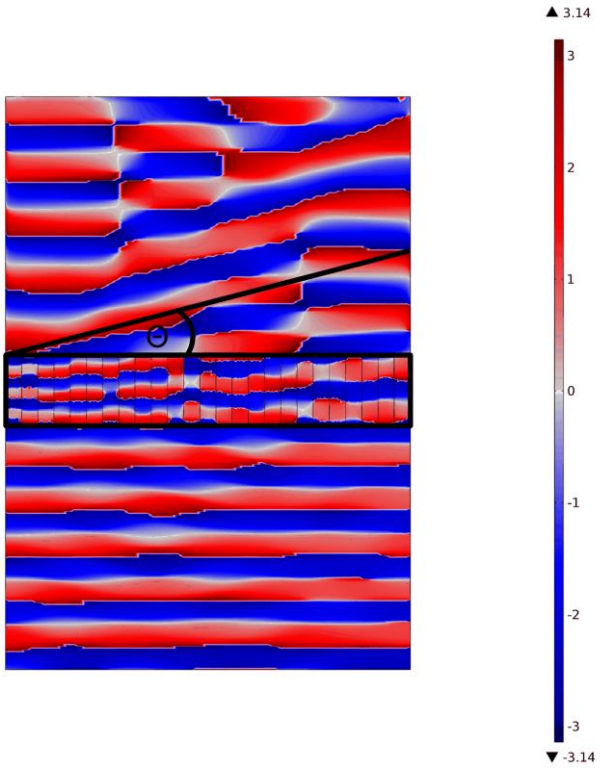

Figure 8.11. Acoustic pressure phase distribution on surface (Θ= 15°)

From the pressure distribution it can be seen that the incident plane wave (going upwards) after the interaction with the GRIN medium is indeed bent by the defined angle Θ. To demonstrate the tunability of the proposed approach, another bending angle was produced with same geometrical parameters . The calculated temperature distribution in the GRIN medium for a 30° bending is shown in Fig.8.12.

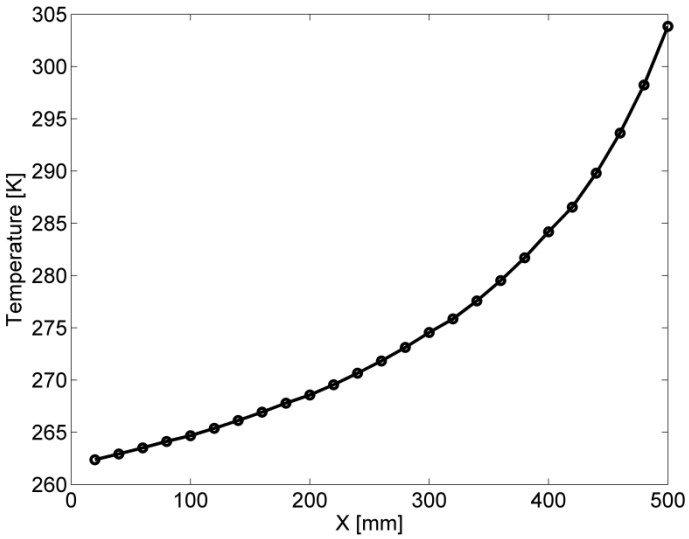

Figure 8.12 Temperature T_i [K] in lens along the direction transverse to propagation direction for a bending on angle Θ= 30°

In this situation the maximal value of the refractive index is n_{max}= 2.5 and the temperature difference between the two sides of the lens is 41.5 K. The acoustic pressure phase distribution on the surface is shown in Fig. 8.13.

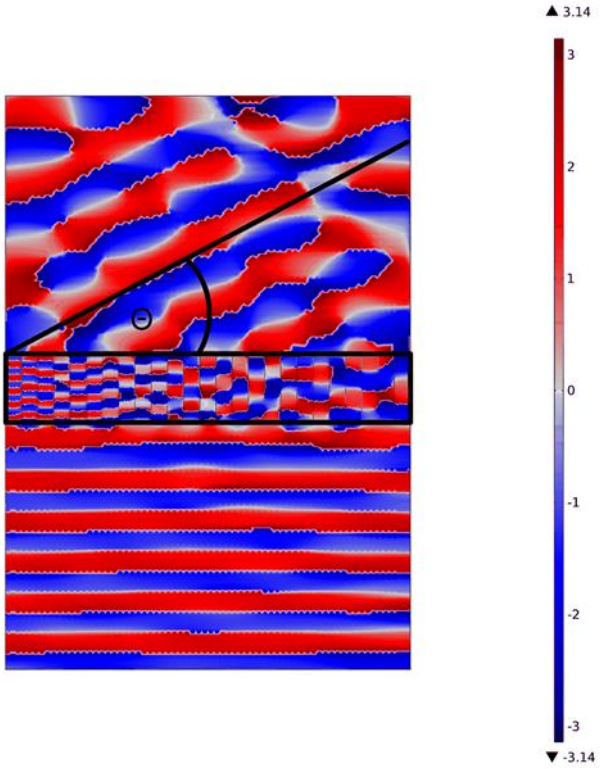

Figure 8.13. Acoustic pressure phase distribution on the surface (Θ= 30°)

From the pressure distribution it can be seen that the incident plane wave (going upwards) is bent by the defined angle *Θ* after interacting with the GRIN medium.

8.4.2 Focusing an acoustic surface plane wave

The most common refractive index profile in GRIN medium for focusing is the hyperbolic secant refractive index profile [45, 140, 143, 144, 145], which exhibits no distortions [146]. The hyperbolic secant refractive index profile is given by:

$$n(x) = n_0 \,\mathrm{sech}(\alpha x) \tag{8.10}$$

where n_0 is the index of refraction in the center of the lens and α is the gradient parameter, equal to:

$$\alpha = \frac{2}{w}\cosh^{-1}\left(\frac{n_0}{n_w}\right), \tag{8.11}$$

where w is the width of the lens and n_w is the index of refraction at its edge. For demonstrating versatility and tunability of the structure three different hyperbolic secant profiles were designed by changing the temperature distribution in the GRIN medium. Using the refractive index profile Eq. (8.10) and combining Eqs. (8.4) and (8.6), the wavenumber and the temperature in all regions can be calculated. Matlab code for calculating the temperature distribution for a hyperbolic secant profile GRIN medium is given in *Appendix A6*. Input parameters were the refractive indexes at the edge and in the center of the GRIN medium. In the first case the refractive index was chosen to be n_0 = 1.5 and

$n_w = 1$ at the edges on the medium. The calculated temperature distribution in the GRIN medium for the first case is shown in Fig. 8.14.

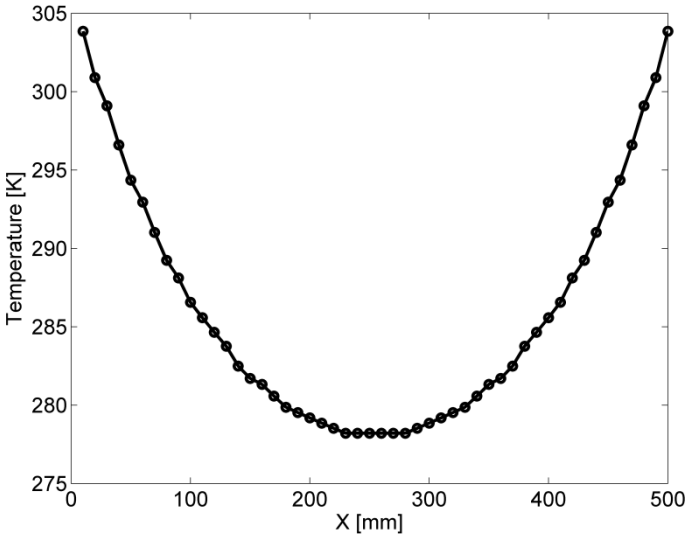

Figure 8.14 Temperature T_i [K] in lens along the direction transverse to propagation direction for focusing with central refractive index $n_0 = 1.5$

Temperature distribution has a hyperbolic secant shape and the maximal temperature difference between the center and the edge of the structure is $\Delta T = 28$ K. Acoustic pressure distribution on the surface is shown in Fig. 13. In the GRIN medium (framed with a black rectangle) the wave starts to bend and after the medium the wave is focused on one point.

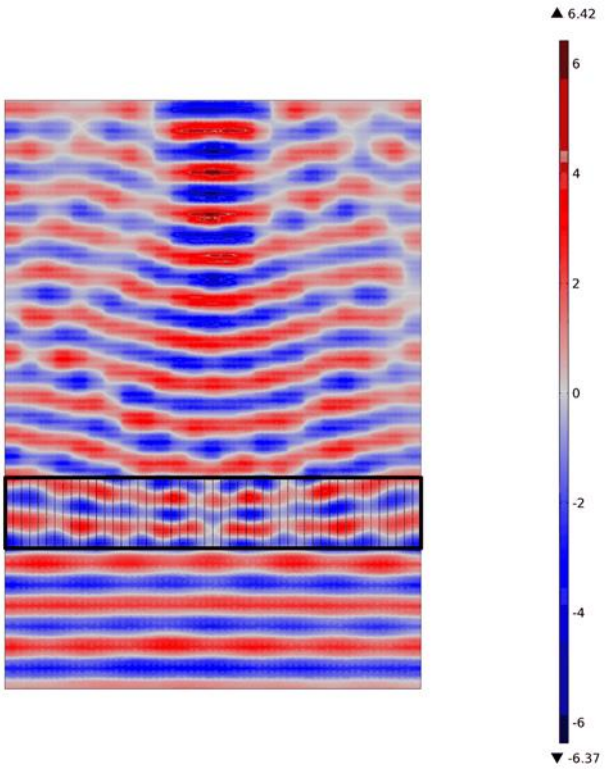

Figure 8.15. Acoustic pressure distribution on the surface

To indicate the focal point better, Figures 8.16a and 8.16b show the absolute pressure and the sound wave intensity distribution on the surface respectively.

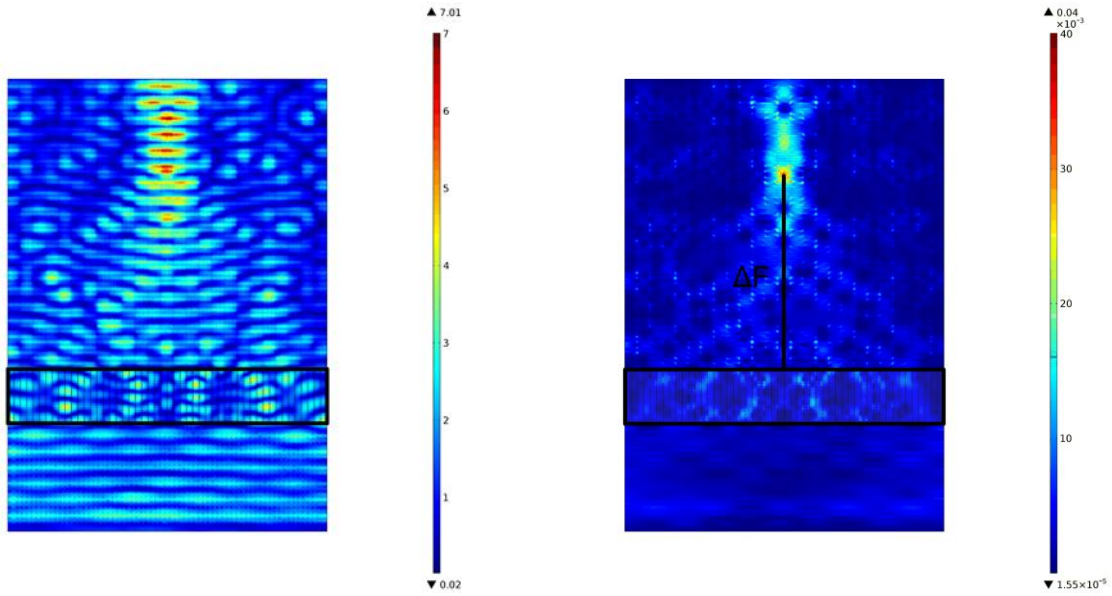

a) b)

Figure 8.16 Distribution of a) absolute pressure field and b) sound intensity on the surface

From Figs 8.16a and 8.16b it can be clearly seen that the pressure amplitude increases near the focal point and that the most of sound intensity is focused in one point. This point is in the middle of the structure and the distance from the lens is ΔF= 360 *mm*, as also marked in Fig.8.16b. The sound intensity along the wave propagation path (vertical line in the middle) is shown in Fig. 8.17a, and it can be seen how the sound increases before the focal point and decreases after it.

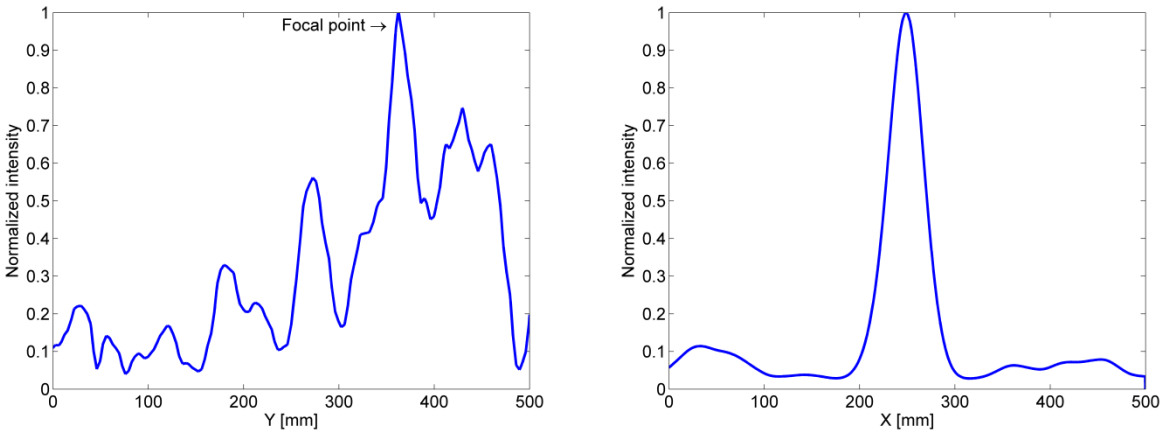

a) *b)*

Figure 8.17 Normalized sound intensity along the a) y direction in the middle of the structure (x=250 mm) and b) x direction (y=ΔF)

Figure 8.17b shows the sound intensity along the direction transverse to the wave propagation at a distance equal to focal length (horizontal line across the structure and at a distance ΔF from the GRIN lens). It can be seen that the sound intensity is indeed focused in the middle of the structure

where the focal point is positioned. In the second case a hyperbolic secant profile was calculated with parameters $n_0 = 1.8$ and $n_w = 1$. The calculated temperature distribution in the GRIN medium for the second case is shown in Fig. 8.18.

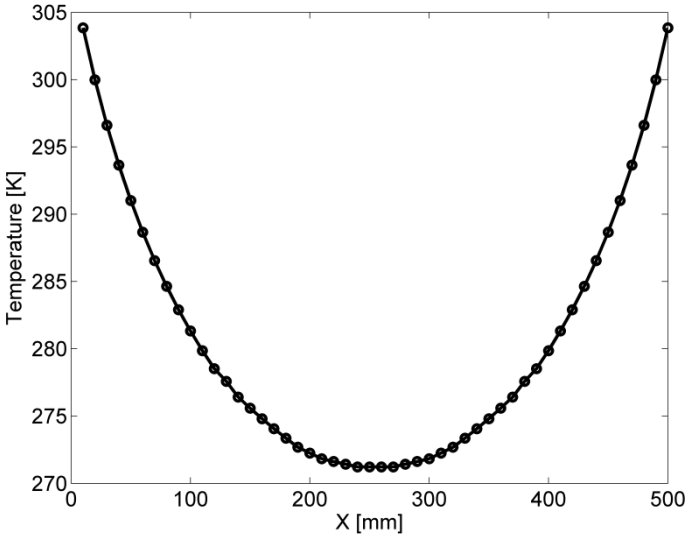

Figure 8.18 Temperature T_i [K] in the lens along the direction transverse to propagation direction for focusing with central refractive index n_0=1.8

Temperature distribution has a hyperbolic secant shape and the maximal temperature difference between the center and the edge of the structure is ΔT= 35 K. Figures 8.19a and Fig. 8.19b show the absolute pressure and the sound wave intensity distribution on the surface respectively.

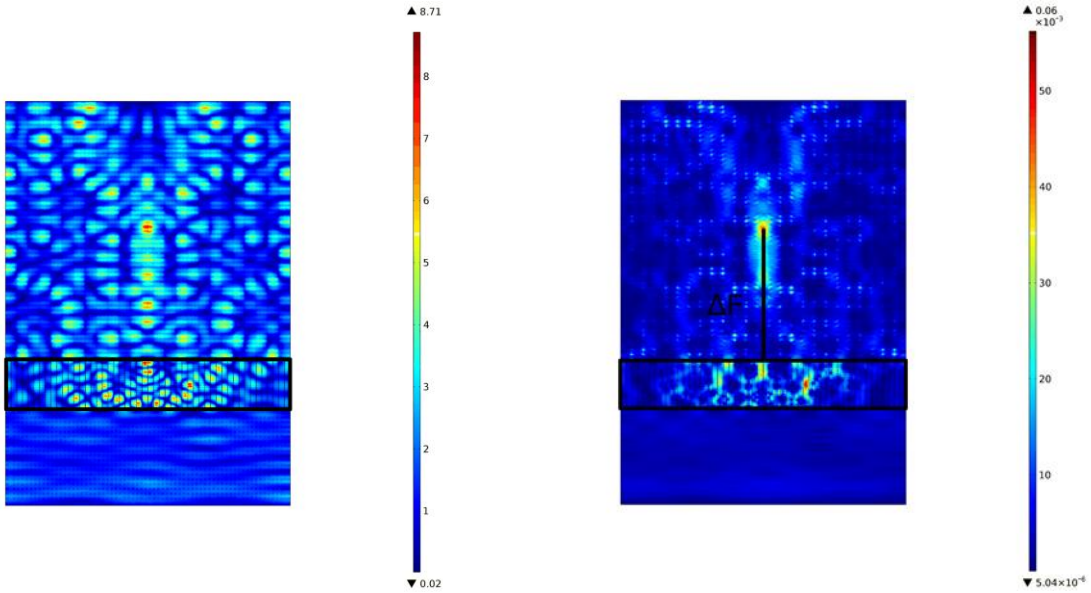

a) *b)*

Figure 8.19 Distribution of a) absolute pressure field and b) sound intensity on the surface

In Figs 8.19a and 8.19b the point where the sound intensity is focused can be clearly seen. The focal point is in the middle of the structure and at the distance from the lens equal to $\Delta F = 270$ *mm*, as also marked in Fig.8.19b. The sound intensity along the wave propagation path (vertical line in the

middle) is shown in Fig. 8.17a, and it can again be seen that the sound increases before the focal point and decreases after it.

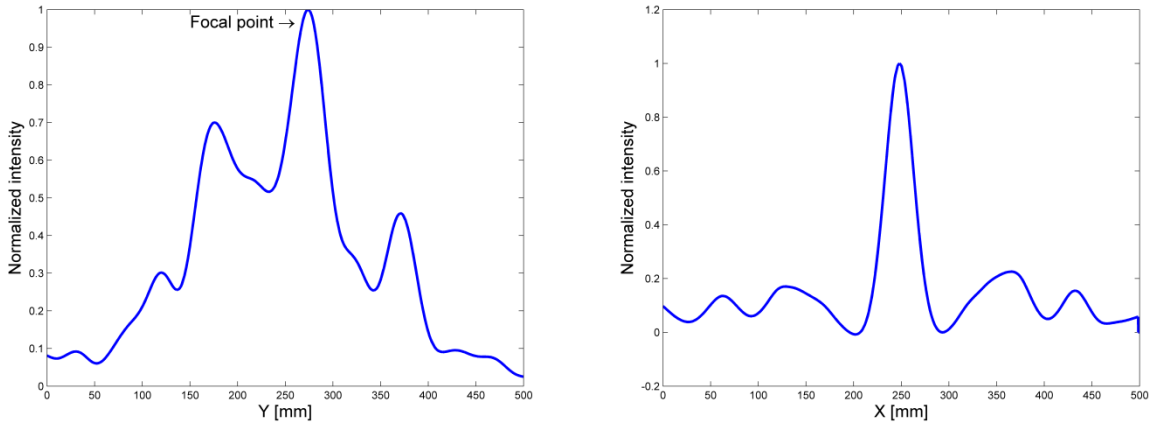

a) *b)*

Figure 8.20 Normalized sound intensity along the a) y direction in the middle of the structure (x=250 mm) and b) x direction (y=ΔF)

Figure 8.20b shows the sound intensity along the direction transverse to the wave propagation across the focal point (horizontal line at the distance ΔF from the GRIN lens). In both cases presented here the refractive index on the edge of the structure was equal to 1 but this is not necessary. By changing the temperature arbitrary profiles can be defined, according to the needs of a particular application. Since the temperature in all regions can be larger and smaller than the temperature in the host medium (T_0), the refractive index can also be smaller than 1. In the third case a hyperbolic secant profile with parameters n_0= 1.9 and n_w= 0.9 was defined. The calculated temperature distribution in the GRIN medium for this case is shown in Fig.8.21.

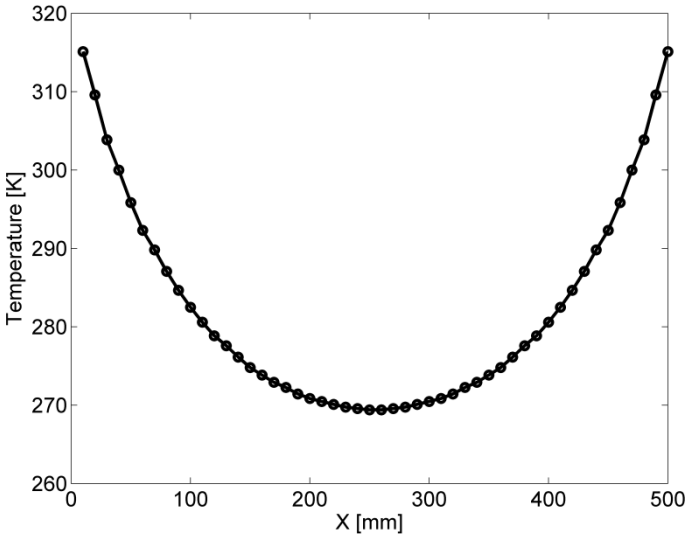

Figure 8.21 Temperature T_i [K] in the lens along the direction transverse to propagation direction for focusing with central refractive index n_0=1.9

It can be seen from Fig. 8.21 that temperature near the edges is higher than the temperature in the host medium, which is the consequence of the requirement that the refractive index should be less than 1. Temperature distribution has a hyperbolic secant shape and the maximal temperature difference between the center and the edge of the structure is ΔT = 48 K. Figures 8.22a and Fig. 8.22b show the absolute pressure and the sound wave intensity distribution on the surface respectively.

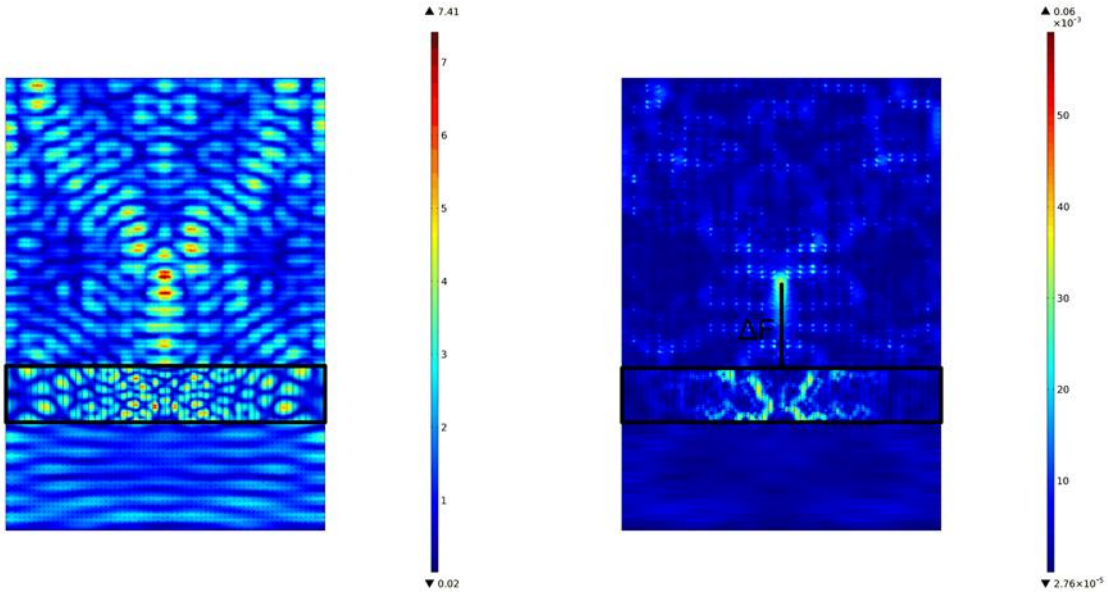

a) *b)*

Figure 8.22 Distribution of a) absolute pressure field and b) sound intensity on the surface

In Figs 8.22a and 8.22b the focus is, again, clearly visible, at the distance from the lens equal to ΔF= 160 *mm*, as indicated in Fig.8.22b. The sound intensity along the wave propagation path (vertical line in the middle) is shown in Fig. 8.23a, and it can, again, be seen how the sound increases before the focal point and decreases after it.

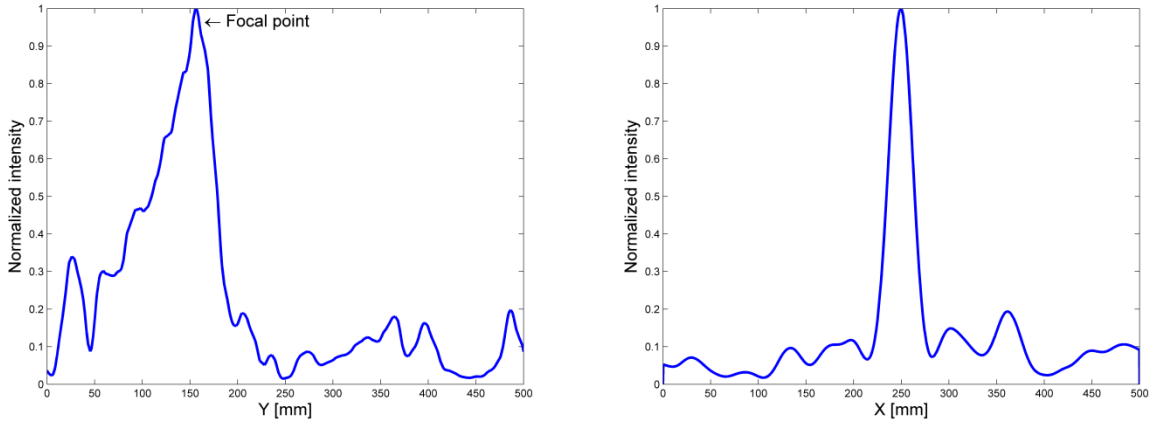

a) *b)*

Figure 8.23 Normalized sound intensity along the a) y direction in the middle of the structure (x=250 mm) and b) x direction (y=ΔF)

Figure 8.23b shows the sound intensity along the direction transverse to the wave propagation at the distance equal to focal length (horizontal line at the distance ΔF from the GRIN lens). After the analysis we can conclude that with temperature the surface acoustic wave propagation can be controlled. Different temperature distributions can be used depending on the application. The system can be easily tuned by varying the temperature and obtain a completely new functionality.

9. Conclusions and future work

The goal of this research was to analyze, design and realize new acoustic artificial media composed of subwavelength unit cells and demonstrate the possibility of non-conventional wave propagation through such media.

The scientific contribution of this dissertation consists of new types of acoustic wave propagation modes, such as near-zero propagation, i.e. acoustic wave propagation with infinite phase velocity. New resonant type metamaterial unit cell with negative mass density and a consequent new approach to the realization of left-handed acoustic wave propagation was also demonstrated. In the end of the thesis it was also shown that surface wave propagation can be easily controlled by varying the temperature of the surround medium.

All structures were designed, modeled and simulated with two different numerical simulation models, namely, the finite element method (FEM) simulation model and the simulation based on the transmission line model and the circuit theory (ABCD matrix, two-port network matrix transformations etc.). *COMSOL Multiphysics* FEM simulator was used to design and simulate 2D and 3D structures, while the code which follows the transmission line theory was written in *Matlab*.

At the beginning of the research a method was developed to analyze the behavior of acoustic metamaterial unit cells and acoustic two port systems with acoustic scattering parameters. The method is based on the measurement with four microphones and signal processing in order to recover the parameters of the acoustic scattering matrix. The method was used to characterize the acoustic two port systems.

The thesis also presented a novel class of one-dimensional near-zero acoustic metamaterials based on near-zero values of effective compressibility, realized using resonant-type metamaterials (Helmholtz resonator). The conditions needed to support compressibility near zero propagation have been theoretically analyzed in detail and experimentally verified. The fabricated prototype was characterized using the developed method for extraction of the acoustic scattering parameters for two port systems. The unique properties of CNZ propagation such as phase change minimization open a way for the development of various applications, in both audible and ultrasound ranges.

The thesis also demonstrated a new acoustic metamaterial unit cell based on a simple electro-acoustic analogy with the typical resonant-permeability unit cell from the domain of electromagnetic metamaterials, which was shown to be an efficient means to provide negative mass density to acoustic metamaterials. A closed analytical formula for the effective density of the proposed cell has been developed, confirming that at a range of frequencies the value of this parameter is indeed negative. The versatility of the proposed approach has been demonstrated through examples including single- and multi-stopband acoustic media with steep roll-offs, as well as left-handed and density-near-zero acoustic wave propagation.

The research presented in the thesis has also shown that the temperature of the surrounding medium can be used to manipulate surface acoustic waves in a variety of ways, through applications such as acoustic wave trapping, spatial spectral analysis of wideband acoustic waves, as well as acoustic wave steering and focusing. Unlike standard techniques for manipulation of surface acoustic waves, which require careful design of the surface geometry, this approach offers a simple solution, applicable to surfaces with uniform geometries and easily adaptable to any change in system specifications, thus allowing wave steering over variable paths or wave focusing with a variable focal length using temperature-controlled gradient refractive index (GRIN) acoustic lenses. Furthermore, the same phenomenon can be used in the opposite direction, for sensing the temperature of the fluid through the behavior of the acoustic wave, which extends the field of its application even further.

The results presented in the thesis constitute only one part of the research which is still not finished. Unfortunately we did not have a facility to fabricate more complex structures until quite recently, but now we are able to fabricate and characterize them. Our future work will include the fabrication and experimental characterization of all newly developed resonant type metamaterial unit cells. The new unit cells can also can be used as unit cells of tunable acoustic metasurfaces which can be used as acoustic beam formers. One of the next steps in this research is to fabricate and characterize this metasurface, combining different technologies as a LTCC and thin film technology. The research related to acoustic surface waves also continues, by fabrication of all proposed structures in 3D printing technology and their characterization. Novel applications in domains such as sensing will also be investigated.

Appendix A

A1. Matlab code: Extraction of the acoustic S-matrix

```
clear all;
close all;
clc;
rho_0=1.25; % density
B_0=1.42e5; % bulk modulus
c=sqrt(B_0/rho_0); % speed of sound
x1=0.1; % probe 1 position [m]
x2=0.05; % probe 2 position [m]
x3=0.05; % probe 3 position [m]
x4=0.1; % probe 4 position [m]
%----
load CNZa
load CNZb
    f=Pa(:,1);
    omega=2*pi*f;
    kx=omega/c;
    for p=1:length(Pa(:,1))
    P1a=Pa(p,2);
    P1b=Pb(p,2);
    P2a=Pa(p,3);
    P2b=Pb(p,3);
    P3a=Pa(p,4);
    P3b=Pb(p,4);
    P4a=Pa(p,5);
    P4b=Pb(p,5);
    k=kx(p);
    S11(p,1)=-(P1a*P3b*exp(i*k*x1)*exp(2*i*k*x2)*exp(i*k*x3) -
P1b*P3a*exp(i*k*x1)*exp(2*i*k*x2)*exp(i*k*x3) - P2a*P3b*exp(2*i*k*x1)*exp(i*k*x2)*exp(i*k*x3)
+ P2b*P3a*exp(2*i*k*x1)*exp(i*k*x2)*exp(i*k*x3) -
P1a*P4b*exp(i*k*x1)*exp(2*i*k*x2)*exp(i*k*x4) + P1b*P4a*exp(i*k*x1)*exp(2*i*k*x2)*exp(i*k*x4)
+ P2a*P4b*exp(2*i*k*x1)*exp(i*k*x2)*exp(i*k*x4) -
P2b*P4a*exp(2*i*k*x1)*exp(i*k*x2)*exp(i*k*x4))/(P1a*P3b*exp(i*k*x1)*exp(i*k*x3) -
P1b*P3a*exp(i*k*x1)*exp(i*k*x3) - P1a*P4b*exp(i*k*x1)*exp(i*k*x4) +
P1b*P4a*exp(i*k*x1)*exp(i*k*x4) - P2a*P3b*exp(i*k*x2)*exp(i*k*x3) +
P2b*P3a*exp(i*k*x2)*exp(i*k*x3) + P2a*P4b*exp(i*k*x2)*exp(i*k*x4) -
P2b*P4a*exp(i*k*x2)*exp(i*k*x4));
    S12(p,1)=(P1a*P2b*exp(i*k*x1)*exp(i*k*x2)*exp(2*i*k*x3) -
P1b*P2a*exp(i*k*x1)*exp(i*k*x2)*exp(2*i*k*x3) - P1a*P2b*exp(i*k*x1)*exp(i*k*x2)*exp(2*i*k*x4)
+ P1b*P2a*exp(i*k*x1)*exp(i*k*x2)*exp(2*i*k*x4))/(P1a*P3b*exp(i*k*x1)*exp(i*k*x3) -
P1b*P3a*exp(i*k*x1)*exp(i*k*x3) - P1a*P4b*exp(i*k*x1)*exp(i*k*x4) +
P1b*P4a*exp(i*k*x1)*exp(i*k*x4) - P2a*P3b*exp(i*k*x2)*exp(i*k*x3) +
P2b*P3a*exp(i*k*x2)*exp(i*k*x3) + P2a*P4b*exp(i*k*x2)*exp(i*k*x4) -
P2b*P4a*exp(i*k*x2)*exp(i*k*x4));
    S21(p,1)=-(P3a*P4b*exp(2*i*k*x1)*exp(i*k*x3)*exp(i*k*x4) -
P3b*P4a*exp(2*i*k*x1)*exp(i*k*x3)*exp(i*k*x4) - P3a*P4b*exp(2*i*k*x2)*exp(i*k*x3)*exp(i*k*x4)
+ P3b*P4a*exp(2*i*k*x2)*exp(i*k*x3)*exp(i*k*x4))/(P1a*P3b*exp(i*k*x1)*exp(i*k*x3) -
P1b*P3a*exp(i*k*x1)*exp(i*k*x3) - P1a*P4b*exp(i*k*x1)*exp(i*k*x4) +
P1b*P4a*exp(i*k*x1)*exp(i*k*x4) - P2a*P3b*exp(i*k*x2)*exp(i*k*x3) +
P2b*P3a*exp(i*k*x2)*exp(i*k*x3) + P2a*P4b*exp(i*k*x2)*exp(i*k*x4) -
P2b*P4a*exp(i*k*x2)*exp(i*k*x4));
    S22(p,1)=-(P1a*P3b*exp(i*k*x1)*exp(i*k*x3)*exp(2*i*k*x4) -
P1b*P3a*exp(i*k*x1)*exp(i*k*x3)*exp(2*i*k*x4) - P1a*P4b*exp(i*k*x1)*exp(2*i*k*x3)*exp(i*k*x4)
+ P1b*P4a*exp(i*k*x1)*exp(2*i*k*x3)*exp(i*k*x4) -
P2a*P3b*exp(i*k*x2)*exp(i*k*x3)*exp(2*i*k*x4) + P2b*P3a*exp(i*k*x2)*exp(i*k*x3)*exp(2*i*k*x4)
```

```
+ P2a*P4b*exp(i*k*x2)*exp(2*i*k*x3)*exp(i*k*x4) -
P2b*P4a*exp(i*k*x2)*exp(2*i*k*x3)*exp(i*k*x4))/(P1a*P3b*exp(i*k*x1)*exp(i*k*x3) -
P1b*P3a*exp(i*k*x1)*exp(i*k*x3) - P1a*P4b*exp(i*k*x1)*exp(i*k*x4) +
P1b*P4a*exp(i*k*x1)*exp(i*k*x4) - P2a*P3b*exp(i*k*x2)*exp(i*k*x3) +
P2b*P3a*exp(i*k*x2)*exp(i*k*x3) + P2a*P4b*exp(i*k*x2)*exp(i*k*x4) -
P2b*P4a*exp(i*k*x2)*exp(i*k*x4));

    end
%--------DisplayResults

figure(1);
plot(f, 20*log10(abs(S11)),'r','linewidth',2.5);
hold on
plot(f, 20*log10(abs(S21)),'b','linewidth',2.5);
hold on
xlabel('Frequency [Hz]','fontsize',16);
ylabel('Reflection and transmission coefficeient [dB]','fontsize',16);
legend ('Reflection','Transmission');
set(gca,'fontsize',16);
grid off;
```

A2. Matlab code: Extraction of effective material parameters

```
clear all;
close all;
clc;
rho_0=1.25; % density
B_0=1.42e5; % bulk modulus
c=sqrt(B_0/rho_0); % speed of sound
   load MembranA
   load MembranB
    f=Pa(:,1);
len = 34e-3; % length of the structure
flist =f;
omega=2*pi.*flist;
k0=omega*sqrt(rho_0/B_0);
a=8.1e-3; % duct radius [m]
Zfactor=sqrt(rho_0*B_0);
lambda0 = c./flist;

k = (S11.^2 - S21.^2 + 1)./(2.*S11); % S-parameters from extraction S matrix
Gamma = k + sqrt(k.^2-1);
index = find(abs(Gamma)>1);
Gamma(index) = k(index) - sqrt(k(index).^2-1);

Gamma=real(Gamma)-i*abs(imag(Gamma));

zeff = (1+Gamma)./(1-Gamma)*(Zfactor);
xfactor=(((1+S11).*(1-S22) + S12.*S21 + (1-S11).*(1+S22)+S12.*S21))/4./S21;

newpfactor = 1/len.*log(xfactor+sqrt(xfactor+1).*sqrt(xfactor-1));
refractiveindex = newpfactor./(i*omega);

n_eff=refractiveindex;
n_frec=length(flist);
d_eff=len;

%%%%%%%%%%%%%%%%%%%%%%%%%%%%%%%%%%%%%%%%%%%%%%%%%%%%%%%%%%%%
%Step - 6 Apply Kramers-Kronig relations to approximate the real part of
%the refractive index from the imaginary part
%auxiliary variable
imag_n = imag(n_eff);

%stores the real part of N
n_re_KK = zeros(n_frec,1);

%it is supposed that the frequencies are equidistant
delta_omega = omega(2)-omega(1);

%Evaluate the Kramers-Kronig integral with trapeze rule
%Calculate the first element
term_a = imag_n(2)*omega(2)/(omega(2)^2 - omega(1)^2);
for i = 2:n_frec-1
    %trapeze rule for integration
    term_b        = imag_n(i+1)*omega(i+1)/(omega(i+1)^2 - omega(1)^2);
    n_re_KK(1)  = n_re_KK(1) + term_a + term_b;
    term_a        = term_b;
end;
n_re_KK(1) = 1.0 + delta_omega/pi*n_re_KK(1);
```

```
%Calculate the last element
term_a = imag_n(1)*omega(1)/(omega(1)^2-omega(n_frec)^2);
for i = 1:n_frec-2
    %trapeze rule for integration
    term_b = imag_n(i+1)*omega(i+1)/(omega(i+1)^2-omega(n_frec)^2);
    n_re_KK(n_frec)  = n_re_KK(n_frec) + term_a + term_b;
    term_a = term_b;
end;
n_re_KK(n_frec) = 1.0 + delta_omega/pi*n_re_KK(n_frec);

%Calculate the middle elements
for i = 2:n_frec-1;
    n_re_KK(i) = 0.0;
    term_a = imag_n(1)*omega(1)/(omega(1)^2 - omega(i)^2);
    for j = 1:i-2
        %trapeze rule for integration
        term_b     = imag_n(j+1)*omega(j+1)/(omega(j+1)^2 - omega(i)^2);
        n_re_KK(i) = n_re_KK(i) + term_a + term_b;
        term_a     = term_b;
    end;
    term_a = imag_n(i+1)*omega(i+1)/(omega(i+1)^2-omega(i)^2);
    for j = i+1:n_frec-1
         %trapeze rule for integration
         term_b     = imag_n(j+1)*omega(j+1)/(omega(j+1)^2-omega(i)^2);
         n_re_KK(i) = n_re_KK(i) +  term_a + term_b;
         term_a     = term_b;
     end;
    n_re_KK(i) = 1.0 + delta_omega/pi*n_re_KK(i);
end;
%End apply Kramers-Kronig relations
clear i
clear j
%%%%%%%%%%%%%%%%%%%%%%%%%%%%%%%%%%%%%%%%%%%%%%%%%%%%%%%%%%%
% Calculate the branch number m
m_branch =round( (n_re_KK - real(n_eff)).*k0*d_eff/(2.0*pi) );

%store the -2, -1, 0, 1, 2 branches for plotting
n_eff_0    = real(n_eff);
n_eff_1    = n_eff_0 + 2.0*pi*1./(k0*d_eff);
n_eff_min1 = n_eff_0 + 2.0*pi*(-1)./(k0*d_eff);
n_eff_2    = n_eff_0 + 2.0*pi*2./(k0*d_eff);
n_eff_min2 = n_eff_0 + 2.0*pi*(-2)./(k0*d_eff);

%calculate the real part of n with the branch
n_eff   = n_eff +2.0*pi*m_branch./(k0*d_eff);
%Effective material parameters
ro_eff = n_eff.*zeff;
comp_eff = n_eff./zeff;
%--------DisplayResults

figure(1);
plot(f, 20*log10(abs(S11)),'r','linewidth',2.5);
hold on
plot(f, 20*log10(abs(S21)),'b','linewidth',2.5);
xlabel('Frequency [Hz]','fontsize',16);
ylabel('s-parameters [dB]','fontsize',16);
legend('S11', 'S21');
```

```
title ('s-parameters');
legend('location','Best');
legend('boxoff');
set(gca,'fontsize',16)

figure(2);
plot(f, (real(ro_eff)),'r','linewidth',2.5);
hold on
plot(f, (imag(ro_eff)),'b','linewidth',2.5);
xlabel('Frequency [Hz]','fontsize',16);
ylabel('Effective density','fontsize',16);
legend('Re(\rho)', 'Im(\rho)');
title ('Density');
legend('location','Best');
legend('boxoff');
set(gca,'fontsize',16)

figure (3);
plot(f,real(comp_eff),'r','linewidth',2.5);
hold on
plot(f,imag(comp_eff),'b','linewidth',2.5);
xlabel('Frequency [Hz]','fontsize',16);
ylabel('Effective compressibility','fontsize',16);
legend('Re(\beta)', 'Im(\beta)');
title ('Compressibility');
legend('location','Best');
legend('boxoff');
set(gca,'fontsize',16)

figure (4);
plot(f, (real(zeff)),'r','linewidth',2.5);
hold on
plot(f,imag(zeff),'b','linewidth',2.5);
xlabel('Frequency [Hz]','fontsize',16);
ylabel('Impedance','fontsize',16);
legend('Re(Z)', 'Im(Z)');
title ('Impedance');
legend('location','Best');
legend('boxoff');
set(gca,'fontsize',16)

figure (5);
plot(f, real(n_eff),'r','linewidth',2.5);
hold on
plot(f,imag(n_eff),'b','linewidth',2.5);
xlabel('Frequency [Hz]','fontsize',16);
ylabel('RefractiveIndex','fontsize',16);
legend('Re(n)', 'Im(n)');
title ('RefractiveIndex');
legend('location','Best');
legend('boxoff');
set(gca,'fontsize',16)

figure (6);
    hold on; frec= flist;
     set(gcf,'Color','w');
     hold on;
     plot(frec,n_eff_min2,':','Color',[0 0.7 0],'Linewidth',2);
```

```
     plot(frec,n_eff_min1,':','Color',[0.5 0.5 0.5],'Linewidth',2);
     plot(frec,n_eff_0,':','Color',[0.078431372549020   0.168627450980392
0.549019607843137],'Linewidth',2);
     plot(frec,n_eff_1,':','Color',[0.7 0 0],'Linewidth',2);
     plot(frec,n_eff_2,':','Color',[1 0.6 0.2],'Linewidth',2);
     plot(frec,real(n_eff),'rv','Linewidth',2,'Marker','v');
     grid on;
```

A3. Matlab code: Transmission line model for a compressibility near-zero metamaterial

```
clear all;
close all;
clc;

for el=1:4
    if el==1 % L-section
    a=5*10^-3; % radius [m]
    l=0.08; % length [m]
    end
    if el==2 % Helmholtz L-section
    a=10^-3; % radius [m]
    l=0.028; % length [m]
    end
    if el==3 % Helmholtz C-section
    a=4.25*10^-3; % radius [m]
    l=0.01; % length [m]
    end
    if el==4 % C-section (Half length)
    a=26*10^-3; % radius [m]
    l=0.01; % length [m]
    end
rho0=1.25; % density
B_0=1.42e5; % bulk modulus
c=sqrt(B_0/rho0); % speed of sound
mi=18*10^-6;
sigma=sqrt(0.71559);
ksi=0.2;
for f=200:2000; % Frequency [Hz]
w=2*pi*f;
rv=a*sqrt(rho0*w/mi);
rt=rv*sigma;
Fv=(2/(rv*sqrt(-1)))*((besselj(0,(rv*sqrt(-1i))))/(besselj(0,(rv*sqrt(-1i)))));
Ft=(2/(rt*sqrt(-1)))*((besselj(0,(rt*sqrt(-1i))))/(besselj(0,(rt*sqrt(-1i)))));
Z1=1i*((w*rho0)/(pi*a^2))*(1-Fv)^-1;
Z(f-199,1)=Z1;
Y1=1i*((w*pi*a^2)/(rho0*c^2))*(1+(ksi-1)*Ft);
Y(f-199,1)=Y1;
Z0(f-199,1)=sqrt(Z1/Y1);
Gamma(f-199,1)=sqrt(Z1*Y1);
A(f-199,1)=cosh(Gamma(f-199,1)*l);
B(f-199,1)=Z0(f-199,1)*sinh(Gamma(f-199,1)*l);
C(f-199,1)=(Z0(f-199,1)^-1)*sinh(Gamma(f-199,1)*l);
D(f-199,1)=cosh(Gamma(f-199,1)*l);
end
if el==1;
    ABCD_L(1,1,:)=A;
    ABCD_L(1,2,:)=B;
    ABCD_L(2,1,:)=C;
    ABCD_L(2,2,:)=D;
end
if el==2;
    ZHl=Z*l;
    YHl=Y*l;
end
if el==3;
    ZHc=Z*l;
```

```
        YHc=Y*l;
        ZH_sub=ZHc+1./YHc;
        YH_sub=YHl+1./ZH_sub;
        ZH=ZHl+1./YH_sub;
        YH=1./ZH;
        for n=1:1801
        ABCD_H(1,1,n)=1;
        ABCD_H(1,2,n)=0;
        ABCD_H(2,1,n)=YH(n);
        ABCD_H(2,2,n)=1;
        end
    end
    if el==4;
        ABCD_C(1,1,:)=A;
        ABCD_C(1,2,:)=B;
        ABCD_C(2,1,:)=C;
        ABCD_C(2,2,:)=D;
    end
    end

    for n=1:1801;
    ABCD(:,:,n)=ABCD_C(:,:,n)*ABCD_H(:,:,n)*ABCD_C(:,:,n)*ABCD_L(:,:,n)*ABCD_C(:,:,n)*ABCD_H(:,
    :,n)*ABCD_C(:,:,n);
    end

    S_parameters=abcd2s(ABCD,2*10^6);
    S21(1,:)=S_parameters(2,1,:);
    S11(1,:)=S_parameters(1,1,:);
    f=200:2000;
%--------DisplayResults

figure (1)
plot(f,20*log10(abs(S11)),'b', 'linewidth',2.5);
hold on
plot(f,20*log10(abs(S21)),'r', 'linewidth',2.5);
hold on
xlabel('Frequency [Hz]','fontsize',16);
ylabel('Reflection and Transmission[dB]','fontsize',16);
box on
legend('Reflection','Transmission');
legend('location','Best');
legend('boxoff');
set(gca,'fontsize',16);
```

A4. Matlab code: Signal processing and data acquisition

```
clc;
clear all;
close all;
br1=0;
for br2 = 0:119
    br1=br1+1;
    if br2 < 10
        str = sprintf('D:\\Measurement\\Results\\DTEK000%d.CSV', br2);
        strData = sprintf('data = DTEK000%d', br2);
    elseif br2 < 100
         str = sprintf('D:\\Measurement\\Results\\DTEK00%d.CSV', br2);
         strData = sprintf('data = DTEK00%d', br2);
    elseif br2 < 120
         str = sprintf('D:\\Measurement\\Results\\DTEK0%d.CSV', br2);
         strData = sprintf('data = DTEK0%d', br2);
    end
    load( str );
    eval( strData );
    [f1,k,amp,phi] = AmpPhaseNew(br1,data);
   AmpX(f1,k)=amp;
   PhiX(f1,k)=phi;
end

save AmpXP.mat
save PhiXP.mat

% % Measured S-parameters

clear all;
load freq
rho_0=1.25; % density
B_0=1.42e5; % bulk modulus
c=sqrt(B_0/rho_0); % speed of sound in air
x1=0.1; % probe 1 position [m]
x2=0.05; % probe 2 position [m]
x3=0.05; % probe 3 position [m]
x4=0.1; % probe 4 position [m]
load AmpX
load PhiX

    for p=1:length(AmpX(:,1))
        f(p)=freq(p);
        omega=2*pi*f;
        kx=omega/c;
        F1=0;
        F2=PhiX(p,2)-PhiX(p,1);
        F3=PhiX(p,3)-PhiX(p,1);
        F4=PhiX(p,4)-PhiX(p,1);

        P1a=AmpX(p,1)*exp(1i*(F1));
        P2a=AmpX(p,2)*exp(1i*(F2));
        P3a=AmpX(p,3)*exp(1i*(F3));
        P4a=AmpX(p,4)*exp(1i*(F4));
        k=kx(p);
    % In our case the system is symmetrical and reciprocal S11=S22 and S12=S21
        P1b=P4a;
```

```
        P2b=P3a;
        P3b=P2a;
        P4b=P1a;

        S11(p,1)=-(P1a*P3b*exp(1i*k*x1)*exp(2*1i*k*x2)*exp(1i*k*x3) -
P1b*P3a*exp(1i*k*x1)*exp(2*1i*k*x2)*exp(1i*k*x3) -
P2a*P3b*exp(2*1i*k*x1)*exp(1i*k*x2)*exp(1i*k*x3) +
P2b*P3a*exp(2*1i*k*x1)*exp(1i*k*x2)*exp(1i*k*x3) -
P1a*P4b*exp(1i*k*x1)*exp(2*1i*k*x2)*exp(1i*k*x4) +
P1b*P4a*exp(1i*k*x1)*exp(2*1i*k*x2)*exp(1i*k*x4) +
P2a*P4b*exp(2*1i*k*x1)*exp(1i*k*x2)*exp(1i*k*x4) -
P2b*P4a*exp(2*1i*k*x1)*exp(1i*k*x2)*exp(1i*k*x4))/(P1a*P3b*exp(1i*k*x1)*exp(1i*k*x3) -
P1b*P3a*exp(1i*k*x1)*exp(1i*k*x3) - P1a*P4b*exp(1i*k*x1)*exp(1i*k*x4) +
P1b*P4a*exp(1i*k*x1)*exp(1i*k*x4) - P2a*P3b*exp(1i*k*x2)*exp(1i*k*x3) +
P2b*P3a*exp(1i*k*x2)*exp(1i*k*x3) + P2a*P4b*exp(1i*k*x2)*exp(1i*k*x4) -
P2b*P4a*exp(1i*k*x2)*exp(1i*k*x4));

        S21(p,1)=-(P3a*P4b*exp(2*1i*k*x1)*exp(1i*k*x3)*exp(1i*k*x4) -
P3b*P4a*exp(2*1i*k*x1)*exp(1i*k*x3)*exp(1i*k*x4) -
P3a*P4b*exp(2*1i*k*x2)*exp(1i*k*x3)*exp(1i*k*x4) +
P3b*P4a*exp(2*1i*k*x2)*exp(1i*k*x3)*exp(1i*k*x4))/(P1a*P3b*exp(1i*k*x1)*exp(1i*k*x3) -
P1b*P3a*exp(1i*k*x1)*exp(1i*k*x3) - P1a*P4b*exp(1i*k*x1)*exp(1i*k*x4) +
P1b*P4a*exp(1i*k*x1)*exp(1i*k*x4) - P2a*P3b*exp(1i*k*x2)*exp(1i*k*x3) +
P2b*P3a*exp(1i*k*x2)*exp(1i*k*x3) + P2a*P4b*exp(1i*k*x2)*exp(1i*k*x4) -
P2b*P4a*exp(1i*k*x2)*exp(1i*k*x4));

    end

%--------DisplayResults

figure(1);
plot(f, 20*log10(abs(S11)),'r','linewidth',2.5);
hold on
plot(f, 20*log10(abs(S21)),'b','linewidth',2.5);
hold on
xlabel('Frequency [Hz]','fontsize',16);
ylabel('Reflection and transmission coefficeient [dB]','fontsize',16);
legend ('Reflection','Transmission');
set(gca,'fontsize',16);
grid off;

%% Function AmpPhaseNew

function [f1,k,amp,phi] = AmpPhaseNew(br1,data)

load freq
deltaomega = 0.1;
k=rem(br1,4); % probe number
if k==0;
    k=4;
end
brx=br1-k;
f1=brx/4;
f1=f1+1;
f=freq(f1);

%% Filtering
```

```
r = 1 - deltaomega / 2;
t = data(:,1)-data(1,1);
    x = data(:,2);
    xn = data(:,2);
    ang = 2 * pi * f*(t(2)-t(1));
    G = (1-r)*sqrt(1 - 2 * r * cos (2 * ang) + r*r);
    for i=1:length(data(:,1))
    x(1)=0; x(2)=0;
    if i>2
       x(i)= G * x(i) + 2*r*cos(ang)*x(i-1) - r*r*x(i-2);
    end
    end

%% Amplitude calculation

fs=1/(t(2)-t(1));
N   = length(x);
n   = 2:N-1;
x   = x(:);
ave = mean(x);
x=x-mean(x);
xs  = x(n-1)+x(n+1);
C   = xs'*x(n)/(x(n)'*x(n))/2;
amp = sqrt((x(n)'*x(n)-2*x(n)'*x(n+1)*C + x(n+1)'*x(n+1))/(1-C^2)/(N-2));
help=sin(2*t*pi*f);
fi=2*pi*(f/fs);
correct=angle(1-2*r*cos(fi)*exp(-1i*fi)+r^2*exp(-1i*2*fi)); % phase change cross in digital
resonator
N1 = floor(fs/f);

%% Phase calculation

for pr1=1:N1;
     partsum = 0;
     for pr2=1:N1
         if pr2 + 2 * N1 < length(x)
             partsum = partsum + x(pr2+2*N1)*help(pr1+pr2);
         else
             partsum = partsum + x(pr2+N1)*help(pr1+pr2);
         end
     end
     res(pr1) = partsum;
end

for pr1=1:length(res)
    if res(pr1)==max(res)
        n0=pr1;
        pr1=length(res);
    end
end


phi=2*pi*n0/N1+correct;
if phi>pi
    phi=phi-2*pi;
end
if phi<-pi
phi=phi+2*pi;
end
```

A5. Matlab code: Transmission line model for the novel unit cell (aSRR)

```
clear all;
close all;
clc;
a=1;
l=1;
for el=0:2
   if el==0 % Membrane
        ri=3*10^-3; % radius [m]
        poas= 0.34; % Poisson coefficient
        Jung= 2.758e9; % Young's modulus [Pa]
        rhom=1420; % density
        hm=20.7e-6; % thickness [m]
        rho1m=rhom*hm;
        D=(Jung*hm^3)/(12*(1-poas^2));
        zsny=sqrt(rho1m/D);
    end
    if el==1 % aSRR inner L section (half length)
    a=3*10^-3; % radius [m]
    l=0.016+(16*a/(3*pi));   % effective length [m]
    end
    if el==2 % aSRR outer L section
    a=8*10^-3; % outer radius [m]
    l=0.032;  % length [m]
    ri=3*10^-3; % inner radius [m]
    cs=0.1*10^-3;  % wall thickness
    end
rho0=1.25; % density
B_0=1.42e5; % bulk modulus
c=sqrt(B_0/rho0); % speed of sound
mi=18*10^-6;
sigma=sqrt(0.71559);
ksi=0.2;
for f=200:2000; % Frequency [Hz]
w=2*pi*f;
rv=a*sqrt(rho0*w/mi);
rt=rv*sigma;
Fv=(2/(rv*sqrt(-1)))*((besselj(0,(rv*sqrt(-1i))))/(besselj(0,(rv*sqrt(-1i)))));
Ft=(2/(rt*sqrt(-1)))*((besselj(0,(rt*sqrt(-1i))))/(besselj(0,(rt*sqrt(-1i)))));
Z1=1i*((w*rho0)/(pi*a^2))*(1-Fv)^-1;
Z(f-199,1)=Z1;
Y1=1i*((w*pi*a^2)/(rho0*c^2))*(1+(ksi-1)*Ft);
Y(f-199,1)=Y1;
if el==2
rv=(a-ri)*sqrt(rho0*w/mi);
rt=rv*sigma;
Fv=(2/(rv*sqrt(-1)))*((besselj(0,(rv*sqrt(-1i))))/(besselj(0,(rv*sqrt(-1i)))));
Ft=(2/(rt*sqrt(-1)))*((besselj(0,(rt*sqrt(-1i))))/(besselj(0,(rt*sqrt(-1i)))));
Z1=1i*((w*rho0)/(pi*(a^2-(ri+cs)^2)))*(1-Fv)^-1;
Z(f-199,1)=Z1;
Y1=1i*((w*pi*(a^2-(ri+cs)^2))/(rho0*c^2))*(1+(ksi-1)*Ft);
Y(f-199,1)=Y1;
end
Z0(f-199,1)=sqrt(Z1/Y1);
Gamma(f-199,1)=sqrt(Z1*Y1);
A(f-199,1)=cosh(Gamma(f-199,1)*l);
B(f-199,1)=Z0(f-199,1)*sinh(Gamma(f-199,1)*l);
```

```
C(f-199,1)=(Z0(f-199,1)^-1)*sinh(Gamma(f-199,1)*l);
D(f-199,1)=cosh(Gamma(f-199,1)*l);
end
if el==0
    for f=200:2000;
    w=2*pi*f;
    km(f-199,1)=sqrt(w*zsny);
    pr=km*ri;
    S=pi*ri^2;
    m=rho1m*S;
    Zm=-
j*w*m*((besseli(1,pr).*besselj(0,pr)+besselj(1,pr).*besseli(0,pr))./(besseli(1,pr).*besselj(2
,pr)-besselj(1,pr).*besseli(2,pr)));
    end

for n=1:1801
A(n,1)=1;
B(n,1)=Zm(n)/(S^2);
C(n,1)=0;
D(n,1)=1;
end
end
if el==0;
    ABCD0(1,1,:)=A;
    ABCD0(1,2,:)=B;
    ABCD0(2,1,:)=C;
    ABCD0(2,2,:)=D;
end

if el==1;
    ABCDLi(1,1,:)=A;
    ABCDLi(1,2,:)=B;
    ABCDLi(2,1,:)=C;
    ABCDLi(2,2,:)=D;
    for n=1:1801;
    ABCDMx(:,:,n)=ABCDLi(:,:,n)*ABCD0(:,:,n)*ABCDLi(:,:,n);
    end
    Ym0=abcd2y(ABCDMx);
end
if el==2;
    ABCDLo(1,1,:)=A;
    ABCDLo(1,2,:)=B;
    ABCDLo(2,1,:)=C;
    ABCDLo(2,2,:)=D;
    YL0=abcd2y(ABCDLo);
    Ym=Ym0+YL0;
    ABCD=y2abcd(Ym);
end

end

S_parameters=abcd2s(ABCD,2*1e6);
S21(1,:)=S_parameters(2,1,:);
S11(1,:)=S_parameters(1,1,:);
f=200:2000;

%--------DisplayResults
```

```
figure (1)
plot(f,20*log10(abs(S11)),'b', 'linewidth',2.5);
hold on
plot(f,20*log10(abs(S21)),'r', 'linewidth',2.5);
hold on
xlabel('Frequency [Hz]','fontsize',16);
ylabel('Reflection and Transmission[dB]','fontsize',16);
box on
legend('Reflection','Transmission');
legend('location','Best');
legend('boxoff');
set(gca,'fontsize',16);
```

A6. Matlab code: Temperature distribution calculation for a wave transformation

```
clc;        % clear screen
clear all;  % deletes the workspace
close all;  % closes all figures

% Parameters

d=2.5*1e-3; % period of the grooves
a=0.5*1e-3; % width of the grooves
h=23*1e-3; % depth of the grooves
R=287.058; % Specific gas constant (Air)
T0=273.15; % 0 Celsius in K
P=101325; % Atmospheric pressure
gamma=1.4; % adiabatic constant
T_ref=20; % Referent temperature in Celsius
T_max=50; % Maximum applied temperature in Celsius
freq=3400; % opereting frequency
Tc=(4*freq*h)^2/(gamma*R)-T0; % Critical Temperature
T=Tc:0.01:2*T_max;
w=2*pi*freq;

parameter1=input('0 (Bending) or 1 (Focusing):');

%% Ref. Air Parameter Calculation
rho_ref=P/(R*(T_ref+T0));
c_ref=sqrt((gamma*P)/rho_ref);
k_ref=w*sqrt(rho_ref/(gamma*P));

%% Ref. Surf. Parameter Calculation

rho_surface_ref=rho_ref*(1+(a/d)^2*(tan(k_ref*h))^2);
c_surface_ref=sqrt((gamma*P)/rho_surface_ref);
k_surface_ref=w*sqrt(rho_surface_ref/(gamma*P));

if parameter1==0; %Bending
Y2=40*d; % Thicknes of the lens
n=25; % Number of the channels
X0=500*1e-3; % width of the lens
phi=30; % Bending degree
deltaPsi=0;
const=2;
end

if parameter1==1 %HyperbolicSecant
n_h=1; % Refractive index on the edge of the GRIN medium
Y2=20*d; % Thicknes of the lens
n=25; % number of the channels
X0=250*1e-3; % half width of the lens
n_0=1.2*n_h; % Refractive index in the center of the GRIN medium
alphaX=(1/X0)*acosh(n_0/n_h);
end
x_fix=X0/n;
xi=(n-1)*x_fix+x_fix/2:-x_fix:x_fix/2;

if parameter1==0 % Bending
for i=1:length(xi);
```

```
    n_max=(X0/Y2)*sind(phi)+1;
    nx(i)=1+(n_max-1)/X0*xi(i);
    beta2(i)=k_surface_ref*nx(i);
    R1(i,:)= round(beta2(i)*ones(1,length(T)));
    end
end
if parameter1== 1 % HyperbolicSecant
 for i=1:length(xi);
    F(i)=sech(alphaX*xi(i));
    nx(i)=n_0*F(i);
    rHo(i)=(nx(i))^2;
    R1(i,:)= round(rHo(i)*ones(1,length(T))*100)/100;
 end
 end

%% Parameter Calculation (free air)
for i=1:length(T)
rho(i)=P/(R*(T(i)+T0));
c(i)=sqrt((gamma*P)/rho(i));
k(i)=w*sqrt(rho(i)/(gamma*P));
end

%% Surface Parameter Calculation

for i=1:length(T)
rho_surface(i)=rho(i)*(1+(a/d)^2*(tan(k(i)*h))^2);
rho_surfaceR(i)=round(rho_surface(i)*10)/00;
c_surface(i)=sqrt((gamma*P)/rho_surface(i));
k_surface(i)=w*sqrt(rho_surface(i)/(gamma*P));
k_surfaceR(i)=round(k_surface(i));
end

%% Intersect (Graphical Eq. solving)
for i=1:length(xi)
    [c, ia, ib] = intersect(k_surfaceR, R1(i,:));
    Tx(i,1)=T(ia)-T_ref;
end

%% DisplayResults

figure (1)
plot(1000*xi,T_ref+Tx,'or','linewidth',2.5);
hold on
xlabel('x[mm]','fontsize',12);
ylabel('T[\circC]','fontsize',12);
hold on
```

References:

[1] J. Billingham, *Wave motion*, Cambridge University Press, 2000

[2] Lord Rayleigh, *The Theory of Sound*, 2*nd ed*., New York: Dover, 1945

[3] A. Wood, *Acoustics* 2*nd ed*., New York: Dover, 1966

[4] L.L.Beranek, *Acoustics*, McGraw-Hill, New York, 1954

[5] Lawrence E. Kinsler, Austin R. Frey, Alan B. Coppens, James V. Sanders, *Fundamentals of Acoustics*, 4*th ed*., Johm Willey&Sons, Inc, 2000

[6] C. K. Campbell, *Surface Acoustic Wave Devices for Mobile and Wireless Communications*, Academic Press, July, 2000

[7] Ken-ya Hashimoto, *Surface Acoustic Wave Devices in Telecommunications*, Springer Berlin Heidelberg, 2000

[8] Norman J. Berg, *Acousto-Optic Signal Processing: Theory and Implementation*, Marcel Dekker Inc, March 1983

[9] U. L. Rohde, *Microwave and Wireless Synthesizers: Theory and Design*, Wiley-Interscience, August 1997

[10] Constantine A. Balanis, *Advanced Engineering Electromagnetics second edition*, Wiley, January 2012

[11] John David Jackson**,** *Classical Electrodynamics Third Edition*, Wiley, August 1998

[12] Shu Zhang, *Acoustic metamaterial design and applications, PhD thesis*, University of Illinois at Urbana-Champaign, 2010

[13] Petar Pravica, Dragan Drinčić, *Elektroakustika*, Beograd, 2006

[14] Jens Blauert, Ning Xiang, *Acoustics for Engineers*, Springer Berlin Heidelberg, January, 2009

[15] Jean-Paul Marage, Yvon Mo, *Sonar and Underwater Acoustics*, John Wiley & Sons, Inc., March, 2010

[16] Veselago, V. G., "Electrodynamics of substance with simultaneously negative values of μ and ε" *Sov. Phy. Uspekhi-USSR* **10,** 509-514, 1968

[17] J. B. Pendry, A. J. Holden, W. J. Stewart and I. Youngs, "Extremly low frequency plasmons in metallic mesostructures," *Phys. Rev. Lett.*, Vol. 76, No. 25, pp. 4773-4776, 17 June 1996

[18] Pendry, J. B., Holden, A. J., Robbins, D. J. & Stewart, W. J., "Magnetism from conductors and enhanced nonlinear phenomena", *IEEE Trans. Microw. Theory Tech.* 47, 2075-2084 (1999).

[19] Smith, D. R., Padilla, W. J., Vier, D. C., Nemat-Nasser, S. C. & Schultz, S., "Composite medium with simultaneously negative permeability and permittivity" *Phys. Rev. Lett.*, 84, 4184–4187, 2000

[20] Shelby, R., Smith, D. R. & Schultz, S., "Experimental verification of a negative index of refraction" *Science* 292, 77-79, 2001

[21] Shurig, D. et al., "Metamaterial electromagnetic cloak at microwave frequencies", *Science* 314, 977-980, 2006

[22] Pendry, J. B., "Neative refraction makes a perfect lens", *Phys. Rev. Lett.* **85,** 3966-3969, 2000

[23] Engheta, N. & Ziolkowski, R. W., *Metamaterials Physics and Engineering Explorations*, Wiley, New York, 2006

[24] Caloz, C. & Itoh, T., *Electromagnetic Metamaterials — Transmission Line Theory and Microwave Applications*, Wiley, New York, 2006

[25] A. Lai, T. Itoh and C. Caloz: "Composite right/left handed transmission line metamaterials," *IEEE microwave magazine*, September 2004

[26] Iyer, A. K., Kremer, P. C. & Eleftheriades, G. V., "Experimental and theoretical verification of focusing in a large, periodically loaded transmission line negative refractive index metamaterial", *Opt. Express* 11, 696–708, 2003

[27] Fang, N. et al., "Ultrasonic metamaterials with negative modulus", *Nature Mater.* **5,** 452–456, 2006

[28] Hu, X., Ho, K.-M., Chan, C. T. & Zi, J., "Homogenization of acoustic metamaterials of Helmholtz resonators in fluid", *Phys. Rev. B* 77, 172301, 2008.

[29] Liu, Z. Y. et al., "Locally resonant sonic materials", *Science* 289, 1734–1736, 2000

[30] J. Mei, Z. Liu, W. Wen, and P. Sheng, "Effective dynamic mass density of composites", *Phys. Rev. B*, Vol. 76, 134205, 2007

[31] J. Mei, Z. Liu, W. Wen, P. Sheng, "Effective mass density of fluid-solid composites", *Phys. Rev. Lett.* 96, 24301, 2006

[32] S. Yao, X. Zhou, G. Hu, "Experimental study on negative effective mass in a 1d mass–spring system", *New J. Phys.* 10, 043020, 2008

[33] S. Yao, X. Zhou, G. Hu, "Investigation of the negative-mass behaviors occurring below a cutoff frequency" *New J. Phys.* 12, 103025, 2010

[34] Z. G. Wang et al., "Effective medium theory of the one-dimensional resonance phononic crystal", *J. Phys.: Condens. Matter.* 20, 055209, 2008

[35] Liu, Z., Chan, C. T. & P. Sheng, "Analytic model of phononic crystals with local resonances", *Phys. Rev. B* 71, 014103 (2005).

[36] X. Zhou & H. Gengkai, "Analytic model of elastic metamaterials with local resonances", *Phys. Rev. B.* **79,** 195109, 2009

[37] S. H. Lee, C. M. Park, Y. M. Seo, Z. G. Wang & C. K. Kim, "Acoustic metamaterial with negative modulus", *J. Phys.: Condens. Matter* 21, 175704, 2009

[38] Z. Yang, J. Mei, M. Yang, N. H. Chan, & P. Sheng, "Membrane-type acoustic metamaterial with negative dynamic mass", *Phys. Rev. Lett.* 101, 204301, 2008

[39] S. H. Lee, C. M. Park, Y. M. Seo, Z. G. Wangd & C. K. Kima, "Acoustic metamaterial with negative density", *Phys. Lett. A* 373, 4464–4469, 2009

[40] M. Ambati, N. Fang, C. Sun, X. Zhang, "Surface resonant states and superlensing in acoustic metamaterials", *Phys. Rev. B* 75, 195447, 2007

[41] S. Guenneau, A. Movchan, G. Pe´tursson, S. A. Ramakrishna, "Acoustic metamaterials for sound focusing and confinement", *New J. Phys.* 9, 399, 2007

[42] X. Zhou, G. Hu, "Superlensing effect of an anisotropic metamaterial slab with near-zero dynamic mass", *Appl. Phys. Lett*. 98, 263510, 2011

[43] J. Li, Z. Liu, C. Qiu, "Negative refraction imaging of acoustic waves by a two-dimensional three-component phononic crystal", *Phys. Rev. B* 73, 054302, 2006

[44] S. Zhang, L. Yin, N. Fang, "Focusing ultrasound with an acoustic metamaterial network", *Phys. Rev. Lett*. 102, 194301, 2009

[45] L. Zigoneanu, B.-I. Popa, and S. A. Cummer, "Design and measurements of a broadband two-dimensional acoustic lens", *Physical Review B*, 84, 024305, 2011

[46] J. Li, L. Fok, X. Yin, G. Bartal, X. Zhang, "Experimental demonstration of an acoustic magnifying hyperlens", *Nat. Mater*. 8, 931, 2009

[47] H. Chen, C. Chan, "Acoustic cloaking in three dimensions using acoustic metamaterials", *Appl. Phys. Lett.* 91, 183518, 2007

[48] S.A. Cummer, D. Schurig, "One path to acoustic cloaking", *New J. Phys*. 9, 45, 2007

[49] Y. Cheng, F. Yang, J.Y. Xu, X.J. Liu, "A multilayer structured acoustic cloak with homogeneous isotropic materials, *Appl. Phys. Lett.* 92, 151913, 2008

[50] J. Pendry, J. Li, "An acoustic metafluid: realizing a broadband acoustic cloak", *New J. Phys*. 10, 115032, 2008

[51] S. A. Cummer, B. I. Popa, D. Schurig, D. R. Smith, J. Pendry, M. Rahm, A. Starr, "Scattering theory derivation of a 3d acoustic cloaking shell", *Phys. Rev. Lett.* 100, 24301, 2008

[52] Y. Urzhumov, F. Ghezzo, J. Hunt, D. R. Smith, "Acoustic cloaking transformations from attainable material properties", *New J. Phys*. 12, 073014, 2010

[53] Z. Liang, J. Li, "Bending a periodically layered structure for transformation acoustics", *Appl. Phys. Lett.* 98, 241914, 2011

[64] X. Zhu, B. Liang, W. Kan, X. Zou, J. Cheng, "Acoustic cloaking by a superlens with singlenegative materials", *Phys. Rev. Lett*. 106, 14301, 2011

[55] M. Farhat, S. Enoch, S. Guenneau, A. Movchan, "Broadband cylindrical acoustic cloak for linear surface waves in a fluid", Phys. Rev. Lett. 101, 134501, 2008

[56] M. Farhat, S. Guenneau, S. Enoch, A.B.. Movchan, "Cloaking bending waves propagating in thin elastic plates", *Phys. Rev. B*, 79, 033102, 2009

[57] M. Farhat, S. Guenneau, S. Enoch, "Ultrabroadband elastic cloaking in thin plates", *Phys. Rev. Lett.* 103, 24301, 2009

[58] S. Zhang, C. Xia, N. Fang, "Broadband acoustic cloak for ultrasound waves", *Phys. Rev. Lett.* 106, 24301, 2011

[59] B. I. Popa, L. Zigoneanu, S. A. Cummer, "Experimental acoustic ground cloak in air", *Phys. Rev. Lett.* 106, 253901, 2011

[60] J. Li, C. Chan, "Double-negative acoustic metamaterial", *Phys. Rev. E* 70, 055602, 2004

[61] Y. Ding, Z. Liu, C. Qiu, J. Shi, "Metamaterial with simultaneously negative bulk modulus and mass density", *Phys. Rev. Lett.* 99, 93904, 2007

[62] Y. Cheng, J. Xu, X. Liu, "One-dimensional structured ultrasonic metamaterials with simultaneously negative dynamic density and modulus". *Phys. Rev. B* 77, 045134, 2008

[63] Bongard, F., Lissek, H. & Mosig, J.R., "Acoustic transmission line metamaterial with negative/zero/positive refractive index," *Phys. Rev. B* **82,** 94306, 2010

[64] S.H. Lee, C.M. Park, Y.M. Seo, C.K. Kim, "Reversed Doppler effect in double negative metamaterials", *Phys. Rev. B* 81, 241102, 2010

[65] B. Liang, et al., "An acoustic rectifier", *Nature Materials* vol. 9, pp. 989–992, 2010 doi:10.1038/nmat2881

[66] Popa, B.-I. and S. A. Cummer, "Non-reciprocal and highly nonlinear active acoustic metamaterials", *Nature Comm.*, Vol. 5, 3398, doi:10.1038/ncomms4398, 2014

[67] Fleury, R., D. L. Sounas, C. F. Sieck, M. R. Haberman, and A. Alu, "Sound isolation and giant linear nonreciprocity in a compact acoustic circulator", *Science*, Vol. 343, 516-519, doi:10.1126/science.1246957, 2014

[68] Pierre Deymier, *Acoustic Metamaterials and Phononic Crystals*, Springer-Verlag, Berlin, 2013

[69] D. M. Pozar, *Microwave Engineering*, John Wiley & Sons Inc., New York, 1998

[70] S. Mao, S. Chen, C. Huang, "Effective electromagnetic parameters of novel distributed left-handed microstrip lines," *IEEE Trans. Microw. Theory and Tech*, vol. 53, no. 4, pp. 1515-1521, 2005.

[71] Zs. Szabó, G. Park, R. Hedge, E. Li, "A unique extraction of metamaterial parameters based on Kramers- Kronig relationship," *IEEE Trans. Microw. Theory and Tech*, vol. 58, no. 10, pp. 2646-2653, 2010.

[72] G. Gonzalez, *Microwave Transistor Amplifies: Analysis and Design*, *2nd ed*. Englewood Cliffs, NJ: Prentice-Hall, 1997.

[73] A. M. Nicolson and G. Ross, "Measurement of intrinsic properties of materials by time domain techniques," *IEEE Trans. Instrum. Meas.*, vol. 19, no. 11, pp. 377–382, Nov. 1970.

[74] W. B. Weir, "Automatic measurement of complex dielectric constant and permeability at microwave frequencies," *Proc. IEEE*, vol. 62, no. 1, pp. 33–36, Jan. 1974.

[75] X. Chen, T. M. Grzegorczyk, B. I. Wu, J. Pacheco, and J. A. Kong, “Robust method to retrieve the constitutive effective parameters of metamaterials,” *Phys. Rev. E, Stat. Phys. Plasmas Fluids Relat. Interdiscip. Top.*, vol. 70, Feb. 2004, Art. ID 016608

[76] V. Lucarini, J. J. Saarinen, K. E. Peiponen, and E. M. Vartiainen, *Kramers–Kronig Relations in Optical Materials Research*. Berlin, Germany: Springer-Verlag, 2005

[77] N. Cselyuszka, M. Sečujski, V. Crnojević-Bengin", Analysis and synthesis of acoustic metamaterials based on Helmholtz resonator," *ETRAN Zlatibor, Serbia*, 11-14. jun 2012.

[78] N. Cselyuszka, M. Sečujski, V. Crnojević, "Analysis of Acoustic Metamaterials -Acoustic Scattering Matrix and Extraction of Effective Parameters," *METAMATERIALS, St. Petersburg, Russia,* 17-22 September 2012

[79] *Introduction to Comsol multiphysics, version 4.3a*, October 2012

[80] C*omsol Multiphysics: "Acoustic module, user’s guide, version 4.3b*", May 2013

[81] *Comsol Multiphysics: "Structural mechanics module, user’s guide, version 4.3*", May 2012

[82] *Comsol Multiphysics: "Heat Transfer module, user’s guide, version 4.3*", May 2012

[83] G. Kirchhoff, “On the influence of heat conduction in a gas on sound propagation”, *Ann. Phys. Chem*. vol. 134, pp. 177–193, 1868

[84] H. Benade „On the Propagation of Sound Waves in a Cylindrical Conduit“, *The Journal of the Acoustical Society of America*, vol. 44, no. 2, pp. 616-623, 1968

[85] D. H. Keefe, “Acoustical wave propagation in cylindrical ducts: Transmission line parameter approximations for isothermal and nonisothermal boundary conditions”, *Journal of the Acoustical Society of America*, vol. 75, pp. 58–62, 1984

[86] J. C. Zuercher, E. V. Carlson, and M. C. Killion, “Small acoustic tubes: New approximations including isothermal and viscous effects”, *Journal of the Acoustical Society of America* vol. 83, pp. 1653–1660, 1988

[87] R. Christensen, P. Juhl and V. Cutanda Henriquez, „Practical modeling of acoustic losses in air due to heat conduction and viscosity*“, Acoustic' 08, Paris, France*, Jun 29- July 04, 2008.

[88] M. Silveirinha and N. Engheta, "Tunneling of electromagnetic energy through sub-wavelength channels and bends using epsilon-near-zero (ENZ) materials", *Phys. Rev. Lett.* 97, 157403, 2006

[89] B. Edwards, A. Alu, M. E. Young, M. Silveirinha, and N. Engheta, "Experimental verification of epsilon-near-zero metamaterial coupling and energy squeezing using a microwave waveguide", *Phys. Rev. Lett.* 100, 033903, 2008

[90] X. Huang, Y. Lai, Z. H. Hang, H. Zheng, and C. T. Chan, "Dirac cones induced by accidental degeneracy in photonic crystals and zero-refractive-index materials", *Nature Materials*, vol. 10, pp. 582-586 ,2011

[91] Q. Cheng, R. Liu, D. Huang, T. J. Cui, and D. R. Smith, "Circuit verification of tunneling effect in zero permittivity medium", *App. Phys. Lett*. 91, 234105, 2007

[92] V. Crnojević-Bengin, N. Janković, and R. H. Geschke, "Epsilon-near-zero transmission in quasi-TEM microstrip circuits, " *Proceedings of 41st European Microwave Conference,* Manchester, 2011

[93] V. Crnojević-Bengin, N. Cselyuszka, N. Jankovic, R. H. Geschke, "Mu-Near-Zero Propagation in Quasi-TEM Microstrip Circuits," *Journal Of Electromagnetic Waves And Applications*, vol. 27, no. 17, pp. 2198-2212, September 2013

[94] Z. Liang and J. Li, "Extreme Acoustic Metamaterial by Coiling Up Space", *Phys. Rev. Lett.* 108, 114301, 2012

[95] R. Fleury, C.F. Sieck, M.R. Haberman, A.Alù, "Anomalous transmission properties of ultranarrow, zero-density acoustic metachannels", *METAMATERIALS, St. Petersburg, Russia,* 17-22 September 2012

[96] R. Fleury, A.Alù, "Extraordinary sound transmission through density-near-zero ultranarrow channels", *Phys. Rev. Lett.* 111, 055501, 2013

[97] Jong Jin Park, K. J. B. Lee, Oliver B. Wright, Myoung Ki Jung, and Sam H. Lee, "Giant Acoustic Concentration by Extraordinary Transmission in Zero-Mass Metamaterials", *Phys. Rev. Lett.* 110, 244302, 2013

[98] X.-F. Zhu, "Effective Zero Index In Locally Resonant Acoustic Material", *Physics Letters A,* vol. 377, no. 31-33, pp. 1784-1787, October, 2013

[99] N. Cselyuszka, M. Sečujski, V. Crnojević-Bengin, "Compressibility-near-zero acoustic metamaterial", *Physics Letters A*, vol. 378, no. 16-17, pp. 1153-1156, March, 2014

[100] T. W. Parks, C. S. Burrus, *"Digital Filter Design (Topics in Digital Signal Processing)",* Wiley-Interscience, August 1987

[101] Richard G. Lyons, *"Understanding Digital Signal Processing (3rd Edition)",* Prentice Hall; 3 edition, November 11, 2010

[102] M.B. Xu, A. Selamet , H. Kim, "Dual Helmholtz resonator",*Applied Acoustics*, vol. 71, pp. 822–829, 2010

[103] S. H. Lee, C. M. Park, Y. M. Seo, Z. G. Wang and C. K. Kim, "Composite Acoustic Medium with Simultaneously Negative Density and Modulus," *Physical Review Letters*, Vol. 104, No. 5, pp. 54301(4), 5 February 2010

[104] M. Guancong, et al., "Low-frequency narrow-band acoustic filter with large orifice," *Applied Physics Letters*, 103, 1, 011903, 2013

[105] F. Falcone, T. Lopategi, M. A. Laso, J. D. Baena, J. Bonache, M. Beruete, R. Marqués, F. Martin and M. Sorolla "Babinet principle applied to the design of metasurfaces and metamaterials", *Phys. Rev. Lett.*, Vol. 93, No. 19, November 2004

[106] F. Falcone, T. Lopategi, J. D. Baena, R. Marqués, F. Martin and M. Sorolla, "Effective Negative- ε Stopband Microstrip Lines Based on Complementary Split Ring Resonators," *IEEE Microwave and Wireless Components Letter*, Vol. 14, No. 6, pp. 280-282, June 2004

[107] J. D. Baena, et al, " Equivalent-Circuit Models for Split-Ring Resonators and Complementary Split-Ring Resonators Coupled to Planar Transmission Lines," *IEEE Trans. Microw. Theory Tech.* Vol. 53, No. 4, pp. 1451- 1461 (2005).

[108] R. Marqués, F. Martin and M. Sorolla: "*Metamaterials with Negative Parameters: Theory, Design, and Microwave Applications,* " John Wiley & Sons Inc., New Jersey, 2008

[109] N. Cselyuszka, M. Sečujski, V. Crnojević-Bengin, „Novel negative mass density resonant metamaterial unit cell“, *Physics Letters A*, Vol. 379, No. 1-2, pp. 33-36, January 2015, Elsevier

[110] Y. Min, et al., "Homogenization scheme for acoustic metamaterials." *Physical Review B*, 89, 6, 064309, 2004.

[111] M. Rossi, *Acoustics and Electroacoustics,* Artech House, Norwood, MA, 1988.

[112] P. M. Morse and K. U. Ingard, *Theoretical Acoustics,* Princeton University Press, Princeton, NJ, 1986.

[113] Z. Skvor, *Vibrating Systems and their Equivalent Circuits,* Elsevier, New York, 1991

[114] M. Sečujski, N. Cselyuszka, V. Crnojević-Bengin, „A novel approach to density near zero acoustic metamaterials“, *Advances in Materials Science and Engineering*, Volume 2015 (2015), Article ID 626593, doi: http://dx.doi.org/10.1155/2015/626593

[115] J.-C. Weeber, A. Dereux, C. Girard, J. R. Krenn, and J.-P. Goudonnet, "Plasmon polaritons of metallic nanowires for controlling submicron propagation of light", *Physical Review B*, 60, 9061, 1999

[116] H. Ditlbacher, J. R. Krenn, G. Schider, A. Leitner, F. R. Aussenegg, "Two-dimensional optics with surface plasmon polaritons", *Appl.Phys.Lett.* 81, 1762, 2002

[117] W. L. Barnes , A. Dereux, T. W. Ebbesen, "Surface plasmon subwavelength optics," *Nature*, 14;424(6950):824-30 Aug. 2003

[118] T. W. Ebbesen, H. J. Lezec, H. F. Ghaemi, T. Thio, P. A. Wolff, "Extraordinary optical transmission through sub-wavelength hole arrays," *Nature* 391, 667–669, 1998

[119] C. Genet & T. W. Ebbesen, Light in tiny holes, *Nature*, **445**, 39-46, January 2007

[120] M. I. Stockman, “Nanofocusing of optical energy in tapered plasmonic waveguides,” *Phys. Rev. Lett.* 93, 137404-1–4, 2004

[121] A. Rusina, M. Durach, K. A. Nelson, and M. I. Stockman, "Nanoconcentration of terahertz radiation in plasmonic waveguides", *Optics Express* Vol. 16, Issue 23, pp. 18576-18589, 2008

[122] J. B. Pendry, L. Martı´n-Moreno, F. J. Garcia-Vidal, "Mimicking Surface Plasmons with Structured Surfaces" *Science* 305, 847, 2004

[123] A. P. Hibbins, B. R. Evans, J. R. Sambles, "Experimental Verification of Designer Surface Plasmons", *Science*,308, 670, 2005

[124] N. Yu, Q. J. Wang, M. A. Kats, J. A. Fan, S. P. Khanna, L. Li, A. G. Davies, E. H. Linfield and F. Capasso, "Designer spoof surface plasmon structures collimate terahertz laser beams, " *Nature Materials,* Vol 9, September 2010

[125] Fernandez-Doınguez, L. Mart´ın-Moreno, F. J. Garc´ıa-Vidal, S. R. Andrews, and S. A. Maier, "Spoof Surface Plasmon Polariton Modes Propagating Along Periodically Corrugated Wires", *IEEE Journal Of Selected Topics In Quantum Electronics*, Vol. 14, No. 6, November 2008

[126] Y. J. Zhou and T. J. Cu, "Broadband slow-wave systems of subwavelength thickness excited by a metal wire," *Applied Physics Letters,* 99, 101906, 2011

[127] D. Martin-Cano et al., "Domino plasmons for subwavelength terahertz circuitry ", *Optics Express*, Vol. 18, No. 2 18 January 2010

[128] Y. G. Ma et al., "Experimental demonstration of subwavelength domino plasmon devices for compact high frequency circuit", *Optics Express,* Vol. 19, No. 22, 24 October 2011

[129] F J Garcia-Vidal, L Mart´ ın-Moreno and J B Pendry, "Surfaces with holes in them: new plasmonic metamaterials", *J. Opt. A: Pure Appl. Opt.* 7, pp 97–101, 2005

[130] Z. Ruana, M. Qiub, "Slow electromagnetic wave guided in subwavelength region along one-dimensional periodically structured metal surface," *Applied Physics Letters* 90, 201906, 2007

[131] L. Kelders, et al., "Ultrasonic surface waves above rectangular-groove gratings", *J. Acoust. Soc. Am.* 103 (5), Pt. 1, May 1998

[132] L. Kelders, W. Lauriks, and J. F. Allard, "Surface waves above thin porous layers saturated by air at ultrasonic frequencies", *J. Acoust. Soc. Am.* 104 (2), Pt. 1, August 1998

[133] Zhaojian He, Han Jia, Chunyin Qiu, Yangtao Ye, Rui Hao, Manzhu Ke, and Zhengyou Liu, "Nonleaky surface acoustic wave s on a textured rigid surface", *Physical Review B,* 83, 132101, 2011

[134] J. Christensen, P. A. Huidobro, L. Martín-Moreno, and F. J. García-Vida, "Confining and slowing airborne sound with a corrugated metawire" *Applied Physics Letters*, 93, 083502, 2008

[135] J. Zhu, Y. Chen, X. Zhu, F. J. Garcia-Vidal, X. Yin, W. Zhang and X. Zhang "Acoustic rainbow trapping" *Scientific Reports*, Vol. 3, 01728, 2013

[136] H. Jia, M. Lu, X. Ni, M. Bao, and X. Li, "Spatial separation of spoof surface acoustic waves on the graded groove grating", *Journal of Applied Physics* 116, 124504, 2014

[137] J. Christensen, A. I. Fernandez-Dominguez, F. D, Leon-Perez, L. Martin-Moreno and F. J. Garcia-Vidal, "Collimation of sound assisted by acoustic surface waves", *Nature Phys.* 3, 851, 2007

[138] J. Christensen, L. Martín-Moreno, and F. J. García-Vidal, "Enhanced acoustical transmission and beaming effect through a single aperture", *Physical Review B*, 81, 174104, 2010

[139] Y. Zhou, M.-H. Lu, L. Feng, X. Ni, Y.-F. Chen, Y.-Y. Zhu, S.-N. Zhu, and N.-B. Ming, "Acoustic Surface Evanescent Wave and it s Dominant Contribution to Extraordinary Acoustic Transmission and Collimation of Sound" *Phys. Rev. Lett.*, 104, 164301, 2010

[140] Y. Ye et al. "Focusing of spoof surface-acoustic-waves by a gradient-index structure", *Journal of Applied Physics* 114, 154504, 2013

[141] P. Hess, "Surface acoustic waves in materials science", *Phys. Today*, pp. 42–47, March 2002

[142] N. Cselyuszka, M. Sečujski, N. Engheta, V. Crnojević-Bengin, „Temperature-controlled acoustic surface waves“, *(under review)*

[143] B. I. Popa and S. A. Cummer, "Design and characterization of broadband acoustic composite metamaterials", *Physical Review B*, 80, 174303 2009

[144] A. Climente, D. Torrent, and J. Sánchez-Dehesa, "Sound focusing by gradient index sonic lenses", *Applied Physics Letters*, 97, 104103 2010

[145] Sz-C. S. Lin and T. J. Huang, "Gradient-index phononic crystals", *Physical Review B*, 79, 094302, 2009

[146] Gomez-Reino, C., Perez, M.V., Bao, C., *Gradient-Index Optics: Fundamentals and Applications*, Springer, New York, 2002